

UNCLASSIFIED

---

AD 256 357

*Reproduced  
by the*

ARMED SERVICES TECHNICAL INFORMATION AGENCY  
ARLINGTON HALL STATION  
ARLINGTON 12, VIRGINIA

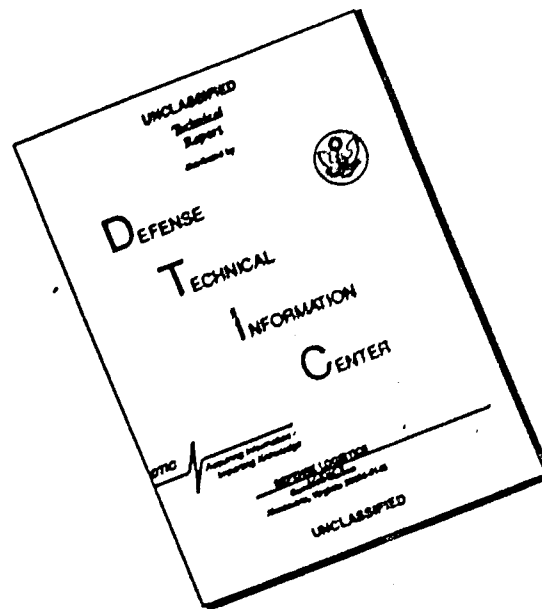


---

UNCLASSIFIED

NOTICE: When government or other drawings, specifications or other data are used for any purpose other than in connection with a definitely related government procurement operation, the U. S. Government thereby incurs no responsibility, nor any obligation whatsoever; and the fact that the Government may have formulated, furnished, or in any way supplied the said drawings, specifications, or other data is not to be regarded by implication or otherwise as in any manner licensing the holder or any other person or corporation, or conveying any rights or permission to manufacture, use or sell any patented invention that may in any way be related thereto.

# DISCLAIMER NOTICE



THIS DOCUMENT IS BEST QUALITY AVAILABLE. THE COPY FURNISHED TO DTIC CONTAINED A SIGNIFICANT NUMBER OF PAGES WHICH DO NOT REPRODUCE LEGIBLY.

256357

CATALOGED BY ASTIA  
AS AD NO. \_\_\_\_\_

*smyth research associates*

SAN DIEGO, CALIF.

\$9.60

XON  
61-3-2

ASTIA  
RECEIVED  
MAY 11 1961  
TIPER



SMYTH RESEARCH ASSOCIATES  
3555 AERO COURT  
SAN DIEGO 11, CALIFORNIA

FINAL REPORT  
TARGET ACCURACY EXPERIMENT

Prepared under  
Contract AF30(602)-2084

for

ROME AIR DEVELOPMENT CENTER  
Griffiss Air Force Base  
Rome, N. Y.

SRA-172

RADC-TR-61-63

FINAL REPORT  
TARGET ACCURACY EXPERIMENT

Staff

April, 1961

## TABLE OF CONTENTS

	Page Number
I. INTRODUCTION . . . . .	1
II. POINT BUCHON FIELD SITE . . . . .	4
III. DESCRIPTION OF EQUIPMENT . . . . .	7
Antennas . . . . .	7
Receivers . . . . .	9
Frequency Measurement System . . . . .	11
Recorders . . . . .	11
Timing Circuits . . . . .	12
Geophysical Sensors . . . . .	12
IV. EXPERIMENTAL DATA . . . . .	15
V. DATA REDUCTION TECHNIQUES . . . . .	19
Valid Sea Interferometer Interval . . . . .	19
Times of Occurrence of Minima . . . . .	19
Elevation Angles of Minima . . . . .	20
Tide Corrections . . . . .	24
Resolution of Ambiguities . . . . .	25
True Trajectory Computation . . . . .	27
Doppler Fix Method . . . . .	28
Computation of Doppler Frequency Shift . . . . .	29
Comparison With Observed Doppler Data . . . . .	32
Measured Elevation Angle Error . . . . .	24
Effects of Sea Swell . . . . .	25
VI. COMPUTATION OF REFRACTIVE CORRECTIONS . . . . .	38
Range Error . . . . .	41
Doppler Error . . . . .	41
VII. COMPARISON OF MEASURED AND PREDICTED ELEVATION ANGLE ERROR . . . . .	43
Table I . . . . .	44
Table II . . . . .	49
VIII. SHORT TERM FLUCTUATIONS . . . . .	55
Elevation Angle Error . . . . .	55
Range Error . . . . .	57
IX. PRECURSORS . . . . .	60
X. CONCLUSIONS . . . . .	63
XI. RECOMMENDATIONS . . . . .	66

## LIST OF FIGURES

### Figure No.

1	Point Buchon Field Site - Area Location Map
2	Maximum Depression Angle vs Azimuth
3	Profile of Foreground Slope
4	Upper Antenna Area
5	Closeup of D Antenna
6	Instrumentation Layout in Trailer
7	Sample Interferometer and Doppler Records
8	Satellite Trajectory Prediction Chart
9	Idealized Plot of Interferometer Data
10-26	Measured $\delta$ 's vs $\alpha$ 's. Transit Passes
27-37	Measured $\delta$ 's vs $\alpha$ 's. Tiros Passes
38	$\delta$ Computations; Pt. Arguello Radiosonde
39	Maximum-Minimum Interferometer Ratios vs $\alpha$ 's
40	Doppler Fluctuations Tiros
41	Doppler Fluctuations Transit
42	Occurrence of Precursors
43	Precursor Signal Levels

## I. INTRODUCTION

The purpose of the work performed under this contract was to investigate experimentally, the accuracy with which a target moving above the ionosphere can be located and tracked. The principal line of attack on the basic problem has been to measure, by radio techniques, the apparent position of radio satellites as they pass within the line of sight of a ground receiving station, and to compare the apparent position with the true position over a range of elevation angles. These measured deviations are then compared with deviations calculated using available refractive index data which are representative of the area and time in which the measurements were taken. Since it is recognized that these deviations are greatest at low elevation angles, and that it is of greatest importance to detect and track at low elevation angles, the work under this contract has been concentrated on elevation angles below  $15^{\circ}$ .

The basic approach has been to use the sea-interferometer technique for measuring the apparent elevation angle of the satellite versus time during each pass. In order to be able to determine the true trajectory (true elevation angle vs time), during a given pass, simultaneous doppler data have also been obtained. The techniques for using doppler data for establishing the true trajectories is discussed in some detail in Section V. By comparing apparent and true elevation angle as the satellite rises or sets, one obtains a curve of  $\delta$ , the elevation angle error versus  $\alpha_0$ , the apparent elevation angle.

One of the aims of this contract is to determine how well one can compute a curve of  $\delta$  vs  $\alpha_0$  from available refractive index data.

Accordingly, the measured and computed  $\delta$  curves are compared under various refraction conditions, and conclusions are drawn concerning the uncertainties in making angular refraction corrections.

It also has been found possible to relate radar range uncertainties to the observed fluctuations in doppler frequencies, thus enabling one to estimate the degree of reliability with which range error corrections can be made.

It was found during the investigations, that signals could be received from the satellite while it was still several hundred miles below the horizon. These "precursor" signals represent one of the unexpected bonuses of the work done under this contract. They indicate that one can expect to detect missiles, for example, well before they come up over the horizon. Because of the importance of this phenomenon, the characteristics of precursors have been analyzed in more detail, although this work was not originally called for. Recommendations have been made for further investigating the precursor mechanism in order to exploit its use for early detection.

Finally, one can estimate the maximum degree of uncertainty in target location caused by the very rapid fluctuations in  $\delta$ . Such fluctuations limit the depth of observed interference minima because they result in a target having an apparently finite size. While other processes also tend to fill in the minima, one can determine apparent target dimensions,  $\Delta\alpha$ , which can be considered as a safe upper limit, on the basis of maximum observed depth of the minima.

In the process of performing the experimental studies, it has been necessary to build a versatile field facility, including large tracking

antennas, narrow band phase lock receivers, (capable of tracking doppler frequency changes), internal timing standards which need to be locked to WWV only once a day, and multi-channel recording equipment for simultaneously recording interferometer data on several frequencies. The equipment details are described in Section III, and the general description of the Point Buchon Field Site is given in Section II.

As a result of the work performed to date, much valuable information has been obtained, and avenues have been indicated for obtaining much new information for providing answers to basic questions on target location accuracy and early detection. The equipment complex for performing the past work can be readily expanded to perform the new work which is recommended.

## II. POINT BUCHON FIELD SITE

The experimental measurements described in this report were carried out at the SRA field site located on the California coast near Point Buchon. Figure 1 shows the location, about 170 miles northwest of Los Angeles. In selecting this site, several requirements were satisfied. First, it has a wide ( $170^\circ$ ) unimpeded horizon. This is essential for sea-interferometer measurements on a maximum number of satellite passes. Of particular advantage at this site is a clear horizon somewhat east of due south (to  $160^\circ$  azimuth) which allows measurement of a number of satellite sets as well as rises. A second requirement for a sea-interferometer site is a steep foreground slope. The Point Buchon site has a maximum depression angle of  $19^\circ$  to the water's edge. The depression angle exceeds  $10^\circ$  over the range from  $173^\circ - 285^\circ$  azimuth. Figure 2 shows the maximum depression angle in milliradians versus azimuth for the highest antenna site. Since we are concerned with measuring at elevation angles below  $10^\circ$ , these allowable depression angles have been adequate for observing most visible passes occurring in the western half of the sky.

A third important requirement which is offered is a low radio noise environment. The site is located on a private ranch and has very little automobile traffic. Other sources of noise are hidden by mountains to the east. The only interference problem has been occasional radar noise from the Vandenberg Air Force Base area, 50 miles to the southeast. This has interfered with only three out of nearly 70 passes recorded to date.

The availability of commercial power nearby is also a distinct asset, since it affords much better frequency and voltage regulation than is

possible with a portable power plant.

Figure 3 shows a profile of the slope on which four antennas are installed, at locations marked A, B, C, and D. The elevations of the antennas are approximately 270 feet, 300 feet, 760 feet and 860 feet msl, respectively. The lower two antennas (A and B) are 9' x 45' parabolic sectors separated by about 150' horizontally. An instrument trailer is located near the upper of the two. This area is just below an existing ranch road and the commercial powerline. The upper pair of antennas (C and D) are 18' x 45' parabolic sectors and are separated by about 250' horizontally. A second instrument trailer is located near the upper antenna of this pair also. The upper area is about 500 feet higher and 1400 feet northeast of the lower area. Power is delivered to this area via a 1500 foot run of parkway cable (3 - #2 conductors) laid on the ground to reduce powerline noise. Power is supplied to both areas at 480 v - 3 phase for operating the antenna drive motors. A portion is transformed down to 120v single phase for the electronics equipment and other needs.

Both instrument trailers are 18 feet x 8 feet insulated aluminum shells which were made by Masterbuilt Trailer Company in Los Angeles. They were towed to their respective locations, the wheels were removed and each shell was levelled and supported on numerous wooden blocks. Each unit has a thermostatically controlled fan for exhausting air heated by dissipation from the electronic equipment. When the inside air temperature rises above a set level, a vane is automatically moved to direct the heated air outside. In this way the electronics equipment is kept at a reasonably constant temperature, which is important for



maintaining the frequency stability of the various receivers, counters, etc.

Figure 4 shows the C-D area. The two antennas are shown, together with the instrument trailer at the D site. A portion of the half-mile road which was constructed to the area is also shown. On the slope just above the trailer may be seen a radiosonde receiver, which is installed for obtaining on-site refractive index data for the troposphere.

The purpose in laying out the antennas in pairs is to provide two separate sea-interferometers at each of two frequency ranges. Separating the heights of each antenna by about 10%, results in the interference minima in one pattern being displaced significantly from those in the companion pattern. This serves the double purpose of helping to eliminate pattern ambiguities as well as providing twice as many points where apparent elevation is accurately determined. The patterns of the upper pair of antennas have minima spacings of about 6mr at 108mc and 3mr at 216mc. Experience to date has shown that the upper frequency limit for these antennas is probably about 400mc, provided simultaneous lower frequency data are taken to resolve pattern ambiguities.

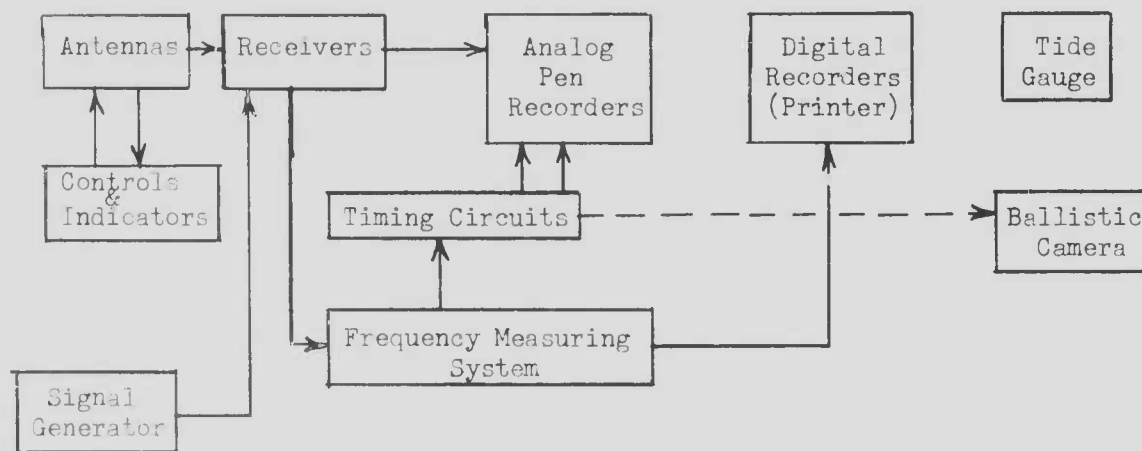
The lower pair of antennas, at roughly one-third the height of the upper pair, have interferometer patterns three times as broad, and therefore can be used up to frequencies of the order of 1200mc.

Measurements to date have been in the 54-324 mc range, such that the upper antenna pair has been adequate. Future work on higher frequencies will necessitate operation of the lower antenna pair. When measurements cover a range of frequencies above and below 400 mc, both

pairs will be operated simultaneously.

### III. DESCRIPTION OF EQUIPMENT

The field site instrumentation at Point Buchon consists of an integrated multireceiver installation with associated antennas, recorders, timing circuits and frequency standards for measuring and recording the apparent elevation angle of satellite radio sources by sea-interferometer techniques. The overall block diagram is indicated below.



Each of the major components of the instrumentation is described below.

#### Antennas

Figure 5 is a closeup view of the D antenna. Details of the mounting, such as the concrete block counterweights are illustrated, together with the 25-foot long feed boom assembly. This assembly is entirely non-metallic. Each boom is a hollow tapered structure made from glued plywood and covered with a 1/8" sheath of fiber glass and resin. The assembly is supported by fiber glass rope. All metallic fittings are located either at the re-

flector face or at the feed structure end of the assembly. The feed structure has five horizontally polarized arrays and one vertically polarized feed. Both the C and D antennas can receive simultaneously on 54, 108, 162, 216, and 324 mc.

The reflectors are constructed of aluminum tubing and faced with expanded aluminum mesh. Each structure was designed to withstand 40mph winds unaided. During nonoperating periods, each antenna is secured to a pair of vertical tubular steel masts, which in turn are guyed by steel cables. When secured in this way, the antennas can withstand winds in excess of 100 mph.

Both the C and D antennas are fully steerable in elevation and azimuth. The mounting was designed to allow continuous  $180^{\circ}$  of elevation tracking. In this way, zenith passes may be tracked without the necessity of rotating  $180^{\circ}$  in azimuth when the satellite passes through the zenith.

The 1 h.p. drive motors are capable of turning speeds of 2 rpm in azimuth and 1 rpm in elevation, although satellite tracking speeds average much slower. The half-power beam widths are about  $14^{\circ}$  (horizontal) by  $35^{\circ}$  (vertical) at 108mc and about half of this at 216mc. Satellite motion in the lowest  $10^{\circ}$  of elevation is such that one can keep the satellite in the beam by shifting azimuth at about one minute or half-minute intervals. To obtain doppler data over the entire pass requires more rapid motion, particularly at nearest approach, but step-wise tracking is still quite satisfactory in this frequency range.

The antenna controls were designed to supply power to the drive motors at either 120 v, 240 v, or 480 v, depending upon the torque requirements. Selsyn indicators are provided in the equipment trailer

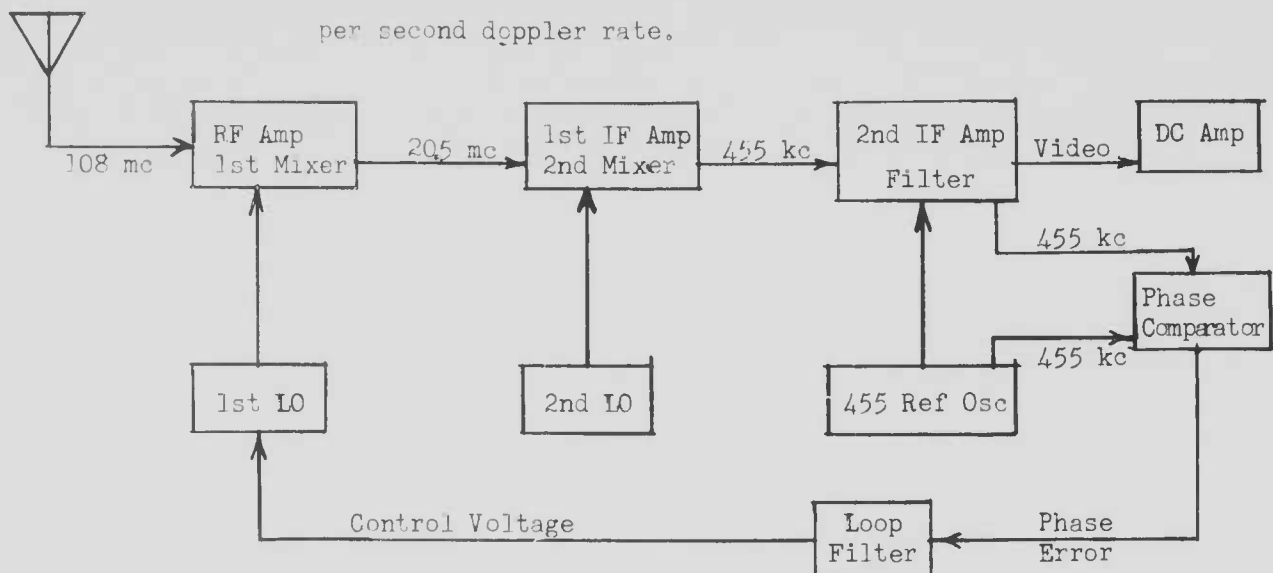
for remotely indicating azimuth and elevation angles of both antennas. In practice, an antenna turning schedule is prepared in advance of each pass, indicating the azimuth and elevation angles to be maintained at each time when a change is required. The operator then uses this schedule for both the C and D antennas; changing to the new positions at the times indicated. Since the operator's post is adjacent to the data recorder, verbal instructions can readily be given if it appears that the satellite is drifting out of the antenna beam.

### Receivers

Twelve receivers make up the receiver complement of the Point Buchon Field Site. These receivers are SRA Modular Receiving Systems. In the configuration used fixed tuned rf amplifier modules and crystal controlled local oscillator modules are used in the receiving systems to allow maximum sensitivity to be realized for the reception of the signals from each satellite tracked. The receivers are used in either of two modes of operation: (1) Fixed tuned, or (2) phase lock frequency tracking. The design and construction of the SRA Modular Receiving Systems allow the required functionally separate units of the receiver to be plugged in to the receiver shell so that all the characteristics of the receiving system can be chosen by appropriate selection of the particular type units to be used. A block and module diagram of one of the phase locked frequency tracking receiving systems is shown below. This receiver has the following characteristics:

- |                            |                        |
|----------------------------|------------------------|
| 1. Frequency of operation  | 107.940 to 108.090 mc. |
| 2. First IF Frequency      | 20.500 mc.             |
| 3. Second IF Frequency     | 455 kcs.               |
| 4. Pre-detection bandwidth | 500 cps.               |

5. Noise figure 2.5 db.
6. Phase locked tuning range  $\pm 5$  kc.
7. Phase error at 20 db S/N ratio;  $15^\circ$  maximum at 50 cps per second doppler rate.



Measurements of the frequency of the received signal as well as the amplitude of the received signal are recorded at the outputs of this receiver. In operation, the receiver tuning tracks the instantaneous frequency of the received signal. Receivers with similar characteristics at operating frequencies around 162 mcs, 216 mcs, and 324 mdc are assembled when different satellites are to be measured, merely by replacing one or two modules in the receiving system. The modular design concept has made practical the taking of measurements on two satellites of different operating frequencies such as Tiros and Transit with as little as 10 minutes available for equipment change-over. The operating frequency of five receivers are changed without sacrifice of the optimum sensitivity or selectivity available in receivers with performance peaked at the operating frequency.

The fixed tuned crystal controlled receivers are assembled with many of the same modules as the phase lock frequency tracking receivers described above. The 455 kcs second IF amplifier employs a 6 kc filter which allows the doppler shift expected in the received satellite signals to be contained in the wider bandwidth system. A block and module diagram of this type receiver is the same as that shown above with the exception that the reference oscillator, phase comparator, and loop filter are not employed.

#### Frequency Measuring System

The frequency of the received signal is measured by electronically counting the operating frequencies of the local oscillator voltages in the super-hetrodyne receiver. Recordings of the doppler frequency are made by digital printing of the counted frequency of the 1st local oscillator which in turn is phase locked to the received signal. The electronic counter used is the Hewlett Packard 5240., shown at lower left, Figure 6.

#### Recorders

Two recording systems are used at Point Buchon to collect the satellite data; (1) an eight channel ink-pen recorder (Offner type RC Dynograph), shown at right center of Figure 6. Each of detected receiver outputs, which are proportional to input signal strength are simultaneously recorded as analog traces on a 16" recorder paper; (2) a digital printer which prints the frequency of a local oscillator phase locked to one of the signals received from the satellite.

Side pens are used on the pen recorder to make second and minute intervals on the paper chart. The time is printed directly on the digital doppler frequency record. Samples of these records are shown

in Figure 7.

### Timing Circuits

A crystal controlled secondary frequency standard is incorporated within the electronic counter, and normally supplies the gating commands to the electronic timer. An output is taken from this frequency standard and divided until accurate one second and one minute impulses are available. Controls are available to vary the frequency divider ratios in order that the timing pulses at the output of the time scales can be brought into synchronism with WWV standard transmissions. These timing circuits control the timing of the electronic counter gate, the second and minute marks on the recorded data, and synchronizing signals to the shutter on the ballistic camera. The equipment is shown at upper left, Figure 6.

### The Geophysical Sensors

Several instruments are available at Point Buchon to measure and monitor the geophysical environment at the site. Among these are:

1. Tide gauge, 2. Ballistic camera, 3. Radiosonde.

### Tide Gauge

The tide gauge is in the form of an air chamber with a filtered opening at the bottom and a pressure connection at the top. The unit is buried several feet below the sand level at a point on the beach above mean tide level. The beach sand serves to filter out individual waves, but allows the averaged sea level at a given time to be established above the chamber. The pressure inside the chamber is transmitted via 1/4" copper tubing to a pressure transducer located well above high tide. This unit is a potentiometer whose sliding contact

is controlled by the input pressure. It has a total range of 0-5 psi, corresponding to a 10 foot tidal range, which is adequate for the Point Buchon coastline. The transducer is part of a battery operated bridge circuit, whose unbalance voltage is nearly linear with the head of water above the air chamber inlet. The output is recorded on a 0-1 ma Esterline-Angus recorder, with a full-scale sensitivity of 0-10 feet of sea water. The bridge, battery and recorder are housed in a watertight box on the edge of the cliff overlooking the beach where the gauge is located. During operations, the chart is checked daily and picked up at the end of each operating period.

An attempt was made to install the air chamber by burying it a foot below the beach level at the water's edge at low tide. This depth of burial was insufficient, and wave action uncovered the chamber a few hours after it was installed. During the operating interval, however, it operated as expected, showing that the principle is a feasible one. A new chamber has been constructed which can be driven into the sand several feet. It is planned to install it further back on the beach at a point where 5 feet burial will place it just below the lowest tide level. No further difficulties are expected in tide measurement.

#### Ballistic Camera

This is a fixed-focus camera with a 20" e.f.l.F-5.6 serial camera lens. It has plate holders for 8" x 10" or 4" x 5" cut film. Using the larger film gives a field of view of  $20^{\circ} \times 25^{\circ}$ . The camera has a rotating paddle just in front of the lens, which is driven by a 1 rps synchronous motor, which is synchronized with the timing ticks provided as described above. The paddle serves to interrupt the satellite



track at known one-second intervals. The complete unit is mounted on a rugged tripod, which allows it to be clamped in any desired position, for photographing various portions of satellite trajectories. Using Royal Pan film, the camera records stars down to 7th magnitude. With fast moving satellites however, 5th magnitude (barely visible) will be required to obtain usable tracks.

#### Radiosonde

The radiosonde equipment installed at Point Buchon is the AN/GMD-1A rawinsonde which automatically tracks a balloon-borne transmitter. The ground equipment can be seen on the slope above the D antenna location in Figure 4. A data recorder is located inside the instrument trailer. It records temperature, pressure and humidity data transmitted by the balloon-borne transmitter. These will be launched at low altitude northwest of the receiver location, such that they can be tracked during all parts of their ascent.

#### IV. EXPERIMENTAL DATA

The basic radio data which are obtained during a given satellite pass are in two forms: (1) a multi-channel graphic recorder chart and (2) a digital print-out paper tape. The interferometer data consist of simultaneous traces of received signal level versus time for each receiver. Normally, two receivers are used for each frequency; one receiver using the C antenna and the other using the D antenna. On Tiros passes only one frequency (108mc) was transmitted, so only two interferometer traces are obtained on these passes. Most Transit passes have at least four traces, two on 216 mc and two on 162 mc. The 54-324 mc transmitters were not operating during most passes, but one trace each was obtained on these frequencies as well, when possible.

As described in the previous section, one receiver on each pass was a phase-lock type, with 500 cps effective bandwidth. Its signal output was recorded as one of the interferometer traces, and in addition, the local oscillator frequency was recorded as a measure of the doppler frequency. One channel of the graphic recorder was used to record the doppler graphically, and in addition, the L.O. frequency was printed out digitally, along with time, at two second intervals on a separate paper tape.

Timing information for the digital tape as well as for time ticks on the multi-channel graphic chart, were derived from a common timing source to preserve accurate time correlation between the two forms of recorded data. Time ticks on the graphic chart were at 1 minute intervals along one margin and at 1 second intervals along the other margin.

A chart speed of 5 mm per second was used during the pass, allowing time interpolation to  $\pm 0.1$  sec. Figure 7 shows a recording of a typical Transit pass. The upper part of the figure shows the multi-channel graphic chart and the lower portion shows a section of the digital doppler data.

In addition to the radio data described above, one needs other data in order to work up each pass.

The exact height of each antenna above sea level is required in order to assign apparent elevation angles to each of the interference minima. The height of each antenna above mean sea level was determined by surveys conducted by a team from RADC. This team installed three bronze survey markers, at locations near each antenna site. The geographic co-ordinates as well as the height above a local bench mark were determined by the team for each of these markers. After installation of the antennas, these markers were used to determine the co-ordinates and heights of the intersection of rotation axes for each antenna.

The heights above mean sea level, as determined above, are then corrected for the tide level during each pass. Tide tables have been used for this purpose, and have been found to be adequate for the  $\pm 0.3$  foot accuracy required. The actual tide level was checked by a survey to the water's edge and was found in agreement with the tide table to within 0.1 feet. It is realized that occasional deviations will occur due to offshore storms, and an attempt was made to install a local tide gauge. Although the attempt was unsuccessful as described in Section III, it is planned to complete the installation in the near future. Meanwhile,

the tide table corrections have been found to be sufficiently reliable for past purposes.

One type of auxiliary data is needed prior to each pass. This is in the form of predicted satellite trajectories, which are required for programming the antenna pointing angles. Since numerous passes occur during any given day, and since the usual observing periods extend over about two weeks, a method was devised which allows the field team to prepare its own pointing schedule for those passes on which it is desired to make measurements.

First, a series of general charts was prepared for each satellite to be utilized. Figure 8 is an example of one such chart. The family of curves with arrow indicates a series of typical trajectories (elevation angle vs azimuth) which the satellite will follow. A circular orbit (zero eccentricity) was assumed for these curves, since the eccentricities of the satellites of interest are relatively small. A second set of curves is superimposed on the trajectory curves. The intersections of these curves with a given trajectory curve indicates the expected position of the satellite at one minute intervals.

In order to specify the trajectory of the satellite during a given pass using these charts, one only needs to know the predicted time, elevation angle and azimuth of one point during the pass. This point is plotted on the appropriate chart, and the remainder of the trajectory can be easily sketched in by interpolation between adjacent curves on the chart. Knowing the time of arrival of the satellite at the given point allows one to estimate the times of arrival at all other points along the pass. If the satellite rises earlier than predicted, the

estimated trajectory is moved eastward by an appropriate amount, knowing that the time intervals between adjacent trajectory curves is 20 minutes. Similarly, if the satellite rises later than expected, the estimated trajectory is moved westward, to account for the earth's rotation during the interval.

In order to preserve the charts for repeated use, it has been found desirable to use an overlay of transparent plastic film, such as Saran Wrap, and plotting the trajectory with a grease pencil. Since Saran Wrap does not adhere well to paper, it is recommended that the charts themselves be laminated in plastic. In this way, the overlay film will adhere to the chart without the necessity of taping.

With the aid of a set of these charts (one for northbound passes and one for southbound passes) for each satellite, the pass predictions need only include one point (usually near rise) for each visible pass occurring during the two week period of interest. These predictions are computed using Space Track orbital data and an electronic computer.

Past experience with Tiros and Transit satellites has indicated that the method described above is adequate for antenna pointing purposes. During the pass, it is occasionally apparent that the satellite is getting a little ahead or behind the prediction, but these cases are easily remedied by leading or lagging the schedule by a small amount. By and large, the method has been quite practical and the accuracy has been all that is required for keeping the satellite in the antenna beam.

## V. DATA REDUCTION TECHNIQUES

### Valid Sea-Interferometer Interval

The first step in the reduction of the interferometer traces, is to determine the limits of the usable data. The criterion in this case is the maximum elevation angle (Figure 2) allowed by the foreground terrain at the azimuth of the particular pass. For this purpose, the antenna pointing schedule is helpful, since it indicates azimuth vs time. By also counting minima, one can roughly determine the approximate elevation angle at various times. When the approximate elevation angle approaches within a degree of the limit set by Figure 2, it is considered that the usable limit is reached. Beyond this point, the phase of the reflected wave will probably be displaced by terrain reflection, such that the elevation angles computed for sea-reflection will be invalid.

### Times of Occurrence of Minima

One next determines the times of occurrence of each interference minimum observed in the valid interval. Most of the minima are sufficiently sharp (see Figure 7) that one can read the times to  $\pm 0.1$  second (0.5 mm on the recorder chart). The minima which are somewhat indistinct ( $\pm 0.3$  second) are tabulated with a question mark, and those which are still more indistinct ( $\pm 0.5$  second or more) are discarded. The time scale established on the recorder chart by the one minute ticks on the upper margin and the one second ticks on the lower margin, is adequate to establish the times of occurrence of minima within the prescribed 0.1 second tolerance. This tolerance was set by the average angular rate of rise, which is about one mr./second and the required angular accuracy of 0.1 mr.

### Elevation Angles of Minima

In order to plot the apparent trajectory (apparent elevation angle vs time) for a particular pass, one needs to determine the elevation angle corresponding to each of the well-defined minima.

In the sea interferometer, the elevation angle corresponding to each minimum is derived as follows:

For a transmitter at infinite distance, the path difference between a direct wave and one which is reflected from the sea surface is

$$\Delta l = 2h_o \sin \alpha_o \quad (1)$$

where  $h_o$  is the height of the receiver above a plane tangent to the earth at the reflection point, and  $\alpha_o$  is the angle of incidence of the reflected wave on the sea surface.

In general, the reflected wave undergoes a phase change  $\phi$ . In order for the direct and reflected waves to arrive at the antenna just out of phase then we require that:

$$\Delta l = (n - 1/2 + \phi/2\pi) \lambda \quad (2)$$

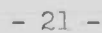
where  $\lambda$  is the wavelength and  $n$  is the order number (1,2,3,etc.) of the minimum.

In the case of a horizontally polarized wave,  $\phi$  is equal to  $\pi$  radians within very narrow limits, regardless of wavelength or angle of incidence. The condition for an interference minimum with horizontal polarization thus becomes:

$$\Delta l = n \lambda$$

Thus we can write:

$$\sin \alpha_o = n\lambda/2h_o \quad (3)$$





$$\alpha_o^4 - \alpha_o^3 n\lambda/2h = n^2 \lambda^2/8ah \quad (5)$$

This quartic is most easily solved numerically using Newton's Method.

#### Large Angles

When  $\alpha_o$  exceeds about 30 mr,  $\tan^2 \alpha_o$  is considerably larger than  $\frac{2h}{a}$ , such that the square root term in (4) may be adequately represented as a three-term expansion:

$$\left[ \tan^2 \alpha_o + \frac{2h}{a} \right]^{\frac{1}{2}} \approx \tan \alpha_o + \frac{h}{a \tan \alpha_o} - \frac{h^2}{2a^2 \tan^3 \alpha_o}$$

Thus (4) becomes:

$$\sin \alpha_o = n\lambda/2h(1 - h/2a \tan^2 \alpha_o) \quad (6)$$

Since the second term in the denominator is small compared to the first, one can use an approximate value of  $\alpha_o$ , in this term to obtain values of  $\sin \alpha_o$  which are accurate to  $\pm .01$  mr. The solutions of (5) and (6) yield values of  $\alpha_o$ , which is the angle of incidence of the reflected wave on the sea surface. It is more convenient to convert this to  $\alpha$ , the angle above the horizontal at the antenna itself. The conversion at small angles is:

$$\alpha = 2\alpha_o - (\alpha_o^2 + 2h/a)^{\frac{1}{2}}$$

At large angles (greater than 30 mr) the correction is small, such that a two term expansion of a square root term similar to that in (4) may be used. In this case:

$$\alpha = \alpha_o - h/a\alpha_o$$

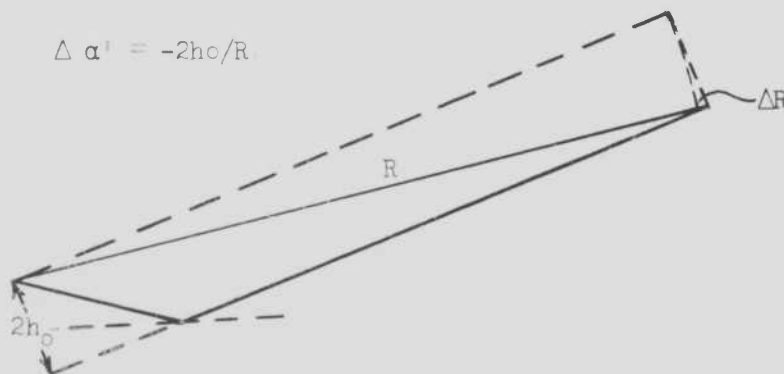
In practice, both (5) and (6) corrected to  $\alpha$  have been tabulated for  $h =$  860 ft. and 760 ft. (the nominal heights of our sea-interferometer antennas,

and for frequencies of 108 mc, 162 mc, and 216 mc. To correct for tidal changes, tabulations are actually made for one foot intervals of antenna height covering the six-foot maximum tidal range expected at the field site. Interpolation can readily be made to  $\pm 0.1$  feet, which brings the accuracy of the elevation angles within 0.1 mr at angles up to 300 mr ( $17.2^\circ$ ).

#### Finite Transmitter Distance

The above expressions were derived assuming parallel direct and reflected rays beyond the reflection point. If the transmitter (or radar target) is at a finite range  $R$ , then two corrections need to be made. First, the elevation angle of the direct ray must be lowered by the angle subtended at the transmitter by the interferometer baseline. This angle is:

$$\Delta \alpha' = -2h_0/R$$



In the figure, we also note that the direct ray is now slightly longer than it would be if it were parallel to the reflected ray. This added path length is:

$$\Delta R = 2h_0^2/R$$

The path difference between direct and reflected rays is now reduced by  $\Delta R$ , which raises the elevation angles of the minima by  $\Delta R/2h_0 = h_0/R$ . Subtracting this effect from  $\Delta\alpha'$  leaves the final correction:

$$\Delta\alpha = -h_0/R$$

The height of a typical satellite used in our studies is about 500 miles.

This gives the following values of  $\Delta\alpha$ :

$\alpha$	$\Delta\alpha$
0	- 0.14 mr
10 mr	- 0.16 mr
100 mr	- 0.20 mr
300 mr	- 0.30 mr

Although these corrections are small, they should be applied for accurate results.

It should be pointed out that  $a$ , the earth's radius which is used in the above expressions should correspond to the curvature of the sea surface at the latitude of the observing station. However, the maximum value of the terms involving  $a$ , is always less than 5 milliradians. Since the maximum variation of  $a$ , over the earth's surface is of the order of 0.4%, one could use a value anywhere in this range and be accurate to within .02 mr. It turns out that the radius of curvature at latitude  $35^\circ N$  is very nearly equal to that of a sphere having the same volume as the earth, namely 6371 km. This was the value used in our computations, and the resulting uncertainty in the elevation angle from this source is certainly much less than 0.01 mr.

#### Tide Corrections

In order to retain the required accuracy of  $\pm 0.1$  mr. in the computed

elevation angles of the minima, over the largest range of angles in the observational data, one needs to establish tide corrections to  $\pm 0.3$  feet. As mentioned earlier, attempts have been made (unsuccessfully) to install a tide gauge near the receiving site. However, the purpose of this gauge was only to detect sea level anomalies caused by offshore storms and high winds. Since these anomalies are rarely more than a few tenths of a foot in amplitude, it is believed that the tide tables offer adequate correction for our purposes. During the attempt to install the gauge, a survey was made from the reference bench mark to the actual water level at low tide, and the measured level agreed with the tide table value to  $\pm 0.1$  foot, the limit of accuracy of the table and of the survey. This agreement confirms the datum correction for the area (difference between mean sea level and mean lower low water) and also confirms our interpolation between two established secondary tide gauges, one about 10 miles southeast and one about 10 miles north of the receiving site coastline. The source of tide correction information which has been used throughout is: "Tide Tables - West Coast of North and South America" published by the U. S. Coast and Geodetic Survey. On the basis of the above considerations, it is believed that the tide corrections made for the passes observed to date have been adequate for maintaining the required 0.1 m accuracy of all measurements.

#### Resolution of Ambiguities

In order to plot a trajectory curve of apparent elevation angle versus time, one must match the elevation angles as computed above with each of the observed minima. In a classic pattern, where all minima are recorded

in an undisturbed way, this is no problem since the first recorded minimum corresponds to  $n = 1$ , the second to  $n = 2$ , etc. However, in the presence of strong refraction, disturbed conditions, or occasionally, failure to record the first few minima for equipment reasons, one is frequently faced with the problem of establishing correct order numbers without having the first few minima as a guide.

In most cases, simultaneous interferometer traces are available from both the C and D antennas. Since the heights are different for these antennas (860' for D and 760' for C), the minima occur at different elevation angles. It turns out that the 9th minimum for the D antenna should occur about 0.2 ms lower (0.2 second earlier) than the 8th minimum for the C antenna. Using this criterion, one can establish these minima and work back to the earliest observed minimum on both traces.

On a few passes, two-antenna data were not taken, but two-frequency data on the same antenna were recorded. In these cases the ratio of order numbers for coincident minima is proportional to the frequency ratios. For example, if data were taken on 162 mc and 216 mc, minimum number 4 on 216 mc would be expected to be coincident with minimum number 3 on 162 mc. Actually, in those cases, since refraction on 162 mc is somewhat more than on 216 mc, one usually finds the third 162 mc minimum a second or two earlier than the fourth 216 mc minimum. Since this method is less certain than the two-antenna method, it was used only when necessary.

There were a few cases where extremely strong refraction occurred, during which the C antenna data indicated a few tenths of a milliradian more refraction than the higher D antenna. In these cases, the ambiguities

were resolved by first establishing the true trajectory and then assigning an order number which gave nearly the expected refraction at the highest elevation angles. Since the minima at the highest frequency (usually 216 mc) are about 2.7 mr apart, and since one knows the expected refraction at high angles to well within this tolerance, resolution of pattern ambiguity could always be accomplished using this means if no others were available.

#### True Trajectory Computation

Having established the apparent trajectory of the satellite within 0.1 mr accuracy during each pass, one must now determine the true trajectory in order to determine the elevation angle errors.

Since the satellite is following an orbit around the earth, one could compute the true elevation angle versus time, if he knew the true orbital elements which apply to each satellite pass. It is recognized that some of the orbital elements issued by Space Track and other agencies are not sufficiently precise to establish the trajectory within the required 0.1 mr accuracy. One of the most crucial elements, and the one subject to the greatest secular variations, is the actual position of the satellite in its orbit. If this position departs by more than 0.1 second from its given value, the resulting trajectory will not be as accurate as required.

This difficulty can be resolved if one has a sufficiently accurate method of fixing the time of passage of the satellite through one known point during the pass. If the remaining orbital elements applying to the pass were known with sufficient accuracy, one could establish the time element by the measured fix point.

### Doppler Fix Method

Since it was realized that most passes would occur at times unfavorable for optical observation of the satellite, and that many satellites are too faint to observe with ballistic cameras or theodolites, even under optimum lighting conditions, a radio fix method was felt to be essential. The method developed for the present applications involved measuring the doppler frequency shift of the received radio signal over as large a portion of the pass as possible. The time of passage through the point of nearest approach can be established within 10 seconds, by determining the time of greatest time rate of doppler change. One then updates the given orbital elements to this time and uses them to compute a curve of doppler shift versus time. The shift in frequency is computed relative to the frequency at nearest approach, which is still unknown. The time scale of the computation is referred to the estimated time of nearest approach, which is known only to the nearest few seconds. However, if the orbital elements used in the computation are correct, the measured and computed doppler curves will have the same shape and by suitable shifting of axes, can be made to coincide over all but the lowest 50 mμ of the pass, where refraction displaces the measured curve by a few cps. If the two curves do coincide over the remainder of the pass (usually at least 10 minutes long), one can be assured that the orbital elements are representative of the pass, and that the true elevation angles calculated using these elements will be valid for the pass.

Matching the two curves in this way, allows one to determine the time of passage of the satellite through the point of nearest approach to

$\pm 0.1$  second and determine the transmitted frequency to  $\pm 2$  cps. The nature of the measured doppler data is sufficiently smooth that there is no difficulty in matching curves to this accuracy.

#### Computation of Doppler Frequency Shift

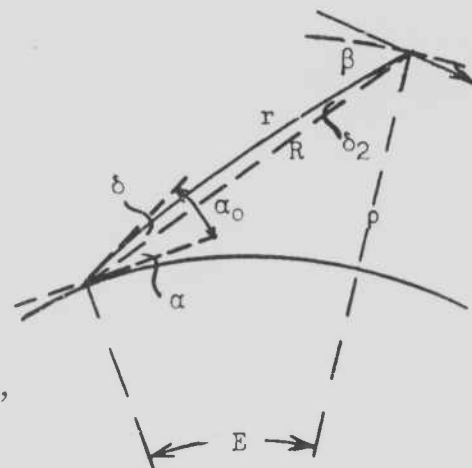
The radio doppler frequency shift caused by a moving transmitter is given by

$$\frac{\Delta f}{f_0} = -\frac{n}{c} \frac{dr}{dt} \quad (7)$$

where  $f_0$  is the transmitter frequency and  $r$  is the range along the curved ray path.

$$\frac{dr}{dt} = \rho \cos \beta \frac{dE}{dt} \sin \beta \frac{d\beta}{dt} \quad (8)$$

where  $E$  is the angle at the earth's center, between the satellite and the receiver.



Applying Snell's law for spherical stratification

$$n_0 a \cos \alpha_0 = n p \cos \beta$$

we have finally:

$$\frac{dr}{dt} = \frac{n_0}{n} a \cos \alpha_0 \left[ \frac{dE}{dt} + \frac{\tan \beta}{\rho} \frac{dp}{dt} \right] \quad (9)$$

Similarly

$$\frac{dR}{dt} = \rho \cos (\beta + \delta_2) \frac{dE}{dt} + \sin (\beta + \delta_2) \frac{dp}{dt} \quad (10)$$

where  $R$  is the straight line range.

Combining (7), (9), and (10) gives:

$$\frac{\Delta f}{f_0} = -\frac{n_0}{c} \left[ \frac{\cos \alpha_0}{\cos \alpha} \frac{dR}{dt} - \frac{a \cos \alpha_0}{\rho} \frac{dp}{dt} (\tan (\beta + \delta_2) - \tan \beta) \right] \quad (11)$$

If both  $\delta$  and  $\delta_2$  are small, (11) becomes:



$$\frac{\Delta f}{f_0} = \frac{-n_0}{c} \left[ \left(1 - \frac{\delta^2}{2} - \delta \tan \alpha\right) \frac{dR}{dt} - \left(\frac{n}{n_0}\right)^2 \frac{p}{a} \frac{\tan \delta_2}{\cos \alpha_0} \frac{dp}{dt} \right] \quad (12)$$

In our computations we actually use

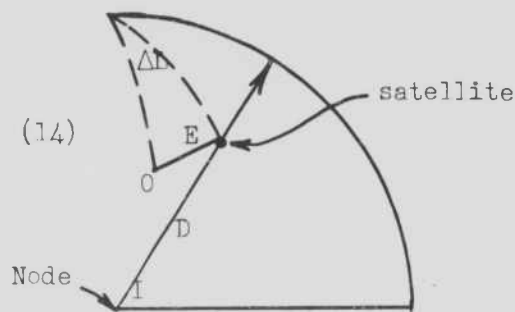
$$\frac{\Delta f}{f_0} = \frac{-1}{c} \frac{dR}{dt} \quad (13)$$

The errors due to refraction (difference between (12) and (13)) are at most 1 cps at 100 mc when  $\alpha_0 = 0$ .

To compute  $\frac{dR}{dt}$  of the satellite, we proceed as follows:

$$R^2 = p^2 + a^2 - 2ap \cos E$$

$$\frac{R}{a} \frac{dR/a}{dt} = \frac{dp/a}{dt} \left[ \frac{p}{a} - \cos E \right] - \frac{p}{a} \frac{d \cos E}{dt} \quad (14)$$



In the figure, O is the observing point at latitude =  $\text{lat}_0$ , and I is the orbit inclination.

$$\cos E = A \sin D + B \cos D$$

$$\text{where } A = \sin I \sin \text{lat}_0 + \cos I \cos \text{lat}_0 \sin \Delta L$$

$$\text{and } B = \cos \text{lat}_0 \cos \Delta L$$

$$\begin{aligned} \frac{d \cos E}{dt} &= (A \cos D - B \sin D) \frac{dD}{dt} + \cos \text{lat}_0 \frac{d \Delta L}{dt} [\sin D \cos I \cos \Delta L \\ &\quad - \cos D \sin \Delta L] \end{aligned}$$

If  $\theta$  is the angular distance of the satellite from perigee and  $r$  is the length of the semimajor axis, and if the orbit follows Kepler's Laws,

$$\frac{dp/a}{dt} = \frac{d\theta}{dt} \left[ \frac{(1-e^2) e \sin \theta}{(1+e \cos \theta)^2} r \right]$$

Furthermore

$$\frac{d\theta}{dt} = \frac{2\pi}{T} (1+e \cos \theta)^2 (1-e^2)^{3/2}$$

Where T is the satellite period and e is the orbit eccentricity.

Also  $\frac{d \Delta L}{dt}$  = earth rotation rate + time rate of change of the R. A. of ascending node.

It is more convenient to change from  $\theta$  to a variable  $\varphi$ , defined as

$$\sin \varphi = \frac{\sin \theta (1 - e^2)^{\frac{1}{2}}}{1 + e \cos \theta} \text{ and } \cos \varphi = \frac{e + \cos \theta}{1 + e \cos \theta}$$

with this substitution, (14) becomes finally

$$\begin{aligned} \frac{d R/a}{dt} = \frac{a}{R} \left\{ \frac{2\pi r^2 a}{T p} \left[ \frac{p}{a} - \cos E \right] e \sin \varphi - (1 - e^2)^{\frac{1}{2}} (A \cos D - B \sin D) \right\} \\ - \frac{p}{a} \cos \text{lat}_o \frac{d \Delta L_o}{dt} [\sin D \cos I \cos \Delta L_o - \cos D \sin \Delta L_o] \end{aligned} \quad (15)$$

In this expression D is actually  $\theta + \omega$  (argument of perigee) and  $\Delta L$  is Long Aries - R. A. of ascending node - Longitude of observer.

The change to the variable  $\varphi$  gives

$$\frac{2\pi}{T} = (t - t_p) = \varphi - e \sin \varphi$$

where  $t_p$  is time of perigee.

#### Computational Procedure

From (15) it will be noted that the dominant term in the one involving  $A \cos D - B \sin D$ , which is zero at  $\tan D = A/B$ . This corresponds closely to the point of zero doppler shift.

It was assumed that the least well known quantity in (15) is D. For this reason, the time of nearest approach is determined approximately from the experimental doppler data (time of greatest rate of doppler change). The value of D is computed at this time as  $\tan D = A/B$  where A and B are determined from given orbital elements. This gives reference values of

$\theta$ ,  $\varphi$  and  $t - t_p$ . Computations are performed at this time and at equally spaced time intervals on either side. For each time interval change  $\varphi$  is determined by

$$\Delta \varphi = \frac{m}{1-e \cos \varphi_0} \left\{ 1 - \frac{m e \sin \varphi}{2(1-e \cos \varphi)} + \frac{m^2}{2(1-e \cos \varphi)^4} [e^2 \sin^2 \varphi - \frac{1-e \cos \varphi}{3} e \cos \varphi] \right\}$$

where  $m = \frac{2\pi\Delta t}{T}$  constant

The new value of  $\varphi = \varphi_0 + \Delta\varphi$  is then used to compute the doppler at the new time. Since the right ascension of the ascending node and the argument of perigee change by at most a few degrees per day, it is assumed that these values are constant during a 20 minute pass.

#### Comparison with Observed Doppler Data

In practice, it is found that the observed curve of doppler frequency versus time rarely matches the computed curve within the  $\pm 1$  cps tolerance allowed by the measured data. Differences of the order of  $\pm 50$  cps are usually found. In order to bring the curves into coincidence, it is necessary to modify the given orbital elements by a small amount. In the case of Transit II, the Applied Physics Laboratory of the Johns Hopkins University re-determines the orbital elements each day. It has been found that even these elements require small corrections in order to apply to the portions of the passes which are visible from our station. Corrections of the nodal right ascension of the order of a few tenths of a degree are usually sufficient to match the doppler data. Occasionally it is necessary to also move the argument of perigee by a degree or two. Using these relatively

small changes the doppler computations of most Transit passes have been brought into coincidence with the observed data to within  $\pm 1$  cps.

In the case of Tiros I, the situation is somewhat different. Since the eccentricity is much lower than for Transit, (.0045 compared to .031) reasonable changes in eccentricity and the argument of perigee are not effective in changing the doppler curve. However, the assumption of constant transmitter frequency during the pass, which is required for a valid doppler match, is not met nearly as well with Tiros as with Transit. This is reasonable, since great pains were taken to design the Transit system with this in mind, whereas the Tiros transmitter was not so designed. Therefore the limit of accuracy with which one can match doppler curves is not as good as the doppler measuring system will allow. On some passes, good matches are obtained with slight changes in nodal right ascension. On other passes, it is evident that the transmitter frequency is drifting by a few cps during the pass, such that one cannot match the entire pass with any one set of reasonable orbit elements. Since one has no way of knowing the way in which the transmitter frequency is changing, one is less certain of the exact orbital elements which apply. On the Tiros passes which are considered to be valid, the match is of the order of  $\pm 5$  cps. In most of these cases the uncertainty in the true elevation angle trajectory is of the order of  $\pm 0.3$  mr or less. During half of the Tiros passes (6 out of 13) which were otherwise suitable for analysis, no reasonable doppler match could be made, indicating a frequency drift during the pass of at least 10 cps. Because of the uncertainty of the true trajectories, these passes were discarded. This situation occurred on only one of the 14

Transit passes during July, when the transmitter was operating properly. During August however, difficulties with the solar batteries deteriorated the Transit frequency stability to the point where only one out of three otherwise suitable passes could be well matched.

From the above discussion one can conclude that the satellite transmitter frequency must be constant during a 15 minute interval to  $\pm 1$  part in  $10^8$  in order to allow computation of the true trajectory to  $\pm 0.1$  mr.

#### Measured Elevation Angle Error

Figure 9 shows an idealized plot of the apparent elevation angle versus time, measured with the sea interferometer. The shaded areas represent the "smeared-out" regions within which the source lies, due to very rapid position fluctuations, and the center dots represent the measured positions corresponding to passage through the minima. It can be seen that the points show second-to-second variations, but the set follows a well defined trend. The solid line in the figure represents the true elevation angle error  $\alpha$  plotted versus time. The elevation angle error  $\delta$  caused by atmospheric refraction of the radio wave, is simply the difference between a given point, and the ordinate of the curve at the same time. The dashed curve represents the predicted trajectory, based on corrections computed as described in Section VI. Figures 10 through 37 are plots of these measured values of  $\delta$  as a function of the apparent elevation angle  $\alpha_0$ . In these plots, the ordinate of scale is ten times the abscissa scale. It can be seen that all of these figures show a similar trend of decreasing  $\delta$  with increasing  $\alpha_0$ . In some of the figures, a distinct difference in

refraction is evident between the two antenna heights. This is attributable to the fact that on these days a strong inversion layer was known to exist at a height about even with the upper antenna. In this situation, the sea reflected wave is bent an additional amount in passing through the inversion layer while the direct wave to the upper antenna is not. The principal effect is that the reflected wave arriving at the antenna has its reflection point moved a little closer to the antenna, resulting in a greater path difference for a given elevation angle of the incoming wave. Thus, the elevation angle where a given minimum will occur is a little less than if the layer were not present. The direct wave to the lower antenna on the other hand will also be bent by the inversion layer, resulting in valid apparent elevation angles in this case. Computation shows that for a strong inversion layer ( $\Delta N = 60$  units) at the antenna height, this effect will result in elevation angles which are about 2.1 mr too low at  $\alpha_0 = 0$ , 0.6 mr at 100 mr and 0.3 mr at 200 mr. Since these are the order of magnitude of the observed differences, as well as the observed  $\Delta N$ 's, it is evident that one should use the values measured at the lower antenna in these cases. For comparison purposes of course, one must compute the  $\delta$ 's with the inversion layer above the antenna, as will be discussed later.

#### Effects of Sea Swell

Another feature of the  $\delta$  plots (Figures 10 through 37) is the presence of a periodic fluctuation, particularly at higher elevation angles. It has been found that the time periods involved are of the order of 15 seconds which corresponds to that of sea swells. The most pronounced effect occurs

on passes where the satellite was to the southwest during the interferometer portion of the pass, although a less distinct effect is also observed on westerly azimuths, with least effect on northwesterly azimuths. The swells were observed to be aligned along a SW-NE orientation, which would make them aligned along the look direction in the most pronounced cases, and normal to the look direction in the least pronounced cases. The distance between crests for a 15 second period is of the order of 1000 feet.

Computation of the size of the first Fresnel zone gives dimensions of the order of 0.1 mile width by one mile length. It is clear that when the long dimension of the zone is aligned with the swell orientation, the average level of the water surface will rise along its entire length as the swell crest passes by, since the Fresnel zone is not wide enough to encompass both the crest and trough simultaneously.

When the look azimuth is normal to the swells on the other hand, several crests and troughs will be illuminated simultaneously, resulting in a periodic residual effect which is much smaller than in the former case.

The effect of sea swells will be greatest at high elevation angles. Since  $\alpha \approx n\lambda/2h$ , it follows that  $\Delta\alpha = \alpha(\Delta h/h)$ . At 200 mr for example, a 2 foot rise in effective sea level will cause a lowering of the minima pattern by 0.5 mr, and at 50 mr, the effect would be about 0.1 mr. The observed periodic fluctuations are in agreement with these figures.

The shape of sea swells is characterized by long flat troughs with relatively short peaked crests. Therefore, the average sea level will correspond more nearly to the level of the troughs than with the crests. It would appear, therefore, that the computed elevation angles of the

minima correspond most closely with the lower water levels (higher angle values). Thus the true measured  $\delta$ 's are just below the peaks of the periodic fluctuations found.

In the top section of Table I the representative measured  $\delta$ 's are tabulated for each pass, at  $\alpha_0$ 's of 150 mr, 100 mr, 50 mr, 20 mr, and 10 mr. These data, together with the remainder of the table will be discussed in Section VII.



## VI. COMPUTATION OF $\delta$ VS $\alpha_0$ FROM ROUTINE REFRACTIVE INDEX DATA

The calculation of refractive effects over a spherical earth with a spherically stratified atmosphere involves knowing the vertical distribution of refractive index. Since this distribution varies considerable both geographically and in time, it is necessary that the computation method be able to handle any given distribution. The method developed by Smyth Research Associates handles this problem in a particularly simple way. The atmosphere is divided into a series of layers, each of which has a linear change of refractive index with height (constant gradient).

In such a layer it can be shown that the refractive bending  $\Delta \gamma$  is exactly:

$$\Delta \gamma = 2(N_B - N_T) \times 10^{-6} / (\tan \beta_B + \tan \beta_T)$$

where  $N$  is the atmospheric refractivity

and  $\beta$  is the angle which the ray makes with the horizontal at a given level.

The subscripts B and T refer to the bottom and top of the layer, respectively.

Similarly it can be shown that the range error, caused by retardation of the ray relative to vacuum velocity, is very nearly:

$$\Delta R = (N_B + N_T) (H_T - H_B) \times 10^{-6} / (\sin \beta_B + \sin \beta_T)$$

where the  $H$ 's are the heights of the top and bottom of the layer.

The derivation of these expressions is straightforward, though somewhat tedious. The reader is referred to the following paper for details:

"Simple Method for Computing Tropospheric and Ionospheric Refractive Effects on Radio Waves", by S. Weisbrod and L. J. Anderson, Proceedings

### Troposphere

To compute tropospheric effects, one uses radiosonde data. These data are in the form of temperature, relative humidity, and pressure at what are termed "significant levels". These levels have been selected during analysis of the original traces, such that between any two adjacent levels, the temperature and/or humidity varies very nearly linearly. These levels then define the boundaries between layers of constant refractive index gradient, as required by the expressions given above. The radiosonde data at each level are converted into refractivity  $N$ , which is  $(n - 1) \times 10^6$  (where  $n$  is the actual refractive index) by the following expression:

$$N = (77.6/T) (P + 4810 e/T)$$

where  $T$  is the temperature in degrees absolute

$P$  is the atmospheric pressure in millibars

and  $e$  is the vapor pressure in millibars.

To complete the conversion, one also needs to determine the height at which each significant level occurs. This information is normally supplied by the meteorologist who works up the original radiosonde trace, or else it can be readily obtained from available tables.

We now have  $N$  values and corresponding heights at each significant level. Next,  $\tan \beta$  is determined at each level, using Snell's law:

$$\tan^2 \beta_h = \left[ \left( 1 + \frac{H}{a} \right) (1 - (N_o - N_h) \times 10^{-6}) \cos \alpha_o \right]^2 - 1$$

One determines  $\tan \beta$  at each significant level for each  $\alpha_o$  of interest.

Using these values and the N values at corresponding heights enables one to compute  $\Delta\gamma$  for each layer whose boundaries are adjacent significant levels. Finally, one sums up the  $\Delta\gamma$ 's for all layers to obtain total  $\gamma_t$  for the troposphere.

### Ionosphere

We must now compute similar values of  $\gamma_i$ , the ionospheric ray bending. The refractive index data we need for this purpose are in the form of ionogram traces, which can be converted to electron density  $N_e$  versus height. The ionospheric refractivity corresponding to a given electron density is also a function of the radar frequency (unlike the tropospheric N's which are independent of frequency.)

The expression for ionospheric refractivity is:

$$N_i = -4.03 N_e \times 10^{-5} / f^2$$

where  $N_e$  is electron density in electrons/meter<sup>3</sup>

and f is the radar frequency in megacycles/second.

The ionosphere is divided into layers of constant N gradient as before and the ray bending is again computed as above.

Having determined  $\gamma_i$  at each  $\alpha_0$ , we now add the tropospheric and ionospheric contributions to obtain:

$$\gamma = \gamma_t + \gamma_i$$

Since we are interested in the elevation angle correction  $\delta$  rather than the ray bending itself, we must correct for the fact that the transmitter (or radar target) is not at infinite distance, where  $\delta$  and  $\gamma$  are equal. We determine  $\delta$  as follows:

$$\delta_H = (\gamma \tan \beta + \gamma^2/2 - (N_o - N_h) \times 10^{-6})/(\gamma + \tan \beta - \tan \alpha_o)$$

In this case, the  $\beta$ 's refer to the height of the transmitter or radar target. They are computed from Snell's Law given in the tropospheric section.

#### Range Error

The radar range error in the troposphere is computed according to the expression:

$$\Delta R \text{ (ft.)} = (N_B + N_T) (h_T - h_B)/1000 (\sin \beta_T + \sin \beta_B)$$

where the h's are expressed in thousands of feet.

Again the  $\Delta R$ 's are computed for each layer and added to give the total  $\Delta R$  for the troposphere.

Ionospheric retardation is computed using the  $N_i$ 's obtained from the ionogram trace. Again the  $\Delta R$ 's are added to give total ionospheric retardation. The total retardation for the entire atmosphere is, of course, the sum of tropospheric and ionospheric contributions.

#### Doppler Error

The doppler frequency shift which one measures after a radio wave has traversed the atmosphere differs from what it would be for a transmitter or radar target moving in exactly the same way, in the absence of an atmosphere. In presence of refractive bending, the measured doppler corresponds to a wave leaving the transmitter or target along the ray path, whereas in absence of refraction, the wave would leave along the straight line path to the receiver. This slight difference in angle is equal to  $\gamma - \delta$ . Therefore,

the doppler error is:

$$\Delta f = (\gamma - \delta) \Delta F$$

where  $\Delta F$  is the measured doppler shift. Since  $\gamma - \delta$  rarely exceeds one milliradian at satellite or missile heights, it follows that the doppler error rarely exceeds 0.1% of the measured doppler.

Measured dopplers are of the order of a few kilicycles, thus, the doppler errors caused by refraction are of the order of a few cycles at most.

## VII. COMPARISON OF MEASURED AND PREDICTED ELEVATION ANGLE ERROR

In table I, the measured values of elevation angle error  $\delta$  are tabulated at apparent elevation angles  $\alpha_0$  of 150, 100, 50, 20 and 10 milliradians. In the next lower part of the Table, the tropospheric  $\delta$ 's computed from radio sonde data taken at Pt. Arguello on the coast 50 miles southwest of the station, are tabulated. Two radiosonde ascents were made each day, and the resulting  $\delta$ 's were computed for the above angles for each ascent. These were then interpolated in time for comparison with measured passes.

The next lower part of the table shows the remaining  $\delta$ , which is the ionospheric component. The succeeding lines of the Table show the predicted ionospheric component, based upon four objective methods.

The first of these involves using the NBS Series D Charts, "Basic Radio Propagation Predictions." These charts allow one to determine the monthly average vertical MUF of the ionosphere corresponding to the point of F layer penetration by the radio wave on each satellite pass. Using these data and the method described in SRA Report 91, one can estimate the expected ionospheric component of  $\delta$  for each frequency.

The second set of predictions utilizes ionogram data measured at White Sands, New Mexico, and Boulder, Colorado, on the days the passes occurred. Such data are taken at 15 minute intervals, and the ionograms measured closest to the same local time as that corresponding to ray penetration of the ionosphere on each pass, were used to compute individual ionospheric refraction components. The assumption which is made is

TABLE I  
COMPARISON OF MEASURED AND PREDICTED ELEVATION ANGLE ERROR

Pass No.	<u>Transit Passes</u>											
	2	11	12	15	16	17	25					
Freq. (mc)	216	162	216	162	216	216	162	216	162	216	162	216
$\alpha_o$ (mr)	Measured $\delta$ in milliradians											
150			5.9	3.8	4.1	7.1	4.1	5.1	4.6	5.7	4.3	
100	3.4		4.7	7.6	5.2	4.6	8.0	5.0	6.0	5.3	6.7	5.2
50	5.6		6.5	10.5	8.0	6.8	10.3	7.6	8.1	7.2	9.7	8.1
20	8.1	11.0	10.2	16.4	13.1	10.3	18.8	13.4	12.4	11.3	14.7	13.4
10	10.1		13.2			14.0				16.8		
	Tropospheric $\delta$ Computed from Radiosonde Data											
150	2.0	2.0		2.0	2.0	2.0		2.0		2.0		
100	2.9	2.9		2.8	2.8	2.8		2.8		2.9		
50	5.0	5.0		4.7	4.9	5.0		5.0		5.0		
20	8.7	8.8		8.1	8.6	8.8		8.8		8.8		
10	11.8	12.9			12.6			13.2				
	Ionospheric Component (Measured minus Tropospheric)											
150			3.9	1.8	2.1	5.1	2.1	3.1	2.6	3.7	2.3	
100	0.5		1.8	4.8	2.4	1.8	5.2	2.2	3.2	2.5	3.8	2.3
50	0.6		1.5	5.8	3.3	1.9	5.3	2.6	3.1	2.2	4.7	3.1
20	-0.6	2.2	1.4	8.3	5.0	1.7	10.0	4.6	3.6	2.5	5.9	4.1
10	-1.7		0.3			1.4				3.6		
	Predicted Ionospheric Components (Average 10-150 mr)											
NBS Series D	1.0	1.8	1.0	1.9	1.0	1.0	1.9	1.0	1.7	0.9	1.5	0.8
Ionogram		0.8	0.5	0.8	0.5	0.5	2.1	1.2	1.9	1.1	1.1	0.6
Meas. $\alpha_o$ diff		1.8	1.0	5.3	3.0		6.9	3.9	1.6	0.9	3.4	1.9
Meas. $\delta$ 's	0.5	3.2	1.8	3.6	2.0	2.1	4.6	2.6	3.6	2.0	3.8	2.2

TABLE I (Cont'd)

Pass No.	26		28(set)		29		30		31(rise)		31(set)
Freq. (mc)	162	216	162	216	162	216	162	216	162	216	216
$\alpha_0$ (mr)	Measured $\delta$ in Milliradians										
150	4.6	2.9		5.2	5.2	3.5	5.3	4.7			
100	6.2	4.2		6.4	6.0	4.4	6.1	5.5			5.4
50	9.2	7.2	12.1	9.1	8.7	6.8	7.6	6.7	7.3	6.2	8.3
20	13.7	11.4		14.8	12.8	11.0	11.3	10.0	11.8	10.7	13.7
10							14.8	13.9		13.9	
Tropospheric $\delta$ Computed from Radiosonde Data											
150	2.0		2.0		1.9		1.8		1.8		1.8
100	2.9		2.9		2.8		2.7		2.6		2.6
50	5.0		5.0		4.8		4.7		4.5		4.5
20	8.8		8.8		8.2		8.0		7.5		7.5
10							11.9		10.0		
Ionospheric Component (Measured minus Tropospheric)											
150	2.6	0.9		3.2	3.3	1.6	3.5	2.9			
100	3.3	1.3		3.5	3.2	1.6	3.4	2.8			2.8
50	4.2	2.2	7.1	4.1	3.9	2.0	2.9	2.0	2.8	1.7	3.8
20	4.9	2.6		6.0	4.6	2.8	3.3	2.0	4.3	3.2	6.2
10							2.9	2.0		3.9	
Predicted Ionospheric Components (Average 10-150 mr)											
NBS Series	1.6	0.9	2.7	1.5	1.6	0.9	1.8	1.0	1.5	0.8	1.5
Ionogram	1.1	0.6	1.7	1.0	1.1	0.6	1.1	0.6	1.1	0.6	
Meas. $\alpha_0$ diff	4.3	2.4	6.9	3.9	4.0	2.3	2.1	1.2	2.5	1.4	
Meas. $\delta$ 's	2.2	1.2	5.7	3.2	3.1	1.7	4.0	2.3	2.8	1.6	2.8



TABLE I (Cont'd)

Pass No.	32		33		36(rise)		36(set)		
Freq. (mc)	162	216	162	216	162	216	324	162	216
$\alpha_0$ (mr)	Measured $\alpha_0$ in Milliradians								
150	5.6	4.1	4.2	3.4	5.7	4.5		4.9	3.1
100	6.4	4.7	5.2	4.6	6.7	5.7	4.9	6.0	4.1
50	8.5	6.5	7.2	6.8	9.3	8.3	7.4	7.9	6.1
20	13.0	11.2	11.2	10.5	12.8	11.8			9.2
10			15.5	14.6	15.5	15.0			12.6
Tropospheric $\delta$ Computed from Radiosonde Data									
150	1.9		1.9		2.0			2.0	
100	2.8		2.8		2.9			2.9	
50	4.9		4.9		5.0			5.0	
20	8.4		8.4		8.7			8.7	
10			12.2		12.7			12.7	
Ionospheric Component (Measured minus Tropospheric)									
150	3.7	2.2	2.3	1.5	3.7	2.5		2.9	1.1
100	3.6	1.9	2.4	1.8	3.8	2.8	2.0	3.1	1.2
50	3.6	1.6	2.3	1.9	4.3	3.3	2.4	2.9	1.1
20	4.6	2.8	2.8	2.1	4.1	3.1			0.5
10			3.3	2.4	2.8	2.3			-0.1
Predicted Ionospheric Components (Average 10-150 mr)									
NBS Series D	1.5	0.8	1.8	1.0	2.0	1.1	0.5	2.8	1.5
Ionogram	1.4	0.8	2.2	1.2	2.4	1.4	0.6	3.0	1.7
Meas. $\alpha_0$ diff	4.1	2.3	1.4	0.8	2.3	1.3	0.6	4.1	2.3
Meas. $\delta$ 's	3.7	2.1	2.5	1.4	3.9	2.2	1.0	2.5	1.4

TABLE I (Cont'd)

Tiros Passes (108 mc)

Pass No.	1	3	5	40	41	43	47R	47S	57	59R	59S	61
$\alpha_o$ (mr)	Measured $\delta$ in Milliradians											
150		5.3		4.1	3.3		4.9	9.3				
100	6.6	6.7	6.4	6.1	4.4		7.4	10.5	8.7			6.0
50	8.6	8.9	8.5	9.5	7.8	11.0	10.3	13.6	12.6	9.3	11.2	9.2
20	11.2	13.3	11.7		12.1	15.8	15.3	16.6	16.1	14.3	17.4	14.1
10	12.9		13.4			22.3	21.8	19.5				17.8
Tropospheric $\delta$ Computed from Radiosonde Data												
150	2.0	2.0	2.0	2.1	2.1	2.1	2.0	2.0	2.1	2.1	2.1	2.1
100	2.9	2.9	2.9	3.0	3.0	3.0	2.9	2.9	3.0	3.0	3.0	3.0
50	4.9	5.0	5.1	5.1	5.1	5.1	5.0	5.0	5.1	5.1	5.1	5.1
20	8.6	8.7	8.8	8.7	8.7	8.7	8.7	8.7	9.1	9.1	9.1	8.6
10	12.2		11.5			11.8	11.8	11.8				11.3
Ionospheric Component (Measured minus Tropospheric)												
150		3.3		2.0	1.2		2.9	7.3				
100	3.7	3.8	3.5	3.1	1.4		4.5	7.6	5.7			3.0
50	3.7	3.9	3.4	4.4	3.7	5.9	5.3	8.6	7.5	4.2	6.1	4.1
20	2.6	4.6	2.9		3.4	7.1	6.6	7.9	7.0	5.2	8.3	5.5
10	0.7		1.9			10.5	10.0	7.7				6.5
Predicted Ionospheric Component (Average 10-150 mr)												
NBS Series D	3.6	3.6	3.6	1.8	2.1	3.2	4.7	7.2	4.3	4.9	6.8	2.1
Ionogram				0.9	1.1	2.5	6.6	8.0	2.9	3.6		1.4

that the ionospheric structure is only a function of local time (solar elevation angle) and that other random changes over a two hour period are negligible.

The geomagnetic latitude of White Sands is the same as Pt. Buchon, and that of Boulder is  $10^{\circ}$  further north. Thus on nearly westerly look angles, the White Sands data were used, and on northwesterly angles, Boulder data were used. There are no nearby ionosonde stations whose geomagnetic latitude is about  $10^{\circ}$  south of Pt. Buchon; south and southwesterly passes are therefore apt to be underestimated, since electron density is usually higher at lower latitudes.

The detailed ionospheric computations were made in accordance with procedures outlined in the previous section.

The third prediction method requires measured  $\alpha_o$  data at two frequencies. From the measured differences in  $\alpha_o$  at these frequencies, and the assumption that the ionospheric  $\delta$  is inversely proportional to the frequency squared, one can determine the ionospheric  $\delta$  at each frequency.

The fourth method requires measured  $\delta$ 's at two frequencies, and is in reality a measure of the self-consistency of all passes and of the  $\frac{1}{f^2}$  assumption.

In Table II the average residual error for all passes where the required data were available, is tabulated at several elevation angles, for each of the four methods described above. The numbers in parentheses are averages of less than 6 passes, and are therefore not reliable. It can be seen that all of the prediction methods give residual errors which usually increase with decreasing frequency and with decreasing  $\alpha_o$ . The

TABLE II  
AVERAGE RESIDUAL ERROR IN  $\delta$ (mr.)

$f(mc)/\alpha_0$ (mr)	10	20	50	100	150
Radiosonde and Series D					
108	3.5	1.7	1.3	0.6	0.7
162	(1.1)	2.9	2.2	1.8	1.6
216	1.7	2.2	1.3	1.2	1.2
Radiosonde and Ionogram					
108	(4.2)	2.4	2.4	1.5	1.4
162	(1.1)	3.4	2.5	1.9	1.8
216	1.5	2.3	1.5	1.2	1.2
Measured $\alpha_0$ Differences					
162	(1.1)	1.6	0.8	1.0	1.2
216	1.5	1.3	0.8	1.0	1.1
Measured High Angle $\delta$ 's					
108	3.1	1.7	1.3	0.7	0.0
162	(1.0)	1.7	0.8	0.4	0.3
216	1.3	1.4	0.5	0.3	0.2

two-frequency measured  $\alpha_o$  differences, yield residual errors which are appreciably less than the Series D method, and which are reasonably the same at both frequencies. Finally, the self-consistency test, labelled "Measured High Angle  $\delta$ 's", shows residual errors which are much smaller at high angles, but about the same at low angles.

From the data indicated in the lower sections of Table II, one can conclude that the  $\frac{1}{f^2}$  assumption is well substantiated by the measurements. Furthermore, the self-consistency of the two-frequency (Transit) passes is good ( $\pm 0.3$  mr) at high angles and the results increase as the elevation angle decreases. This indicates that the tropospheric component predictions are underestimated, since ionospheric  $\delta$ 's are almost constant over the measuring interval.

It is further apparent that the individual ionogram based predictions are no better than those based on monthly averages of the NBS Series D circular, and are if anything somewhat worse. The only conclusion one can draw from this comparison is that the assumption negligible random ionospheric structure changes over a two hour interval is not as valid as the assumption that our passes occurred during conditions which were close to the monthly average. Another factor which undoubtedly contributed to the underestimation of the ionogram  $\delta$ 's is the previously mentioned lack of data for southerly passes.

It appears that the only way in which to improve the ionospheric predictions would be to have ionogram data taken near the actual region where the ray paths penetrate the F layer. Since this takes place in

a ring between 750 and 1100 miles from the station and at azimuths from 160 to 325, this would be difficult to accomplish by vertical incidence soundings. However, the use of the oblique incidence technique from the station at Stanford would provide ionospheric information from the actual penetration region. Since the times and look directions of satellite passes can be predicted with adequate accuracy for two weeks or more, it would be possible to schedule times and azimuths for the oblique incidence soundings well in advance, to insure obtaining the required ionospheric data, without the necessity for a blanket coverage during the expected days of pass observation. It is suggested that this approach be investigated, since it represents about the best one can hope to do in obtaining ionospheric information for refraction predictions.

As mentioned earlier, the tropospheric component was computed from radiosonde data taken twice a day at a point 50 miles away from the receiving site. Inasmuch as the ray paths in the crucial lowest 30,000 feet of the atmosphere occupy about 200 miles in length, it would seem that the 50 miles separation would not be significant. Since both locations are on the coastline, the measured profile would be as representative of the ray path whether the data were taken at Pt. Arguello or at Pt. Buchon. One advantage may well result from a sounding taken near the actual time of the measured pass. Whether or not the hour-to-hour changes measured at the site would be reflected in similar changes throughout the important tropospheric part of the ray paths, remains to be seen. Radiosonde equipment is installed at the field site for obtaining these data, but during

the period of the measurements reported herein, was not in operating condition. Future passes which are measured will be accompanied by on-site radiosonde data in order to test this point.

The results shown in Table II indicate that the radiosonde-derived tropospheric corrections are generally too small at low elevation angles. This is typical of strong refraction conditions.

It was realized that the radiosonde sensing elements (particularly the humidity strip) have appreciable lag coefficients, and therefore tend to indicate inversion layers which are thicker and more diffuse than they actually are. This behavior would result in  $\delta$ 's which are too small at low elevation angles, as is evident in Tables I and II. In reducing the radiosonde data, therefore, compensation was made for the lag in the humidity strip. It was assumed that above the base of the inversion layer the vapor pressure decreased as rapidly as the temperature increased, and reached its equilibrium value at the top of the inversion layer. The vapor pressure value used was the equilibrium value at the top of the inversion layer. The vapor pressure value used was the equilibrium value which was indicated at a height 500 to 1,000 feet above the top of the inversion layer. It is felt that most of the effects of strip lag have been eliminated by this procedure. The lag of the temperature element at the customary rise rate of 1000 ft/minute is about 5 seconds. Its effect is to lower the inversion layer by 100 feet at most, which has no appreciable effect on the resulting  $\delta$  values.

Figure 38 is a plot of the computed  $\delta$ 's versus  $N_0$ , and indicates the variability caused by the shape of the individual N profiles. It can be

seen that at 200 mr, the computed  $\delta$ 's average about .02 mr above the standard atmosphere with a variability of  $\pm .01$  mr. At 100 mr, the corresponding figures are + .03 and  $\pm .02$  mr respectively. Even at an elevation angle as low as 50 mr, the actual profile shapes yielded average  $\delta$ 's only 0.1 mr above the standard atmosphere with a variability of  $\pm .05$  mr. At angles of 50 mr and higher, therefore, one could conclude that the effects of the strong refraction conditions encountered are quite small, and can be well accounted for by standard atmosphere corrections with a small systematic increase; or by corrections based upon  $N_0$  alone.

At 10 mr and 20 mr, the layer effects become progressively more pronounced. The detailed  $\delta$  computations give values generally from 0.5 to 1 mr higher than the standard atmosphere at 20 mr and 1 to 3 mr higher at 10 mr. The profile-to-profile variability is  $\pm 0.2$  mr at 20 mr and  $\pm 0.6$  mr at 10 mr.

It should be realized however, that these comparisons are between standard atmosphere profiles and the moderate-to-strong refractive profiles measured by the Pt. Arguello radiosonde (corrected for lag as described above). The Table II data indicate the corresponding additional differences between observed  $\delta$ 's and those shown in Figure 38.

Thus at 10 and 20 mr, while the computed  $\delta$ 's are about 2.0 and 0.7 mr higher than standard respectively, the observed  $\delta$ 's are an additional 1.4 mr higher. At 50 mr we must add about 0.8 mr to the 0.1 mr computed excess over standard. At higher angles the average residual tropospheric corrections are about 10 times the profile-minus-standard differences.



In summary then, one can conclude that comparisons such as that shown in Figure 38 tend to give one a false sense of security about the accuracy with which corrections can be made for tropospheric refraction. The actual uncertainty at angles above 50 mr is of the order of 10 times as much as one would expect on the basis of N profile computations alone. At lower angles the ratio decreases to about two to one, but the absolute value of the uncertainty about doubles in going from an  $\alpha_0$  of 50 mr to 10 mr.

These comparison were made, of course, under strong to moderately strong refraction conditions and as such, represent about the worst uncertainties one can expect to encounter.

## VIII. SHORT TERM FLUCTUATIONS

### Elevation Angle Error

Examination of Figures 10 to 37 indicates that the second-to-second fluctuations in  $\delta$  at 108 mc are of the order of  $\pm 1$  mr at elevation angles from 0 - 20 mr and  $\pm 0.5$  mr at 50 mr. Corresponding values at 216 mc are 0.4 mr and 0.2 mr. The presence of sea-swell fluctuations at higher angles makes it difficult to estimate the fluctuations at  $\alpha_0$ 's greater than 50 mr, but it is certain that they will decrease rapidly with increasing  $\alpha_0$ . At  $\alpha_0$ 's greater than 150 mr, the fluctuations are probably smaller than the 0.1 mr resolution of the measuring system.

One can, however, draw certain conclusions about very rapid fluctuations in  $\delta$  by examining the max-min ratio of the interference patterns. If one had a point source of radiation and a smooth reflecting surface with unity divergence factor, the depth of individual minima would be limited only by the receiver noise level. At low elevation angles, however, the divergence factor is less than unity and increases as  $\alpha_0$  increases. The effect of wave height on the amplitude of the reflected component on the other hand is small at low angles and increases with  $\alpha_0$ . Figure 39 shows the greatest max-min ratio achievable as a function of  $\alpha_0$ , for various ratios of wave height to radio wavelength. At 108 mc ( $\lambda = 9.1$  ft), a wave height of 4.5 ft. would limit the ratio to 16 db for the lowest minimum, but the ratio increases to a maximum of 32 db at  $\alpha_0 = 37$  mr. Measured max-min ratios of as much as 30 db are frequently observed although ratios as little as 18 db are also seen.

If, instead of being a point source, the apparent elevation angle of

the satellite fluctuated very rapidly (with millisecond periods) the source would appear to have a finite angular width  $\Delta\alpha$ . In this case the max-min ratio would be limited by  $\Delta\alpha$ , and one should be able to draw conclusions about the maximum value of  $\Delta\alpha$  from the observed ratios.

One can show that under ideal reflection conditions the max-min ratio would be:

$$R = (\pi h / \lambda)^2 (\cos \alpha_0 \Delta\alpha - 2 \sin \alpha_0 \Delta\lambda)^2$$

Where  $h$  is the height of the antenna above the reflecting surface,  $\lambda$  is the wavelength, and  $\Delta\lambda$  is the wavelength spread caused by the radio bandwidth. In our system, we can use  $h = 860$  ft. and a bandwidth of 500 cps. This gives  $\Delta\lambda = 5 \times 10^{-5}$  ft. at 100 mc and  $1.2 \times 10^{-5}$  ft at 216 mc. At  $\alpha_0 = 200$  mr,  $\Delta\alpha$  of 1 mr would thus correspond to an  $R$  of 5.2 db at 216 mc and 11.2 db at 108 mc, and a  $\Delta\alpha$  of 0.1 mr would correspond to an  $R$  of 25.0 db at 216 mc, and 29.8 db at 108 mc. Thus the minimum observed  $R$  of about 18 db corresponds to a  $\Delta\alpha$  of the order of 0.2 mr at 216 mc and 0.5 mr at 108 mc. The maximum  $R$  of about 30 db corresponds to a  $\Delta\alpha$  of 0.05 mr at 216 mc and 0.1 mr at 108 mc. The fact that  $R$ 's of as much as 30 db have been observed indicates that  $\Delta\alpha$  cannot be greater than the minimum values cited above. If it were greater than this, for a given pass no  $R$  would be as great as 30 db. The fact that some  $R$ 's less than this are observed can be attributed to fluctuations in sea roughness and other causes not related to the atmosphere. It is therefore concluded that the common occurrence of 30 db max-min ratios indicates a maximum millisecond fluctuation amplitude in  $\delta$  order of 0.1 mr and 0.05 mr at 108 mc and 216 mc respectively even at elevation angles as low as 30 mr.

### Range Error

The doppler data, which were originally taken for radio fix purposes, are also a very sensitive means of determining range error fluctuation rates. If one imagines a wave penetrating a section of the ionosphere with a given integrated electron count (between the transmitter and the receiver), the retardation of the wave will be proportional to the integrated count. If now the ray path sweeps through an ionospheric blob having a higher electron density, the retardation will increase, causing a decrease in doppler frequency which would be proportional to the gradient in retardation normal to the ray path. For example, if the range error were 3 km during a given one second interval, and if it increased by 1% during the next one second interval, the apparent range change rate would be 1% of 3 km = 30 meters per second. This would correspond to a doppler shift of  $\frac{30}{3 \times 10^8} = 10^{-7}$ , or 10 cps at 100 mc. Since the doppler caused by motion of the satellite is a smooth function of time, one can easily distinguish the second-to-second departures caused by electron density gradients from the doppler caused by satellite motion.

Figures 40 and 41 illustrate observed doppler fluctuations on two passes of Tiros and Transit respectively. Several other such passes have been plotted, and the results are similar to those shown. It is seen that during most of the pass which is above the horizon, the average fluctuation is of the order of  $\pm 2$  cps at 108 mc and  $\pm 1$  cps at 216 mc.

The data plotted in Figures 40 and 41 are actually the differences between the received frequency averaged over a given one second interval and that averaged over a succeeding one second interval starting a second

beyond the first interval. Thus one has averaged readings spaced two seconds apart. Each pass is plotted in two parts in order to spread out the time scale. The pass starts in each case at the left ordinate, near the zero difference line, and proceeds across the width of the figure. The remainder of the pass starts again at the left ordinate (at a value of -10 to -20) and continues across the figure. The average fluctuation rates shown, indicate rates of change of range error of the order of 3 meters per second at 108 mc and 0.8 meters per second at 216 mc.

In general, the fluctuations are reasonably random, although one occasionally finds several consecutive intervals during which the doppler rate is consistently below average or above average. This would indicate that the range error probably fluctuates about the mean value with as much as  $\pm 30$  meter and 9 meter deviations at 108 mc and 216 mc respectively over periods of 10 seconds.

These are occasional intervals (Figure 41) where the doppler fluctuations exceed 5 cps per second, indicating deviations of the order of 30 meters in a two second interval. In one case (just before the geometric horizon point, Pass 16, Figure 41) a cumulative range deviation of 12 meters was reached before it swung back.

As pointed out above, these range error deviations are visualized as being caused by the ray path sweeping through blobs with higher or lesser electron density than their surroundings. It appears from the observed doppler data however, that when averaged over one second intervals, the ionosphere is remarkably smooth. This means either that the electron density gradients take place over distances of many tens of miles

such that the gradients themselves are low, or that there is a very fine grain structure (less than a mile in extent) which is averaged out during the one second counting interval.

There will, of course, always be some averaging because of the finite length of the Fresnel zone, which at 108 mc is of the order of 6 miles by one mile in dimensions at low elevation angles, 3.7 miles by one mile at 300 mr, and one mile by one mile at the zenith. These dimensions assume a satellite height of 500 miles and the ionospheric "layer" height at 300 km. Since the satellite velocity is roughly 4.5 miles per second, one could obtain a resolution of a mile by recording doppler data at 0.2 second intervals instead of one second intervals. At 216 mc, the Fresnel zone dimensions are reduced to 0.7 of the above values. Still higher frequencies would have smaller Fresnel zone sizes, but would also be less sensitive to electron density gradients. It would appear that 216 mc would allow one to obtain optimum overall resolution of range error fluctuations, of the order of 0.7 miles. Doppler resolution of 0.2 cps in a time interval of 0.2 second would allow one to detect range error rate changes from mile-to-mile of the order of one meter per second.

## IX. PRECURSORS

One of the results of the investigations described in this report was quite unexpected. This was the detection of signals many minutes before the satellite rose above the horizon, or after it had set. The strength of these "precursors" is occasionally within a few db of the free space levels. The more distant signals usually rise above the detection level for a few seconds and then fade out for a minute or more and recur again at closer range. The signals do not show any rapid fading structure (within the .01 second response of the recorder). Occasionally there is a slower fading period of a second or so with fades of the order of a few db, suggestive of a multipath mechanism.

Out of a total of 47 passes during which these signals would have been detected, they actually appeared on 35. In Figure 42, the times of rise or set are plotted versus azimuth. The purpose of this plot was to determine whether the pattern would be as one would expect for an ionospheric mechanism. Characteristically, the MUF of the ionosphere decreases north of the station latitude ( $35^{\circ}\text{N}$ ) and increases to the south. It is also at a minimum at midnight. If the ionosphere were responsible therefore, one would expect the "no-show" passes to occur toward the north or at night. The data plotted on Figure 42 suggests such a pattern, but there are some inconsistencies where a precursor was detected at a particular time and azimuth during one day and not on the next. This would be expected if, as the measured  $\delta$  data indicate, the horizontal pattern of MUF varies considerably from day to day.

In Figure 43, the level of the precursor peaks is plotted versus the distance of the satellite below the radio horizon of the receiver. This distance was computed along the line connecting the satellite and receiver locations at the time of precursor occurrence. The ordinate is expressed in db below the free space level at a distance corresponding to the first two or three maxima in the interferometer pattern. The free space level to this point could be established since at the maximum the signal should have been about 5 db above free space because the direct and reflected waves add in phase at these points.

It can be seen that the most distant signals were received when the satellite was nearly 2,000 miles beyond the radio horizon, and that the signal levels were 10 and 18 db below the free space level at this distance. Several other signals were detected at 1200 mile ranges, including one case just 2 db below free space.

In examining these data, no well defined frequency dependence is evident. While most of the long range signals were at the higher frequencies, some of them show 162 mc stronger than 216 mc and others are reversed. If the ionosphere were responsible as the propagation mechanism, one would expect the 108 mc signals to be much more predominant than those at higher frequencies.

Correlation of the dates of precursor occurrences with radiosonde data suggests that tropospheric ducts are probably responsible for the observed signals. On the days when the strongest inversion layers were present, the precursors were strongest and most persistent. During



days of relatively weak inversion layers, the precursors tended to be weak or absent.

Since most of the observations were made in the presence of inversion layers, it is desirable to extend them to a wider variety of conditions in order to observe, for example, whether precursors ever occur in the absence of such layers. Once the precursor mechanism has been positively identified, it will be possible to estimate the early detection possibilities of this phenomenon in various areas of operational importance.

## X. CONCLUSIONS

The work which has been described in this report has led to several conclusions regarding the accuracy with which one can correct for atmospheric refractive effects on precision location of objects above the ionosphere.

1. The average total elevation angle error measured during this work is shown in the following table:

TABLE III  
Average  $\delta$ 's

freq \ $\alpha_0$	10	20	50	100	150
108	18.0	14.4	10.0	7.0	5.4
162	15.3	13.3	9.0	6.4	5.4
216	13.8	11.4	7.2	4.9	4.0

2. The correction of elevation angle errors, using nearby radio-sonde data and NBS monthly ionospheric predictions as well as daily ionogram data, leaves residual errors averaging  $\pm 1.3$  milliradians at angles above  $3^\circ$ . Corresponding values at  $1^\circ$  are 2.5 mr.
3. Much of this residual error is caused by space and time variations in the ionosphere, which are not derivable from the monthly average ionospheric predictions or from daily ionogram data taken 1000 miles away. Measured differences in elevation angle at two frequencies allow one to evaluate ionospheric corrections which reduce the residual errors appreciably from the values given above.

4. Further analysis shows that the remaining part of the residual errors at low angles (1 to 3 degrees) is attributable to under-estimation of tropospheric refraction in spite of compensating for a lag of the radiosonde sensing elements.
5. The self consistency of 14 passes where two-frequency data were available indicates residual errors of 0.3 milliradians at angles above  $5^{\circ}$ .
6. Second-to-second fluctuations in apparent elevation angle at 108 mc average about 1 mr at angles below  $1^{\circ}$  and about 0.5 mr at  $3^{\circ}$ . The 216 mc fluctuations are about half the 108 mc values.
7. An estimate of very rapid elevation angle fluctuations (periods of the order of milliseconds) indicates a maximum amplitude of 0.1 mr at 108 mc and 0.05 mr at 216 mc. This estimate is based on the observed max-min ratios of the interferometer patterns.
8. The second-to-second fluctuations in range error can be estimated from measured doppler fluctuations. These are usually small; of the order of  $\pm 3$  meters at 108 mc and 0.8 meters at 216 mc. Occasional deviations of ten times these values are found. Deviations greater than 12 meters at 216 mc are rare.
9. Precursor signals have been received on 70% of the passes where they would have been detected. These signals were received when the satellite was as much as 1800 miles beyond the horizon. No well defined frequency dependence is observed on the occurrence or intensity of the signals. Passes where no precursors were found, were generally those requiring a northwesterly look angle, or

those occurring early in morning. The propagation mechanism producing precursor signals is very efficient; signals of nearly free space intensity were observed out to distances of 1200 miles beyond the radio horizon. Correlation with radiosonde data indicates that the mechanism responsible for propagating precursor signals is the topospheric duct formed by the elevated inversion layer which was present during the passes when strong signals were observed.

## XI. RECOMMENDATIONS

As a result of the information obtained to date the following recommendations are made:

1. Obtain oblique incidence ionosphere sounding data which are simultaneous with, and from the same area as F layer penetration of the ray paths for each measured pass. The station at Stanford would be best suited for the Pt. Buchon measurements.
2. Obtain on-site radiosonde data simultaneous with each pass, for computation of the tropospheric refraction components.
3. Further emphasis should be placed on using the doppler fluctuation approach for obtaining finer grained information on ionospheric inhomogeneities.
4. Further investigation of precursor signals should be performed, particularly during weak duct and standard tropospheric conditions to verify whether or not tropospheric ducting is the only cause of such signals.
5. Further measurements of elevation angle errors should be made during weak duct and standard conditions, so the conclusions presented above may be extended to a wider area of applicability. Winter and springtime measurements at Pt. Buchon would provide such information. Coverage of a wide variety of conditions would enable extrapolation of position accuracy limitations to any area of operational interest.
6. Simultaneous refraction measurements should be made using radio stars and radio satellites. This would indicate the utility of

radio star monitoring as a means of determining day-to-day refractive corrections on an operational basis. Such measurements should be made over an annual cycle to provide the full diurnal range of ionospheric conditions at the time of setting of the star.

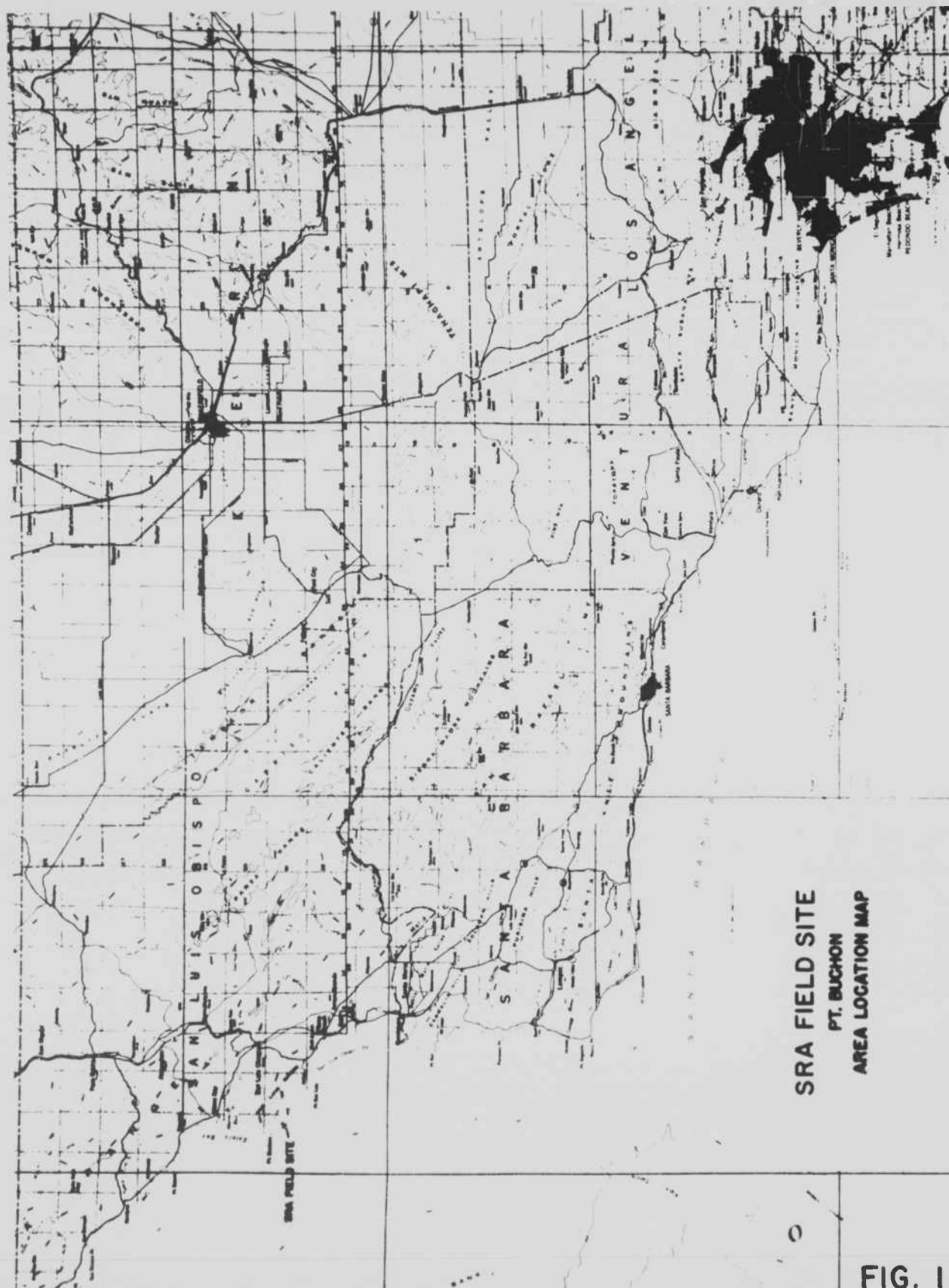
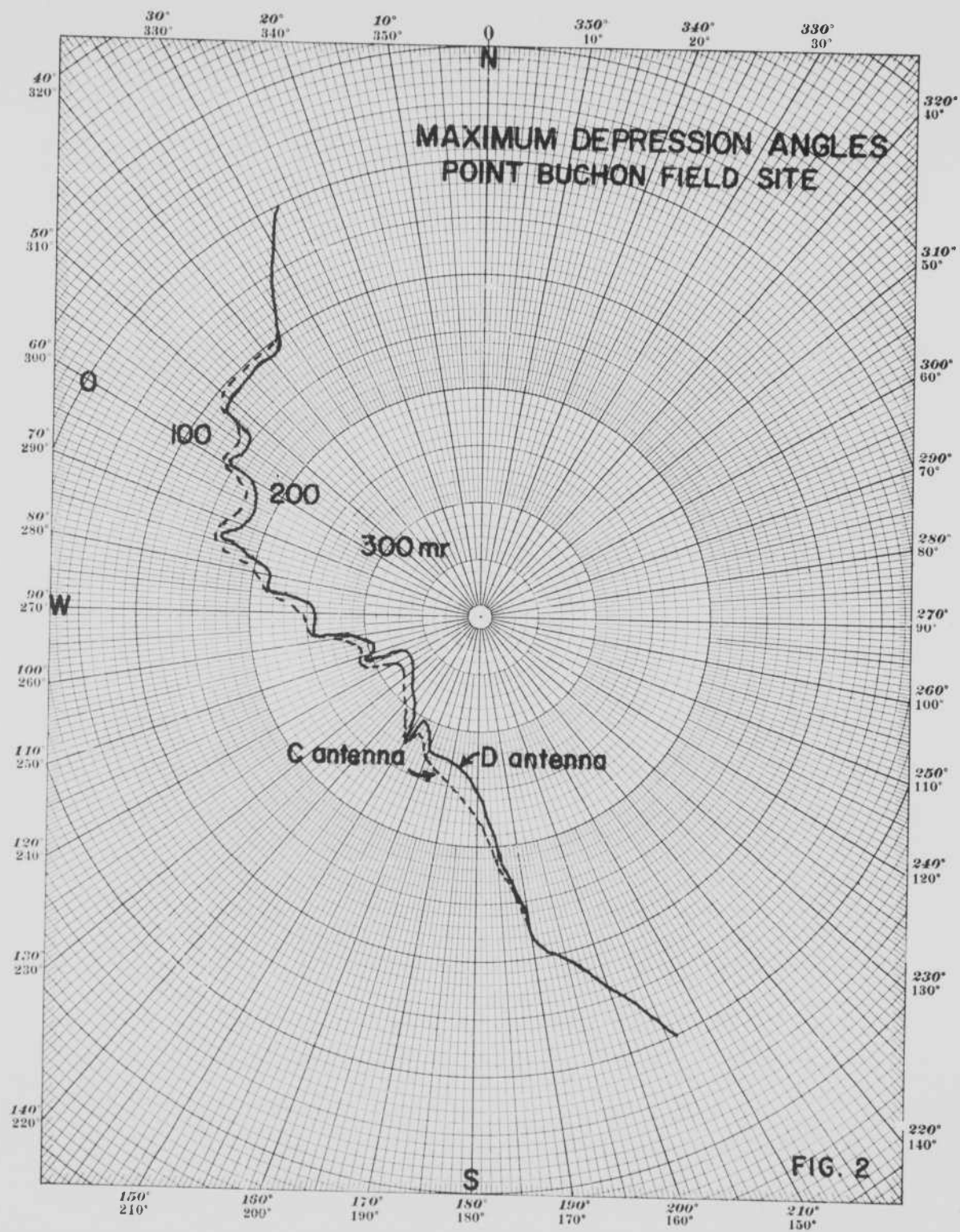
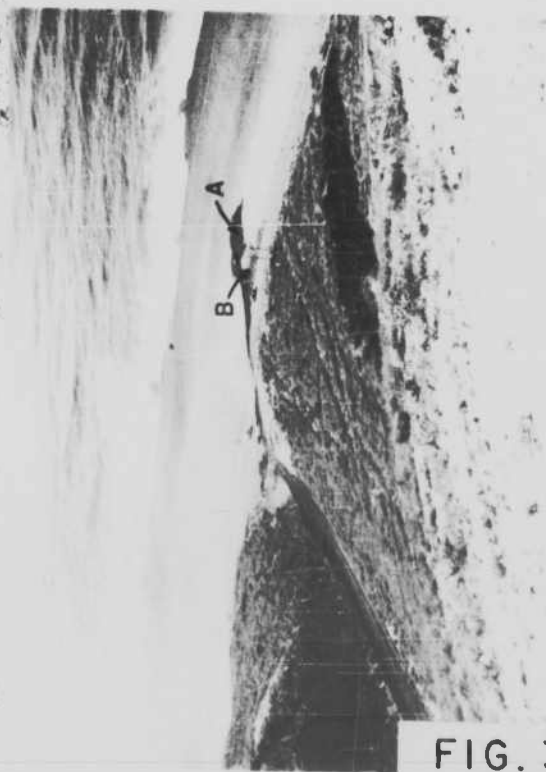
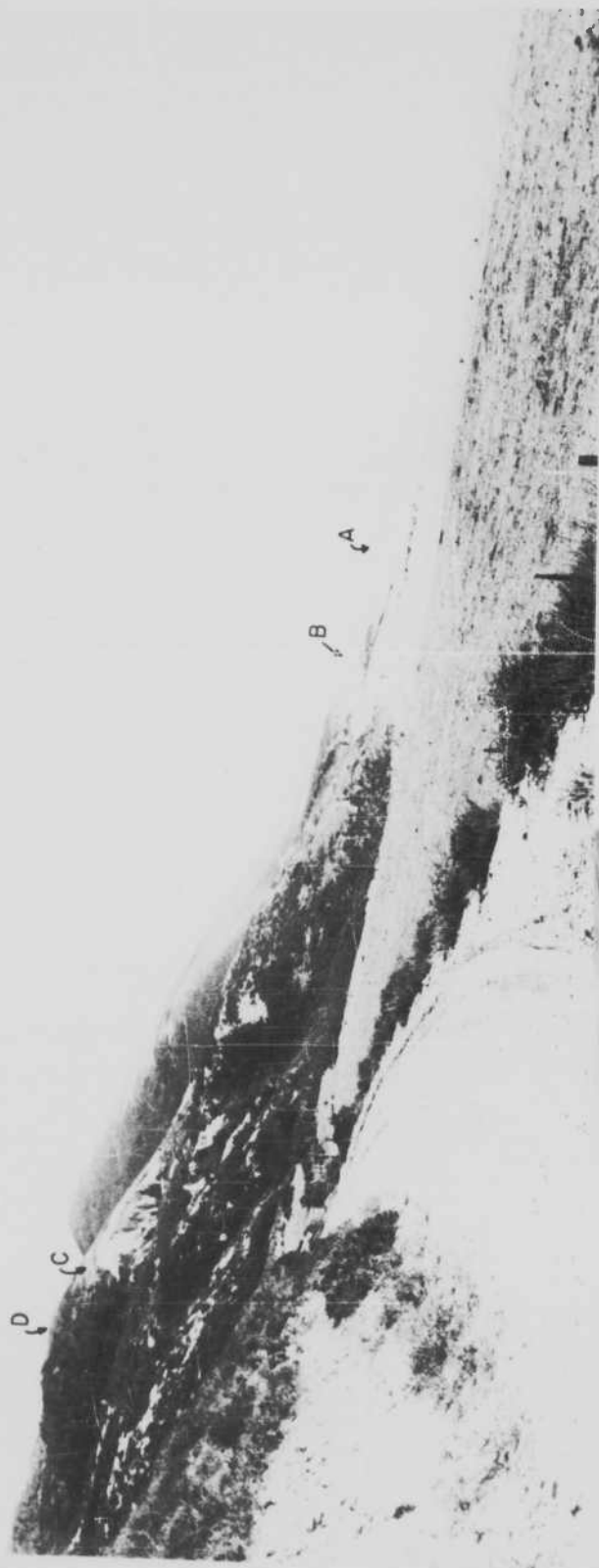


FIG. 1

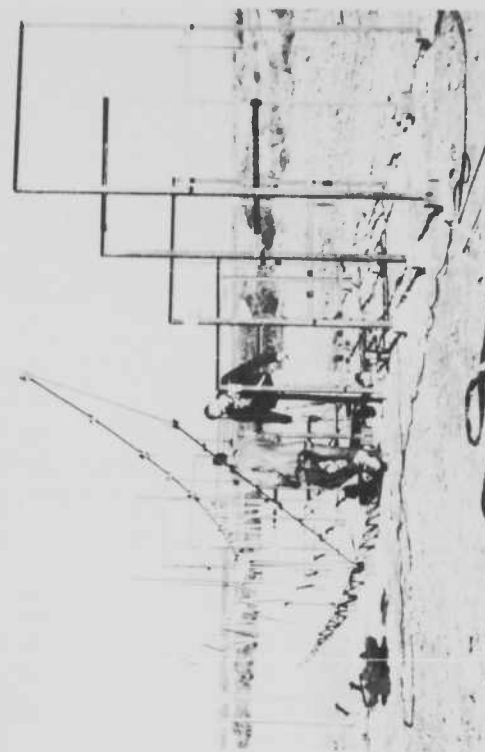




OVERALL TERRAIN PROFILE SHOWING ANTENNA LOCATIONS



LOCATIONS A AND B FROM D



JIG FOR ANTENNA CONSTRUCTION

FIG. 3

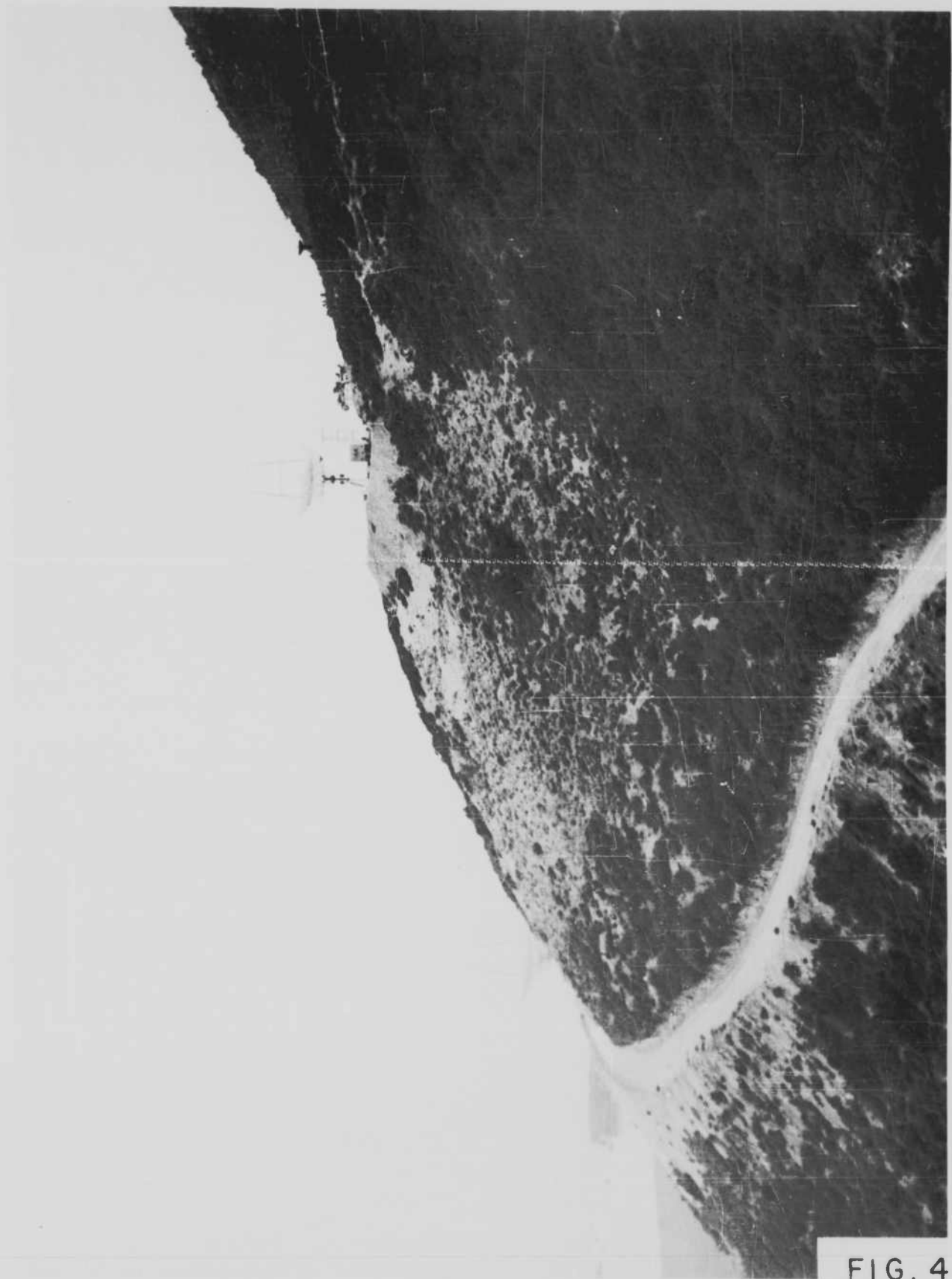


FIG. 4

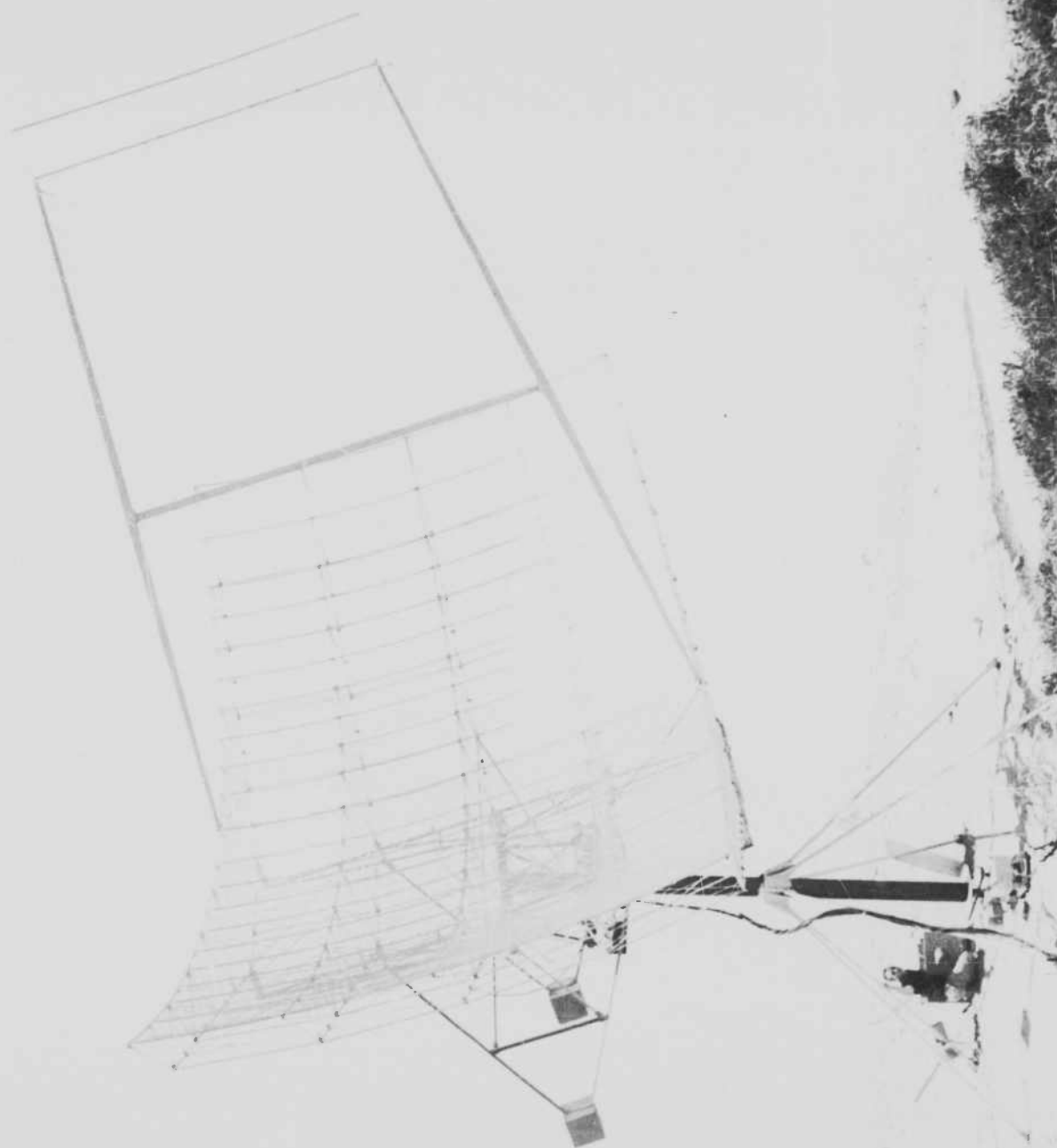


FIG. 5

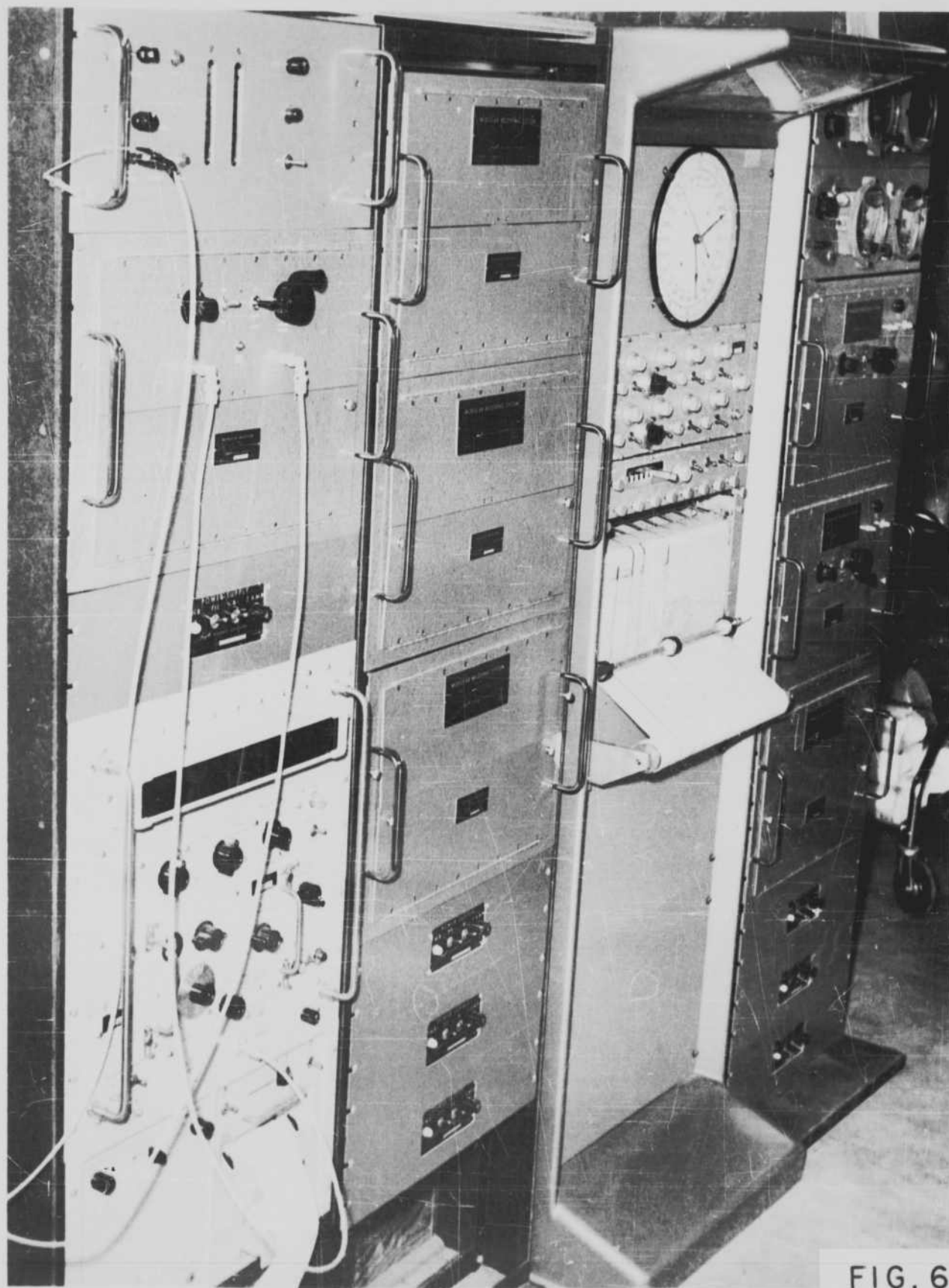
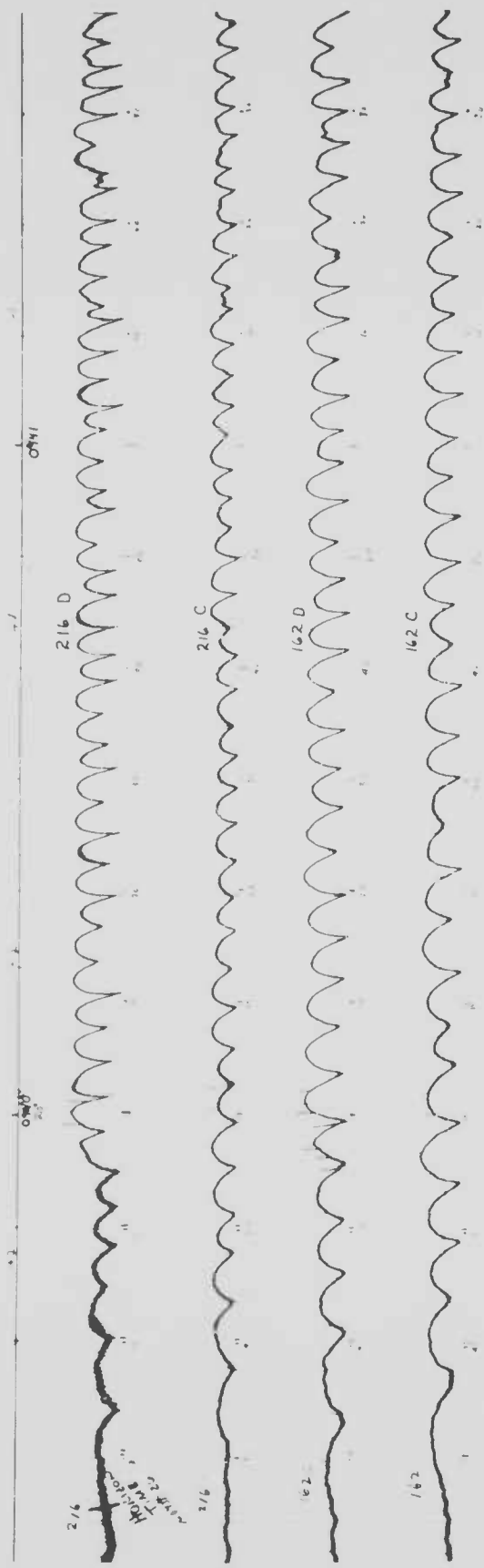


FIG. 6



PASS 16 TRANSIT 2A  
7-18-60

Doppler



FIG. 7

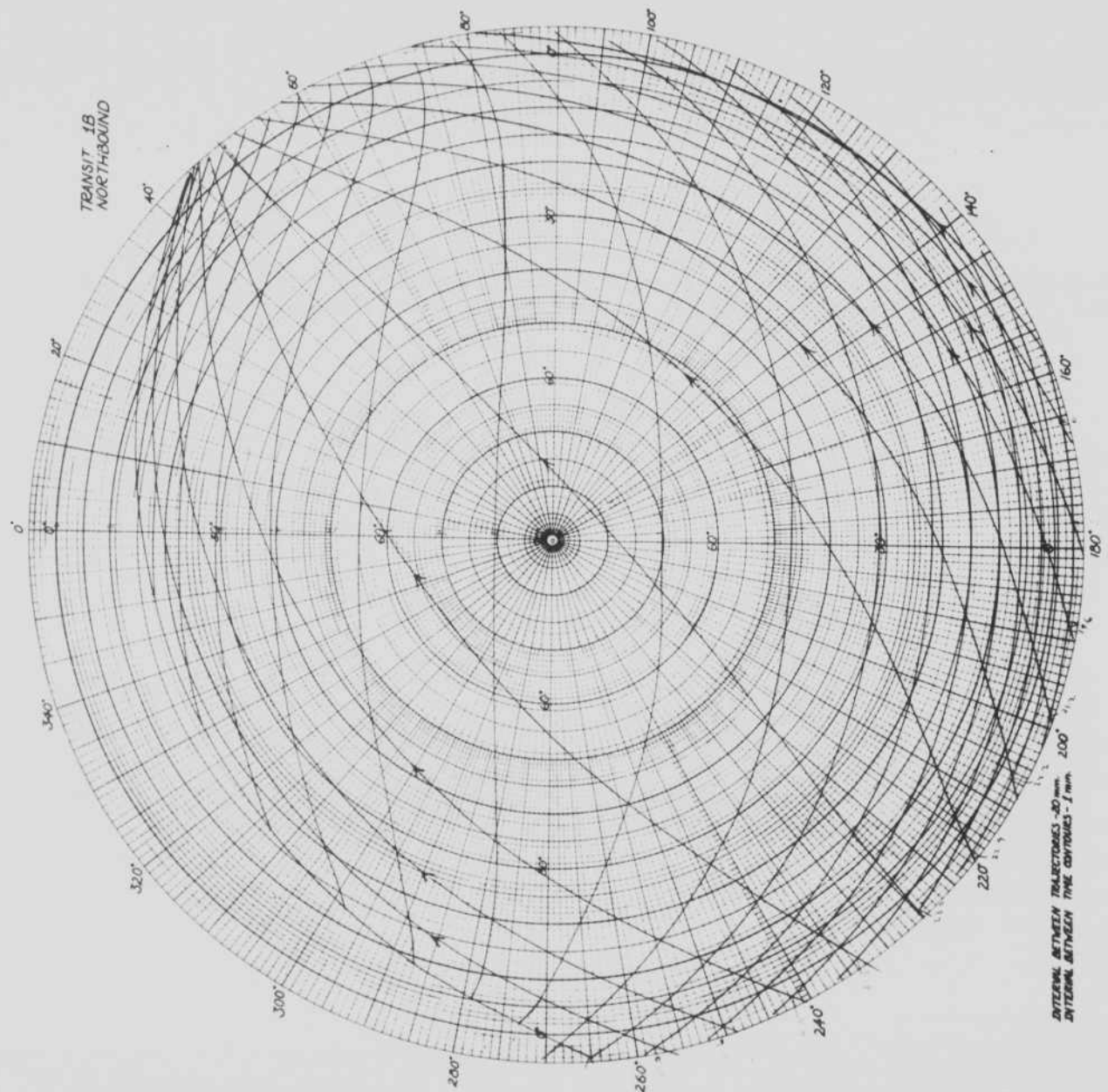


FIG. 8

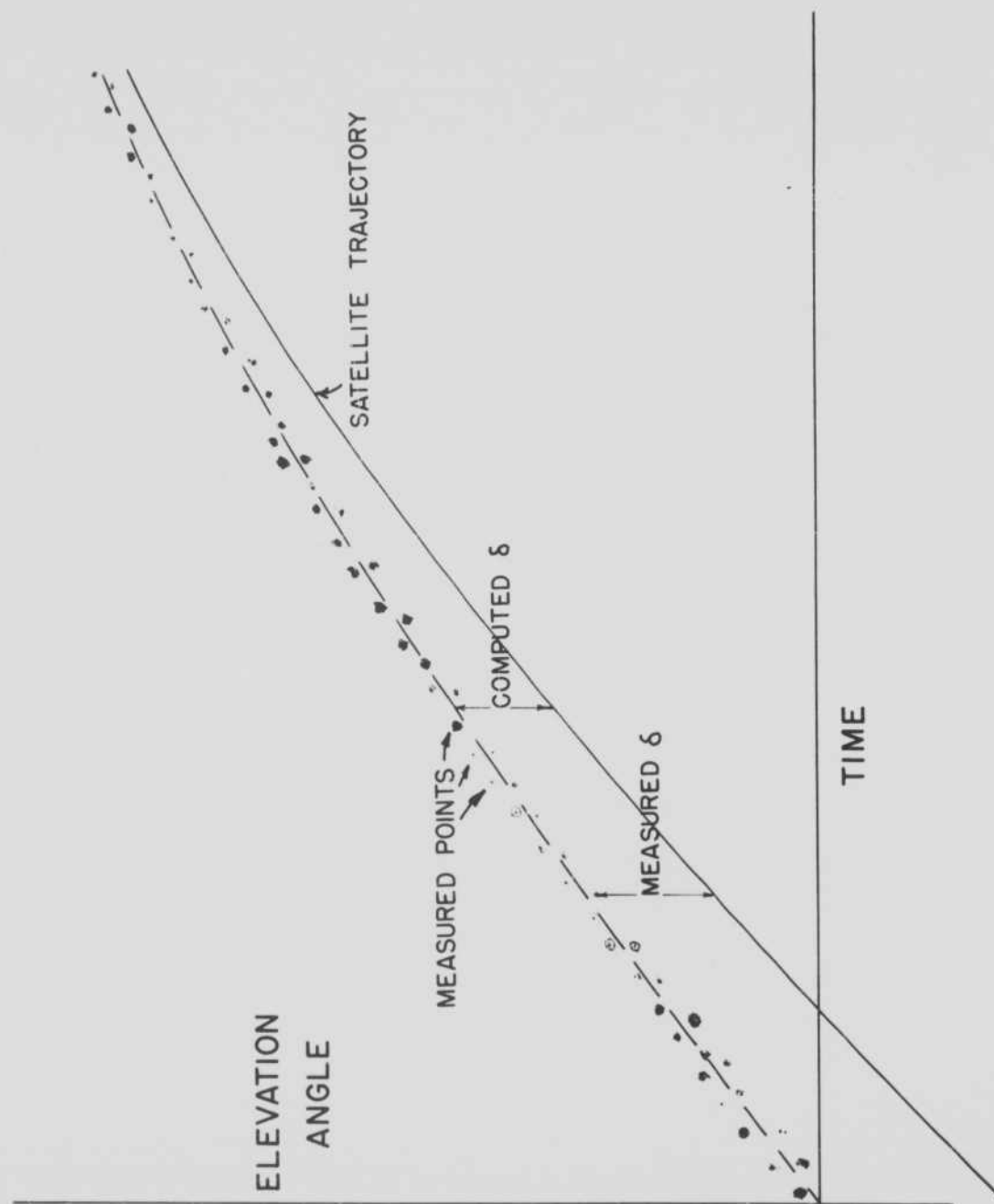
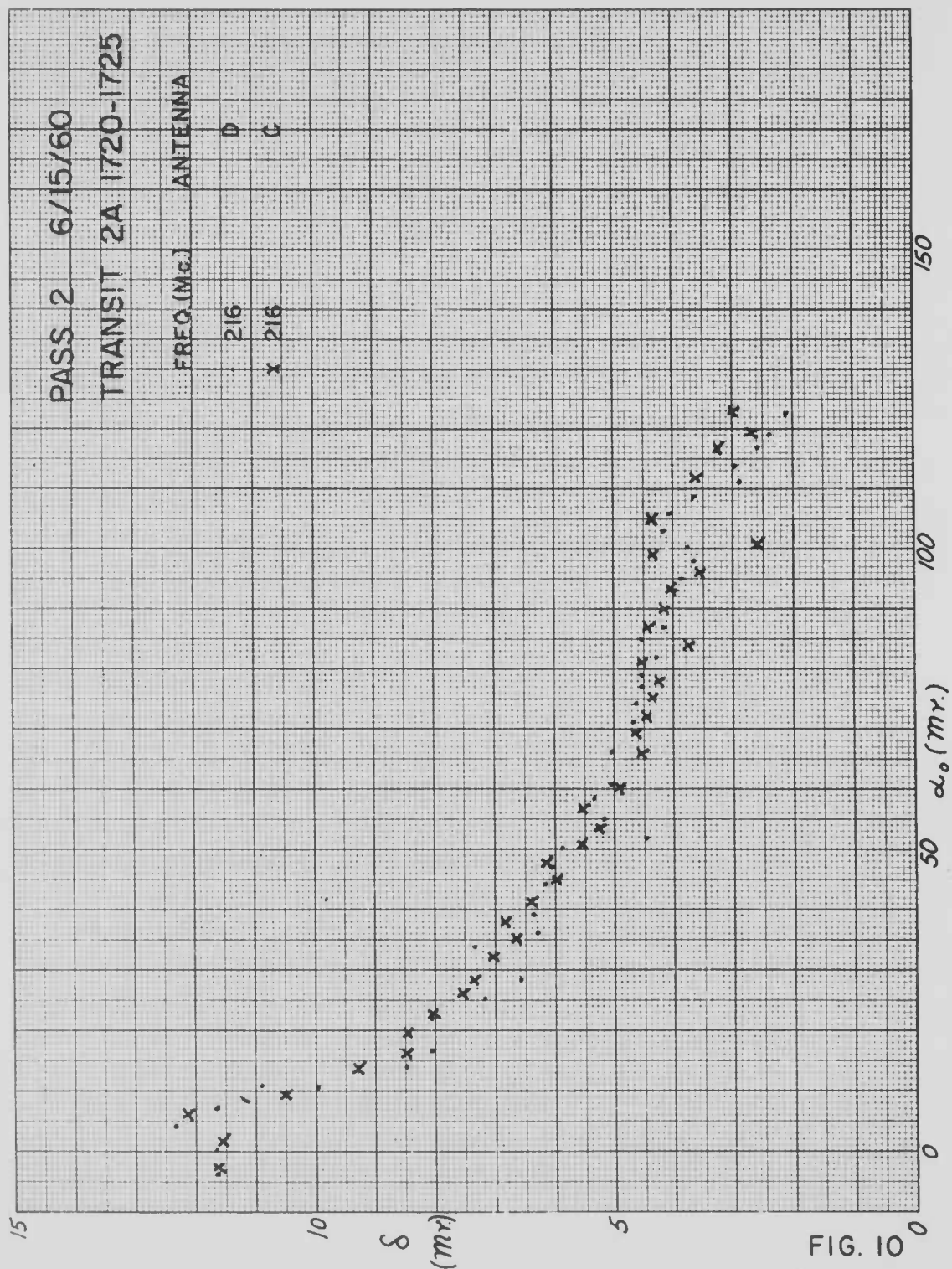


FIG. 9







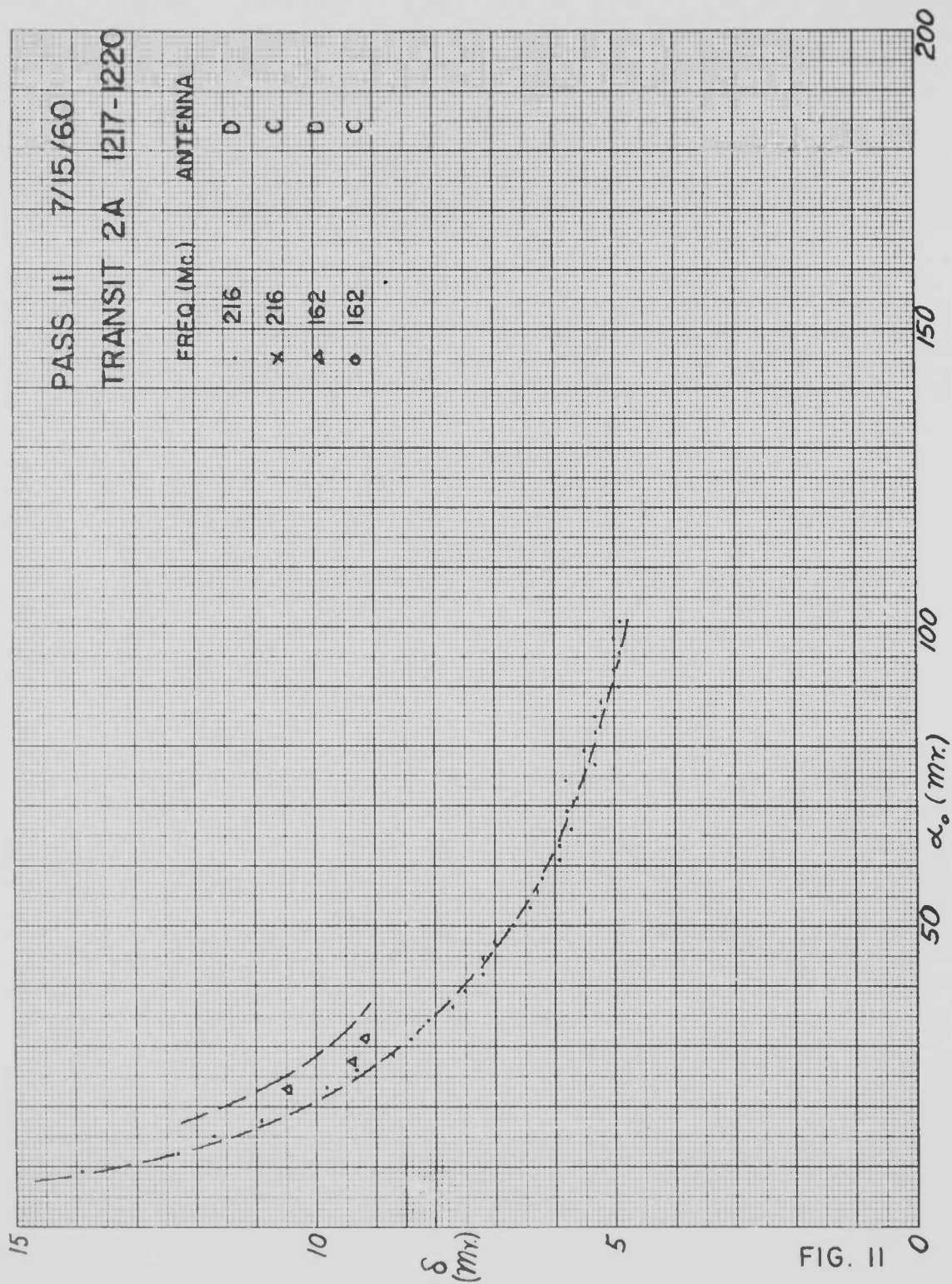


FIG. II

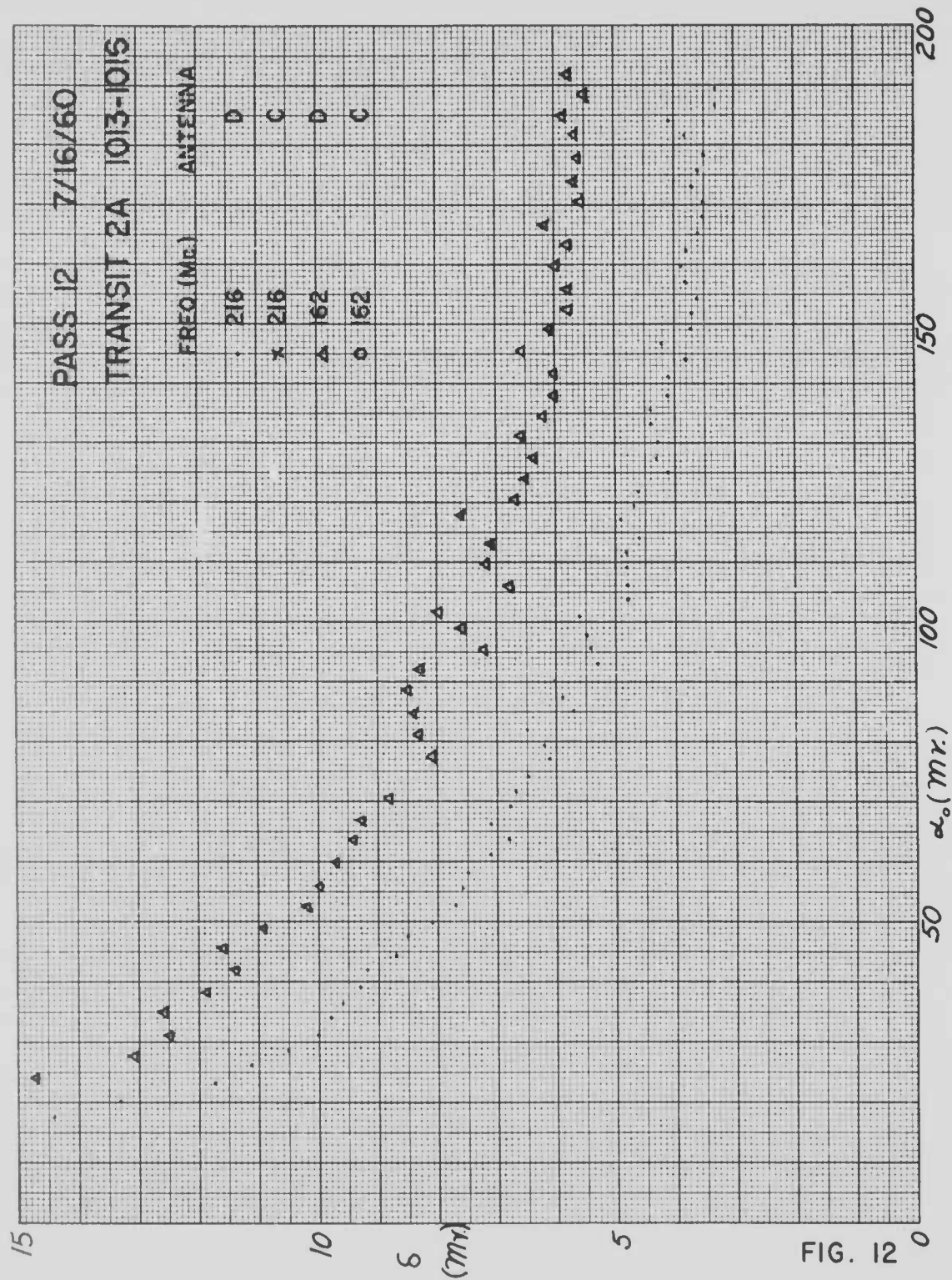
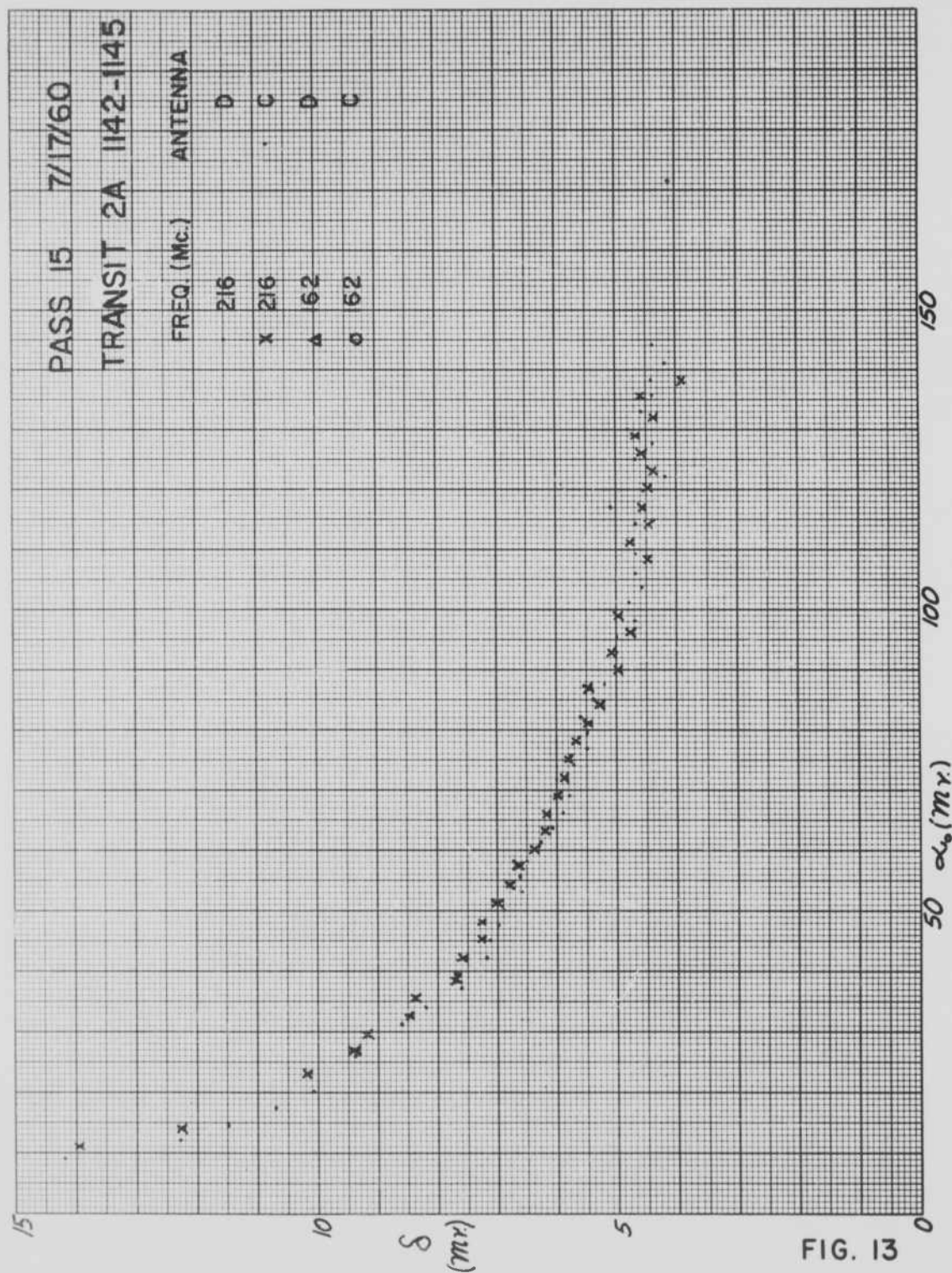
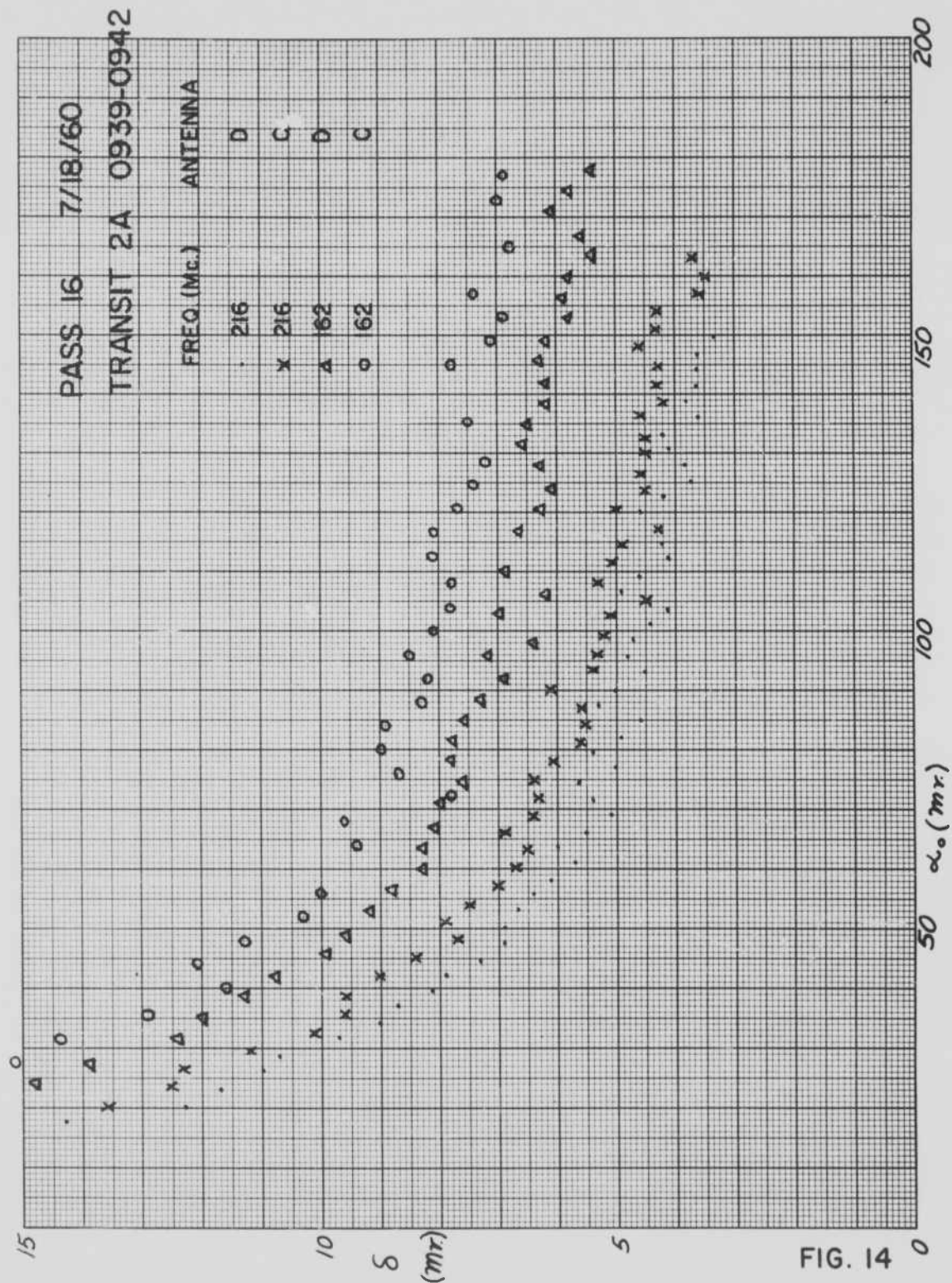


FIG. 12







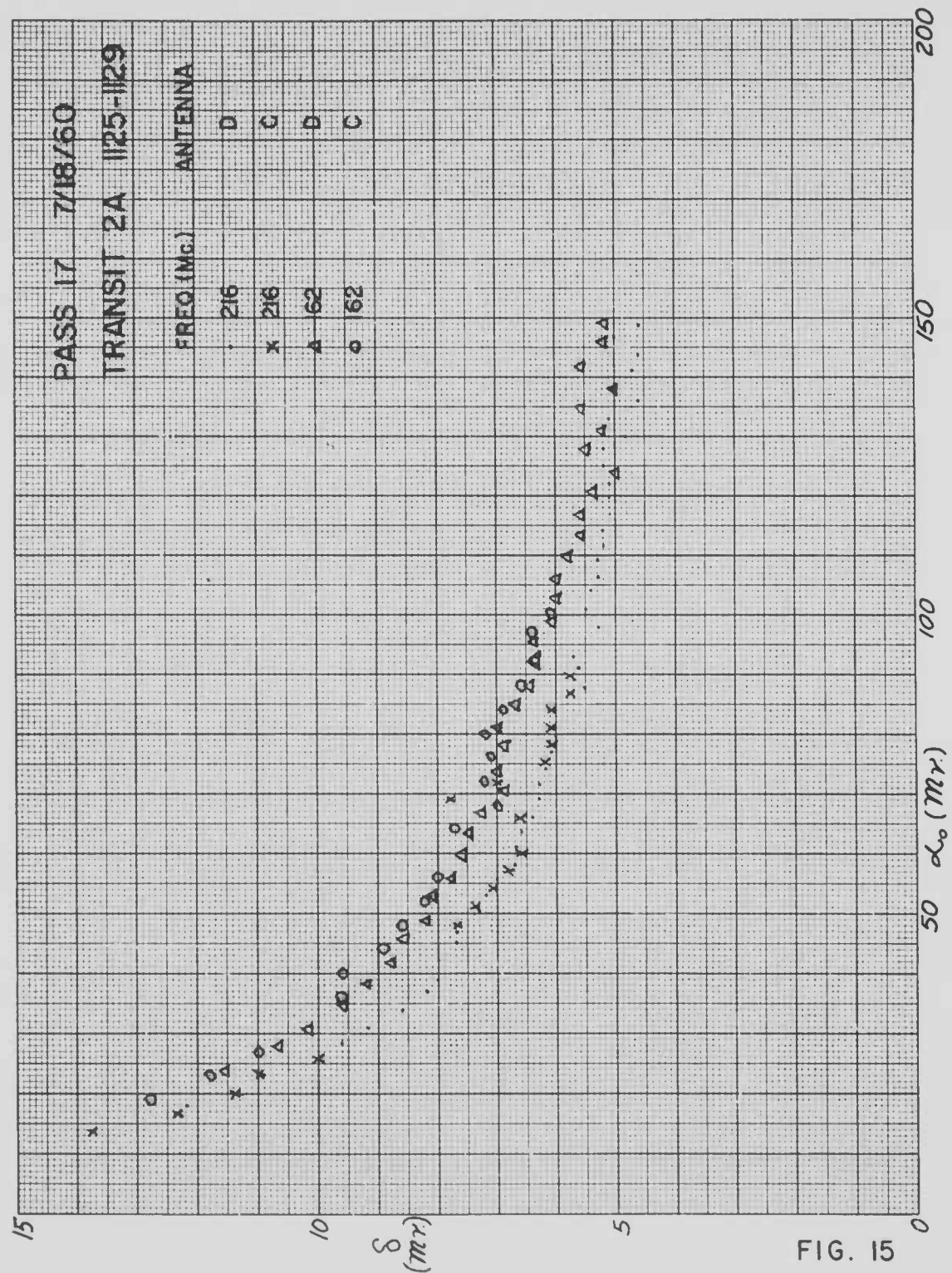
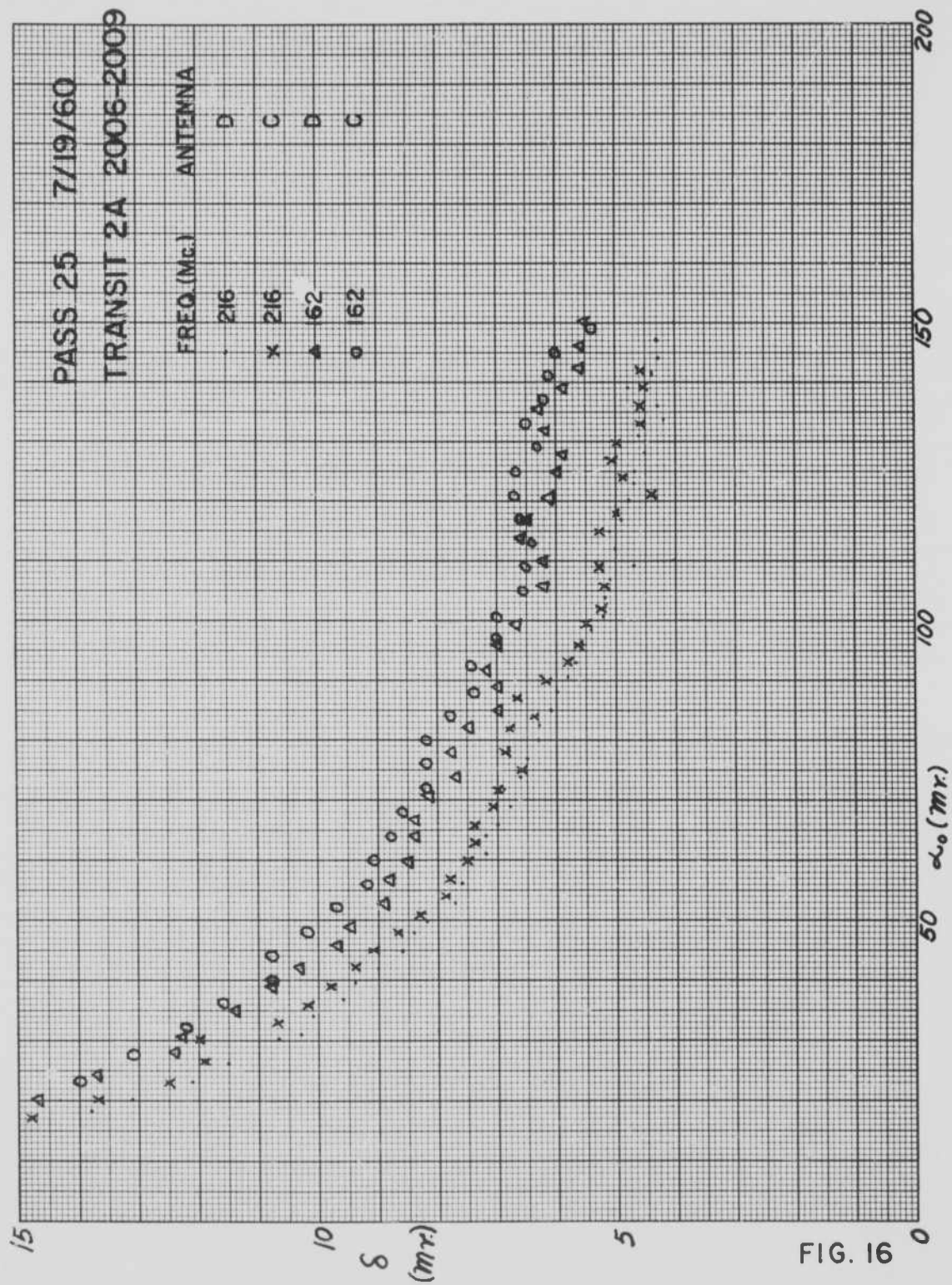


FIG. 15



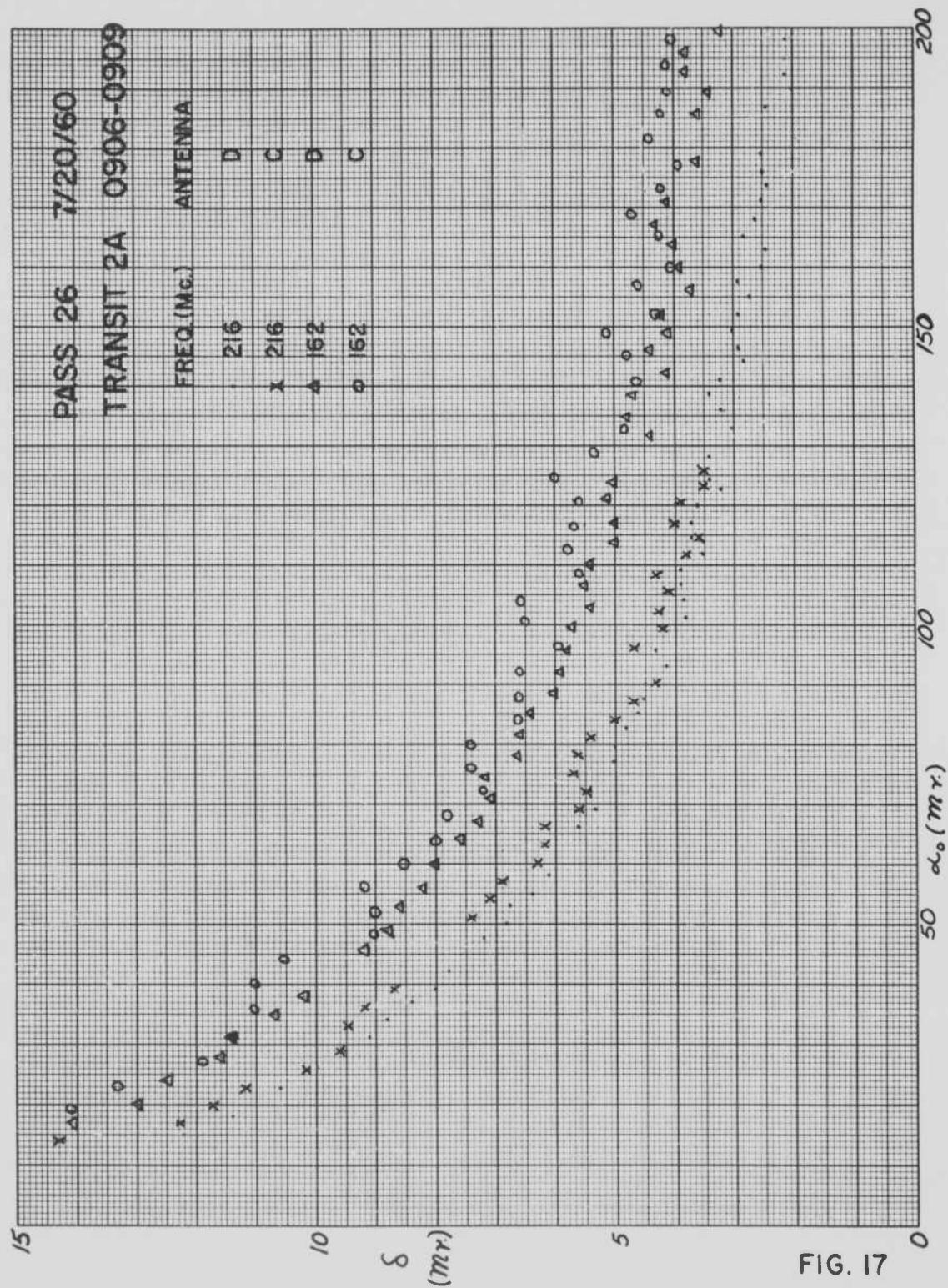
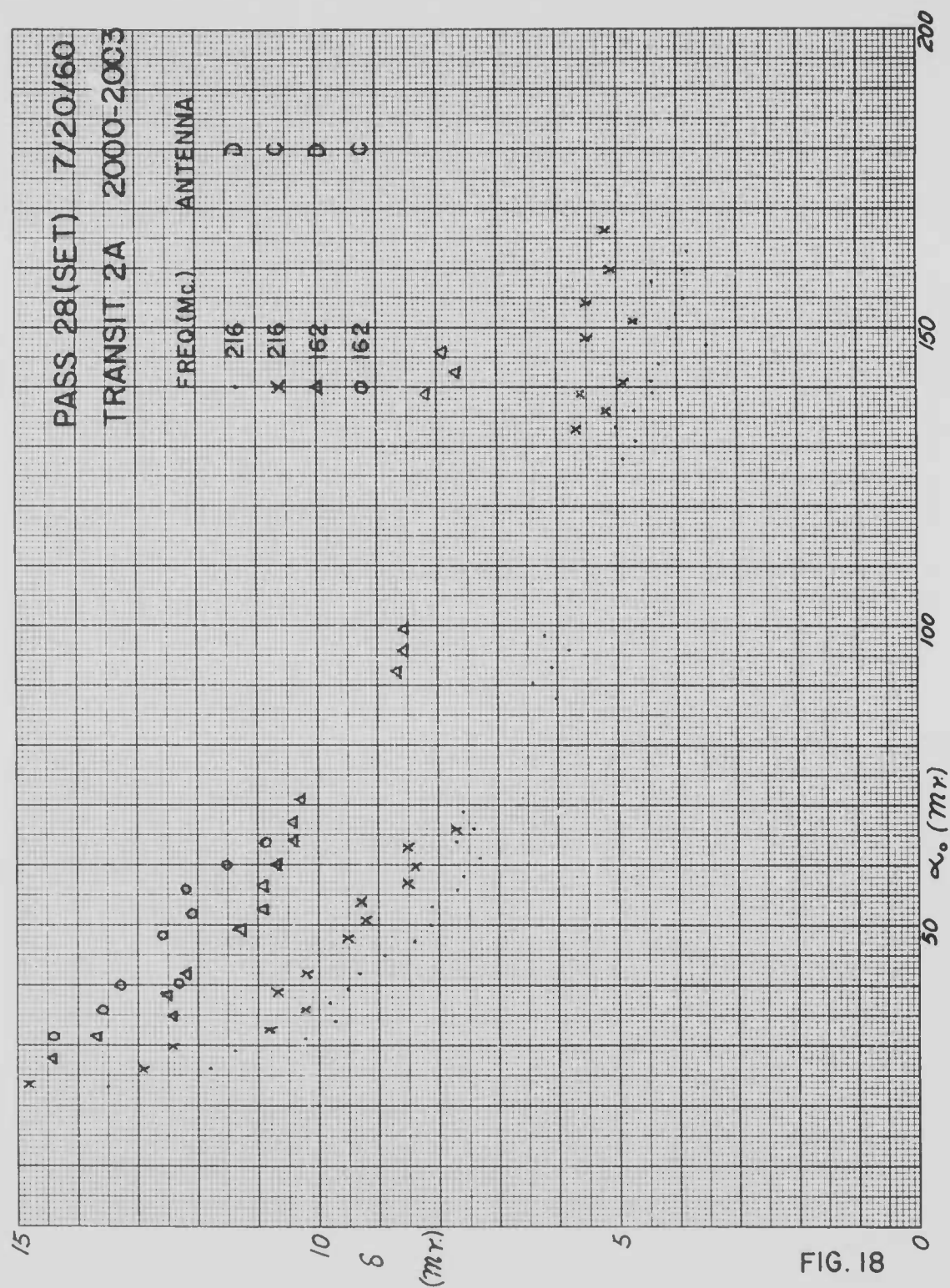


FIG. 17





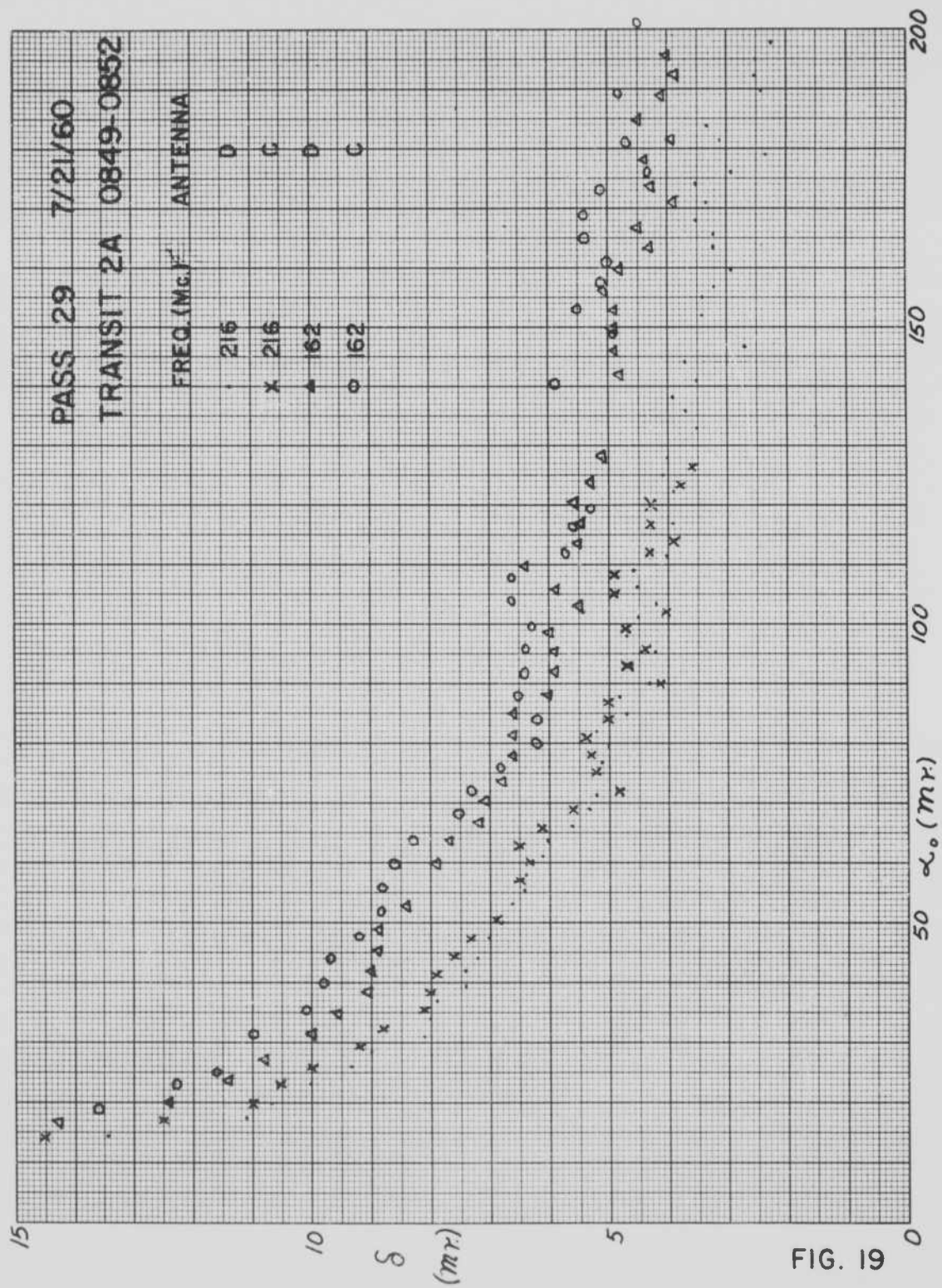


FIG. 19

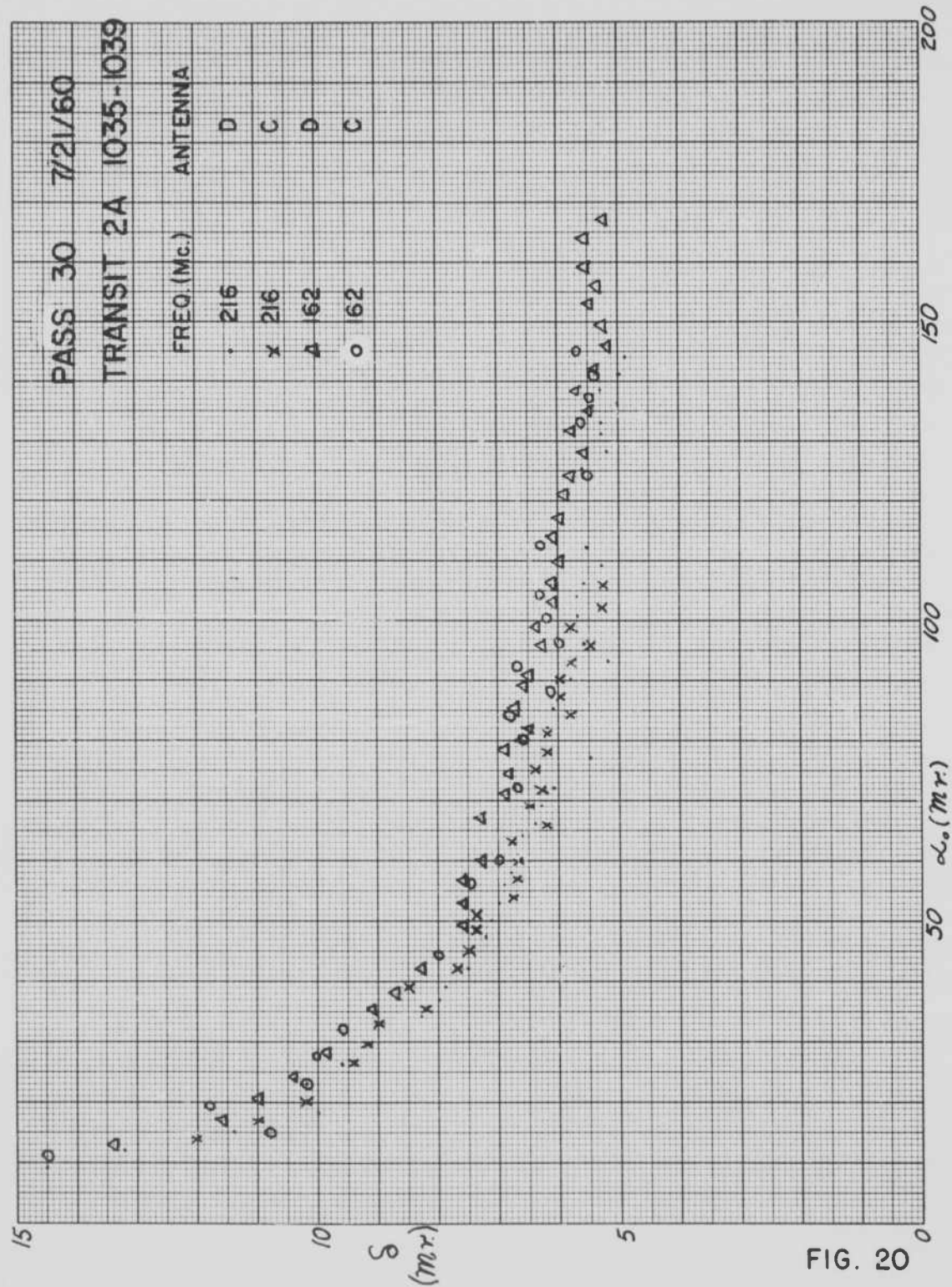


FIG. 20

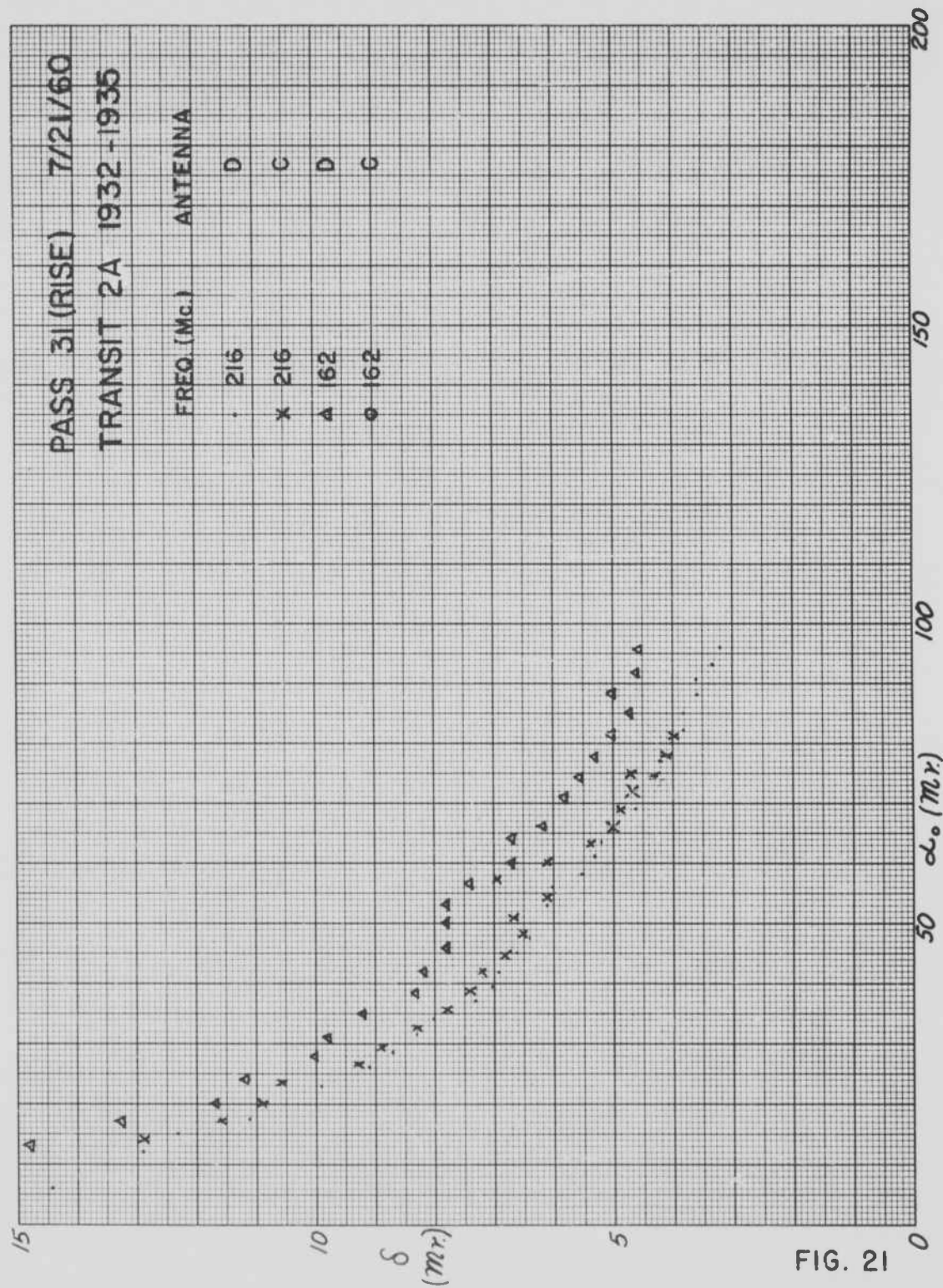
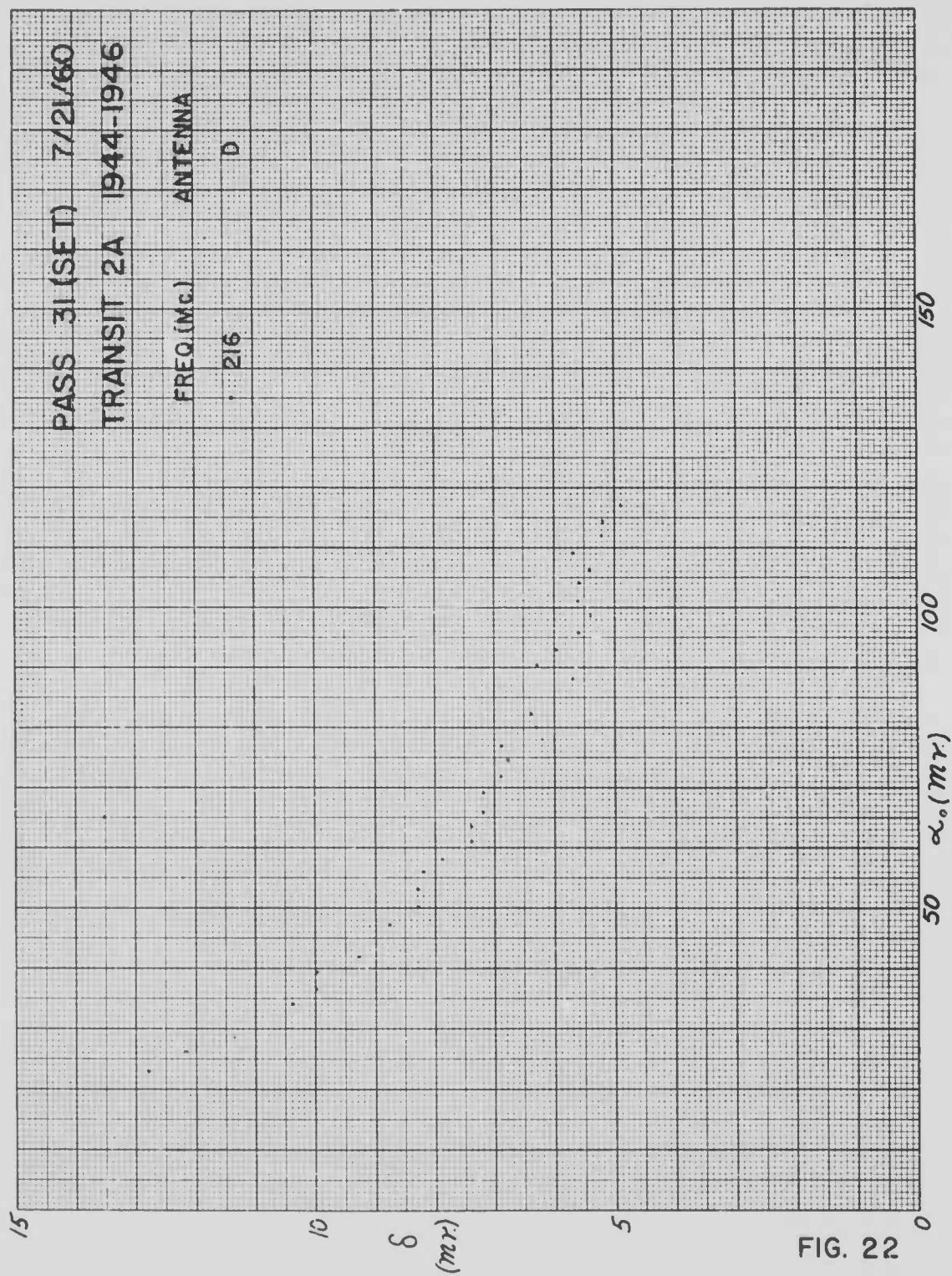
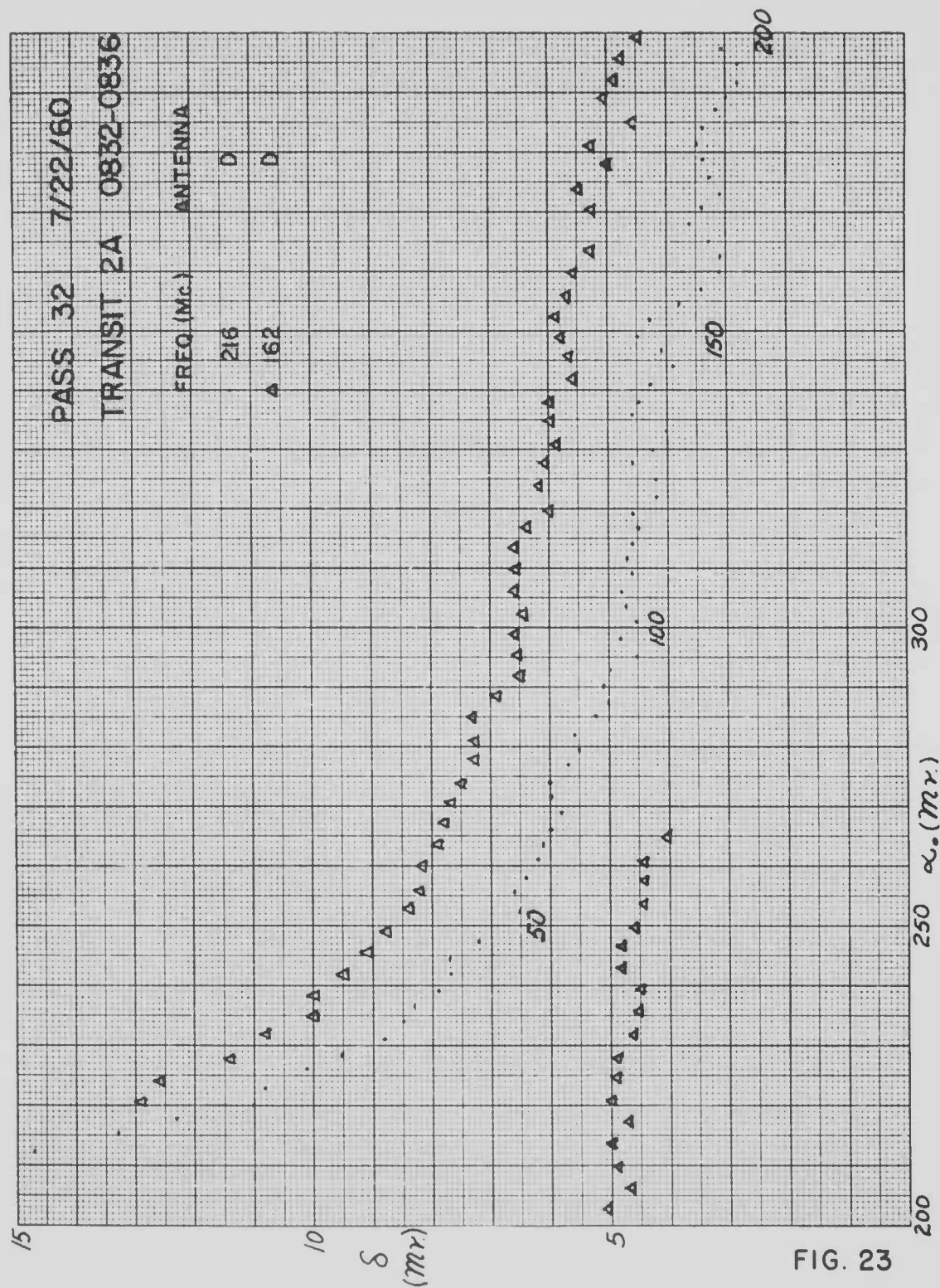
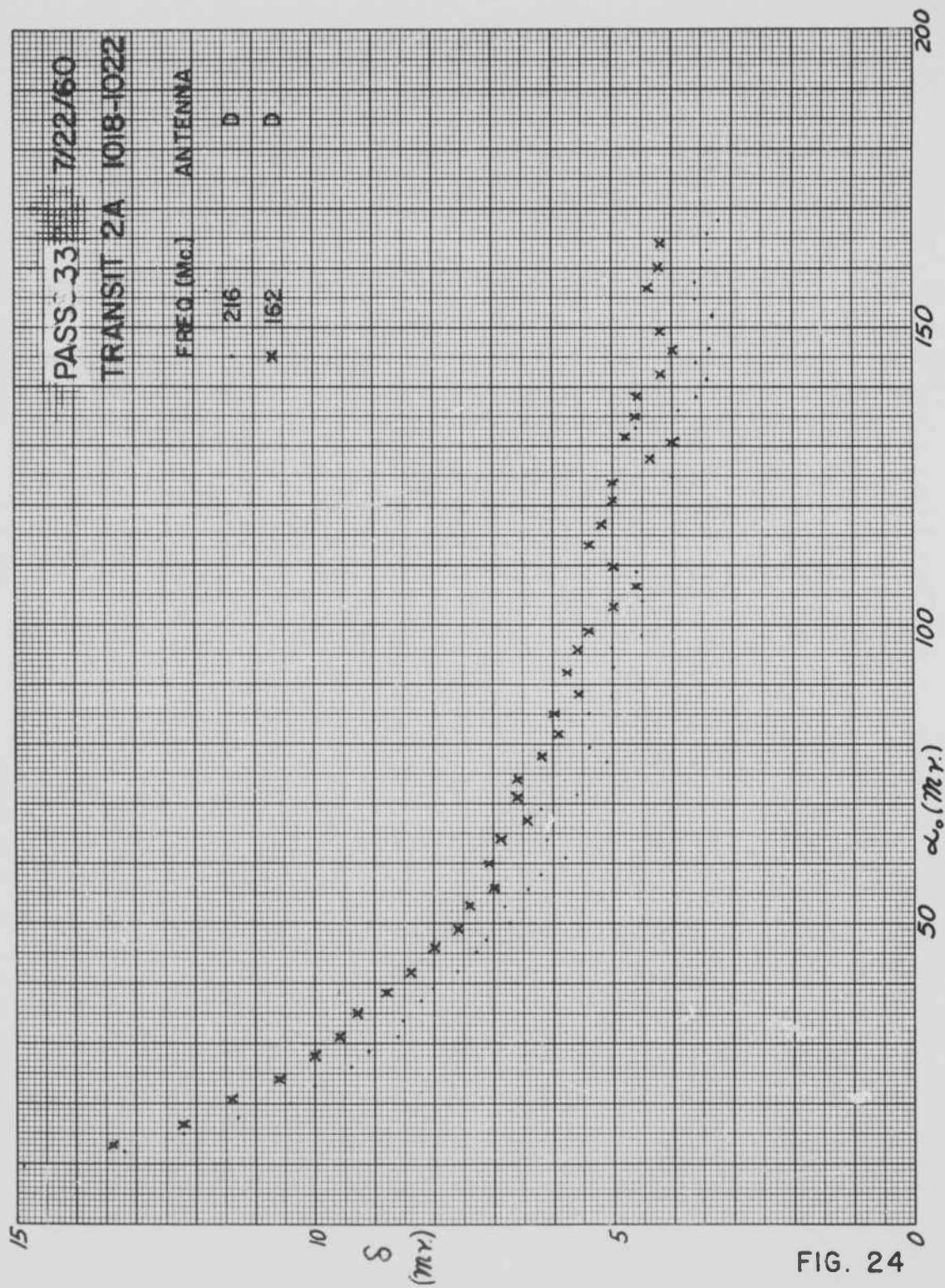


FIG. 21









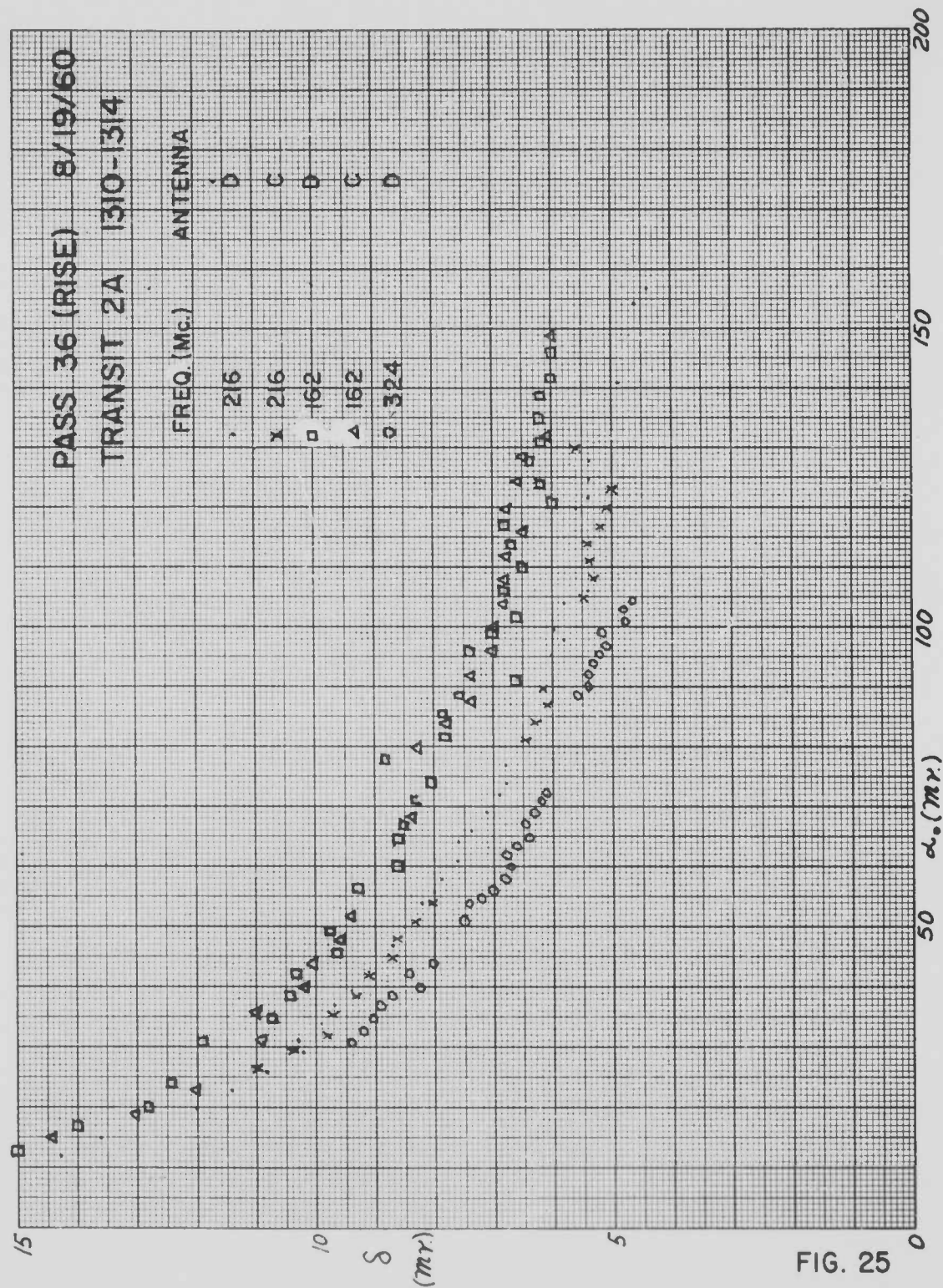


FIG. 25

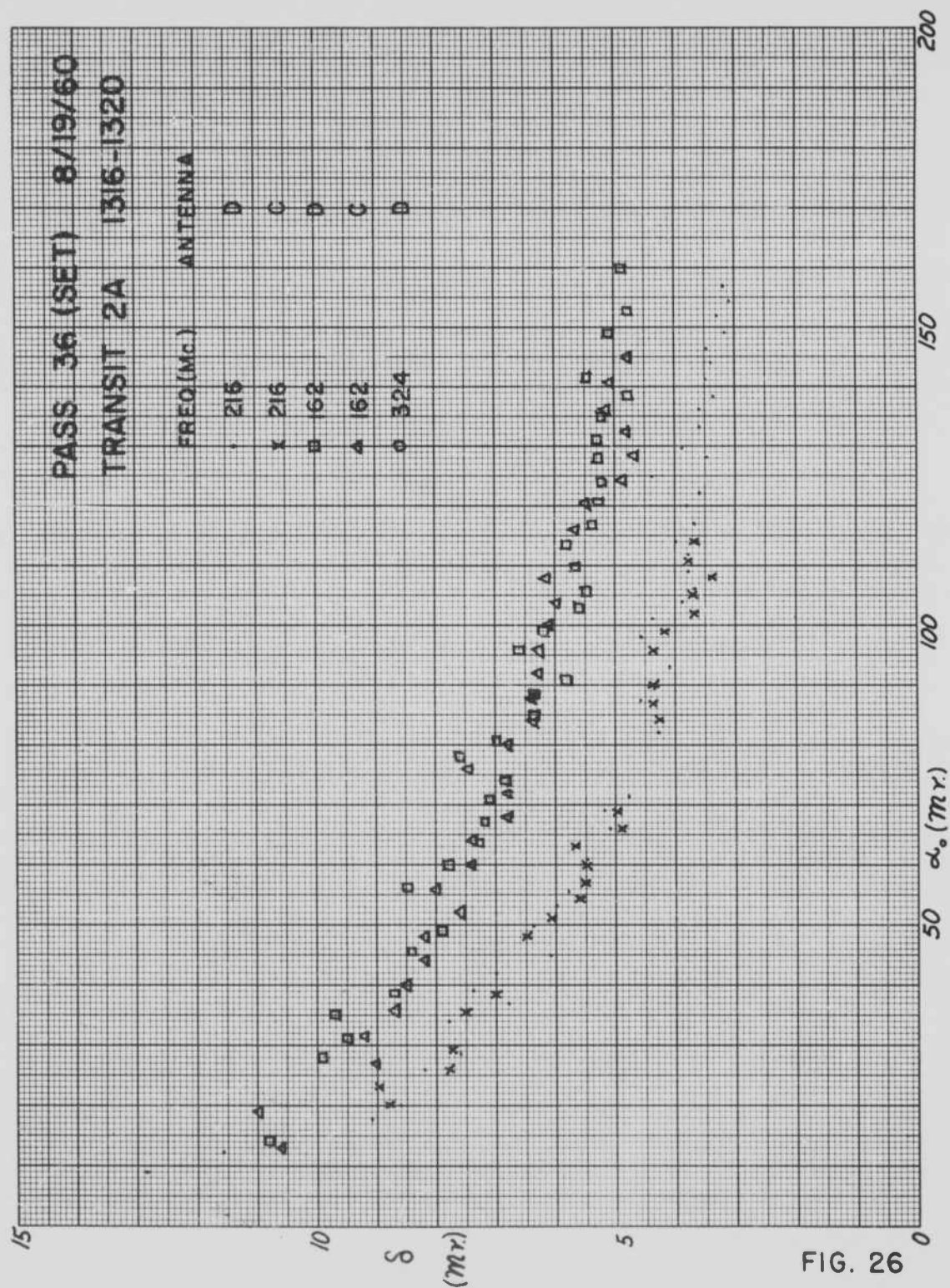
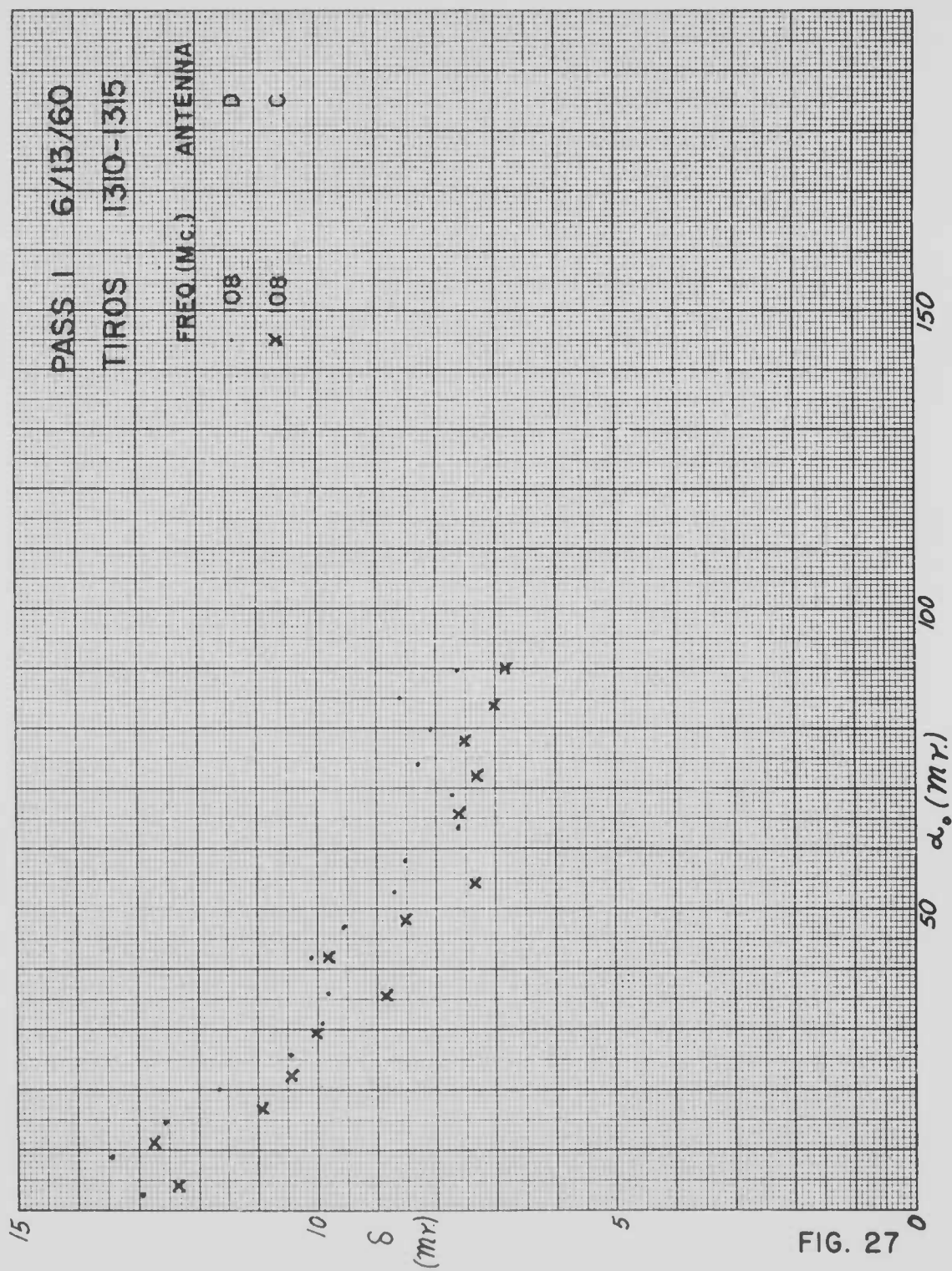


FIG. 26





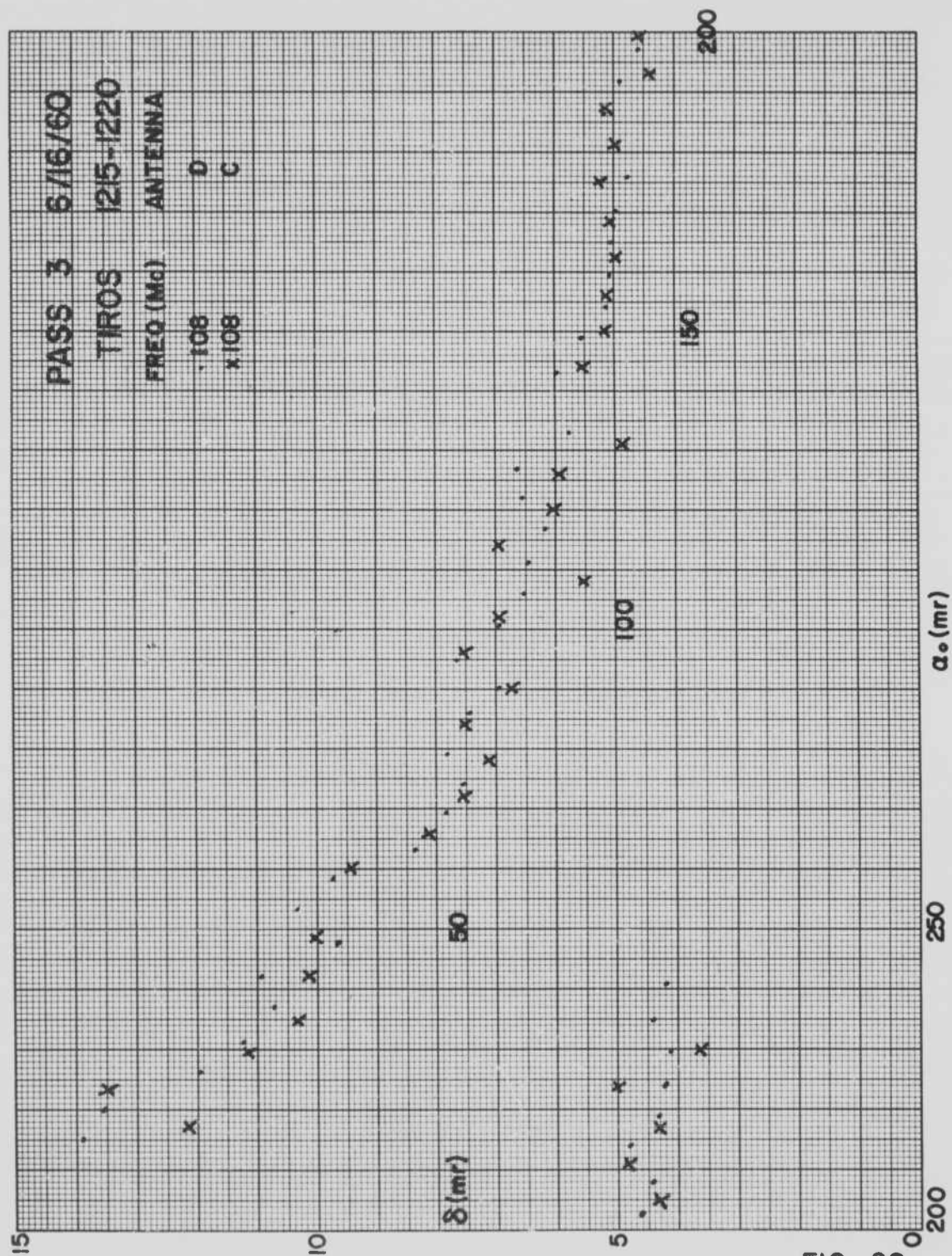
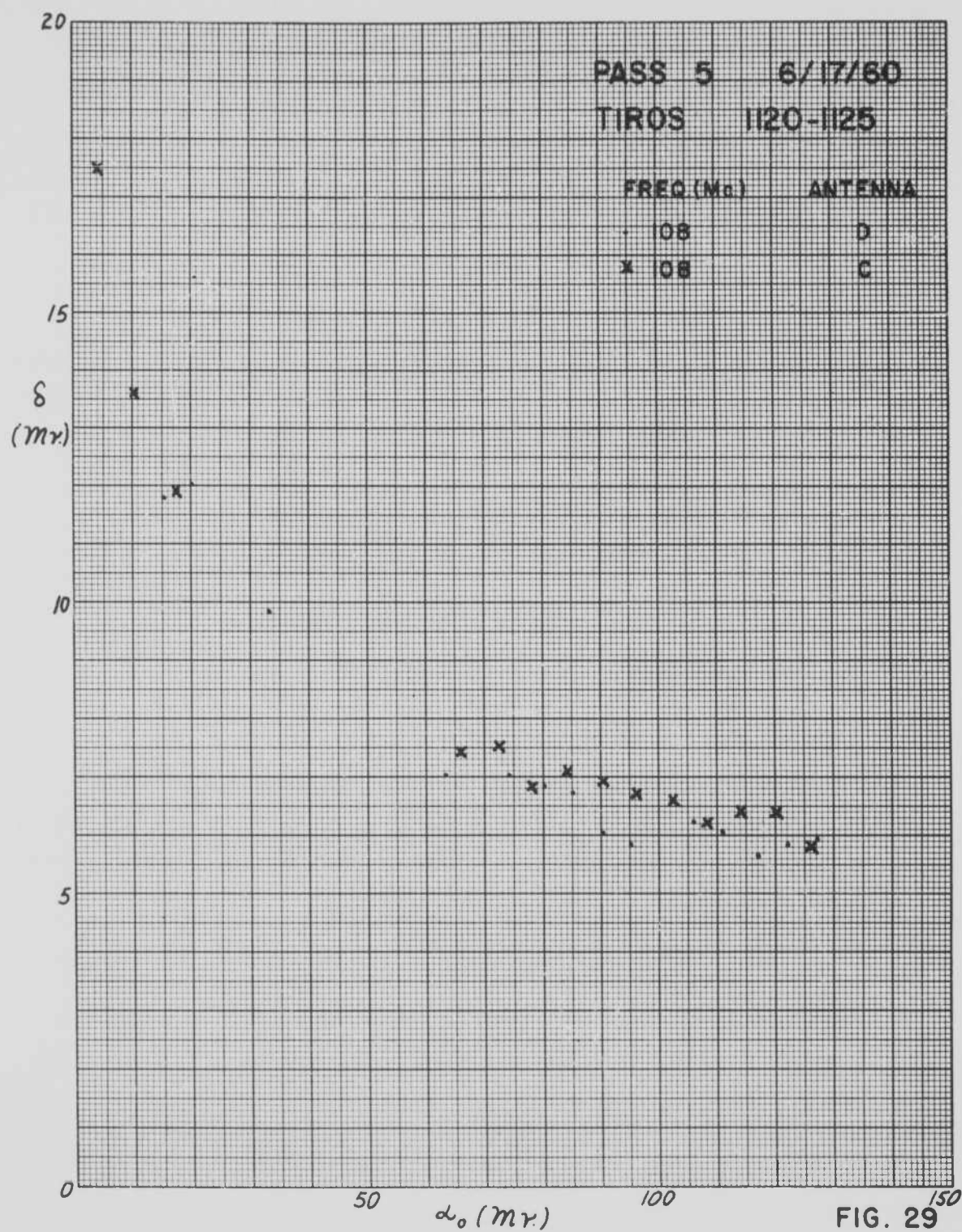
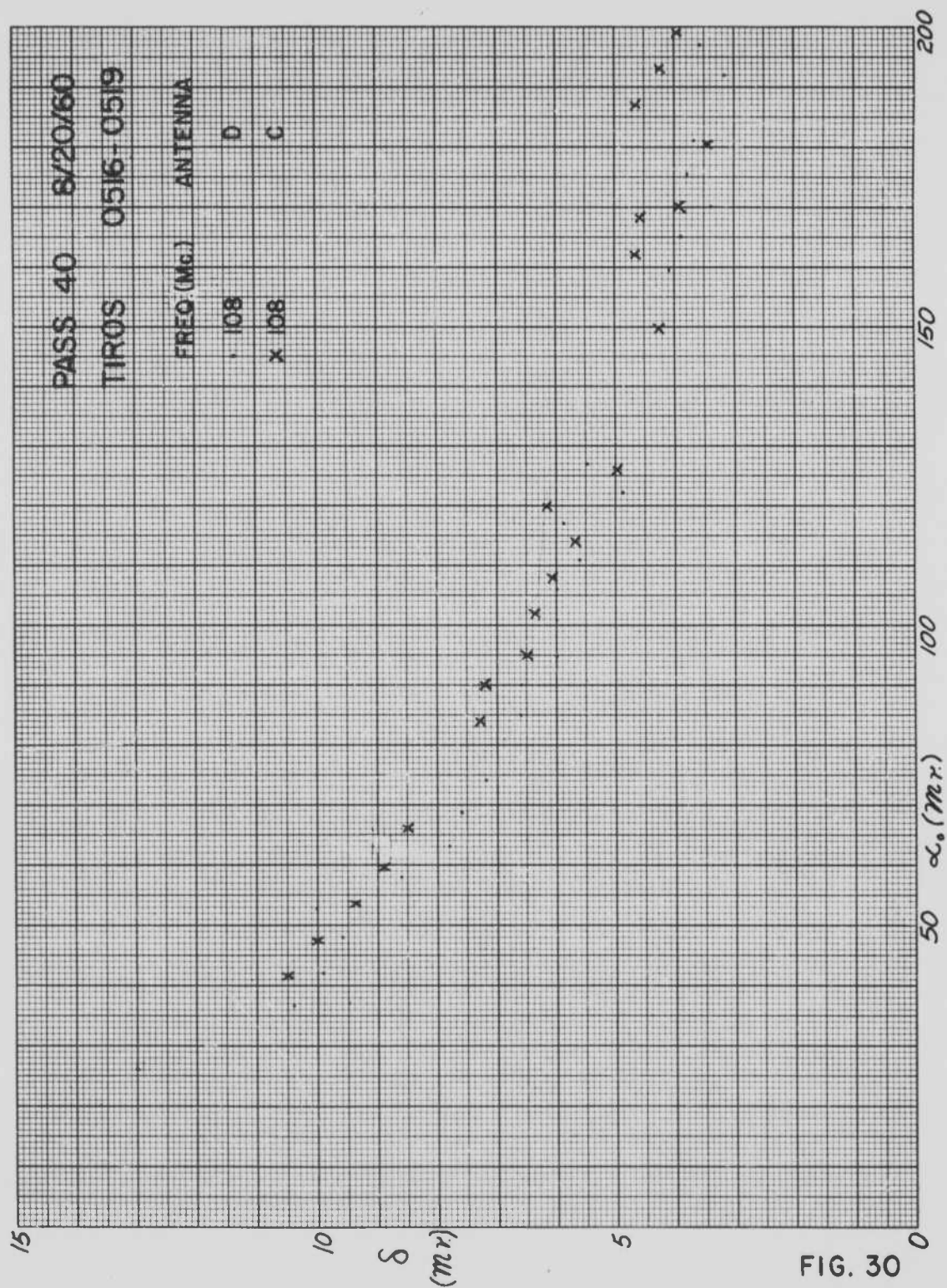


FIG. 28







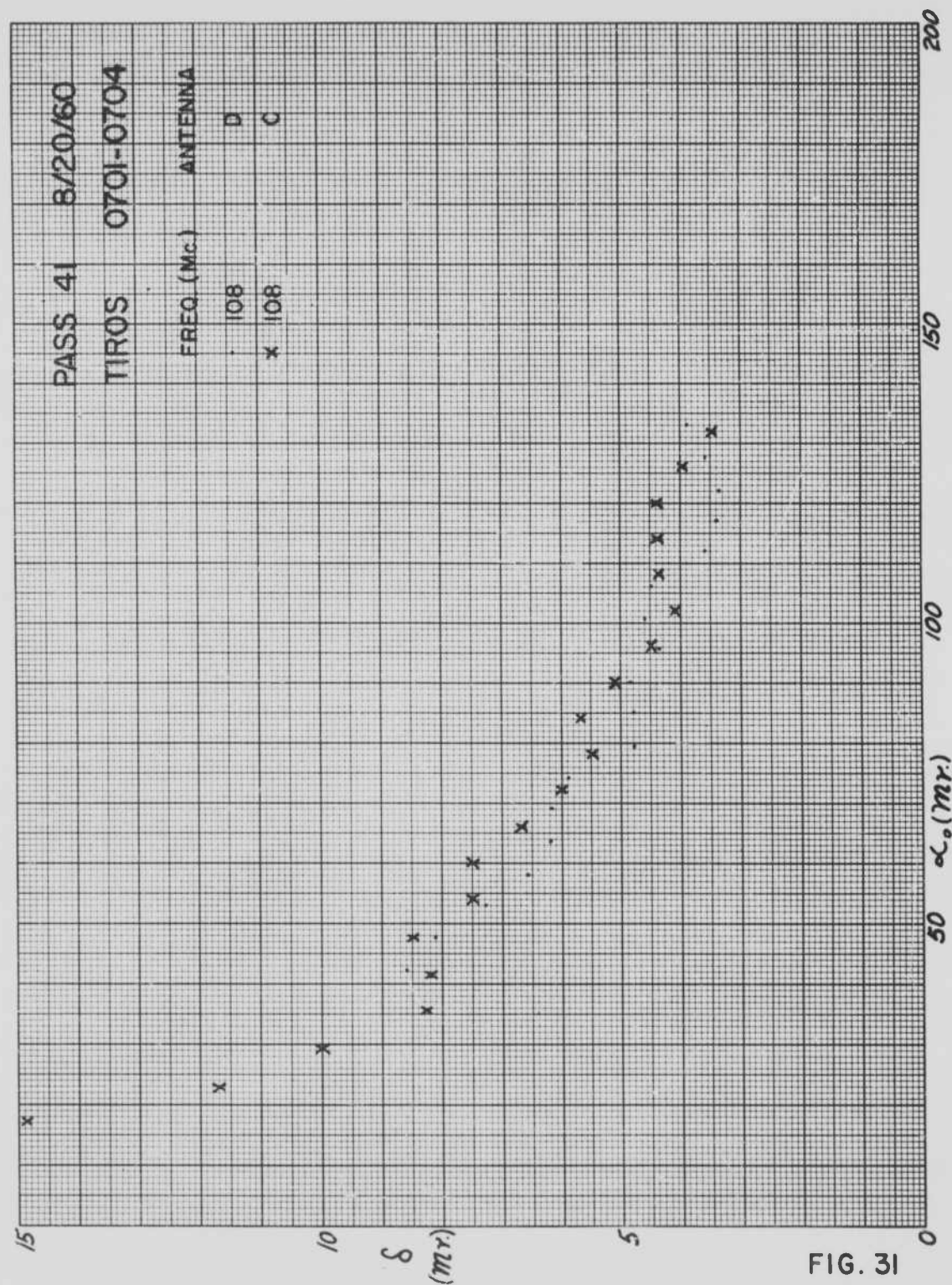


FIG. 31

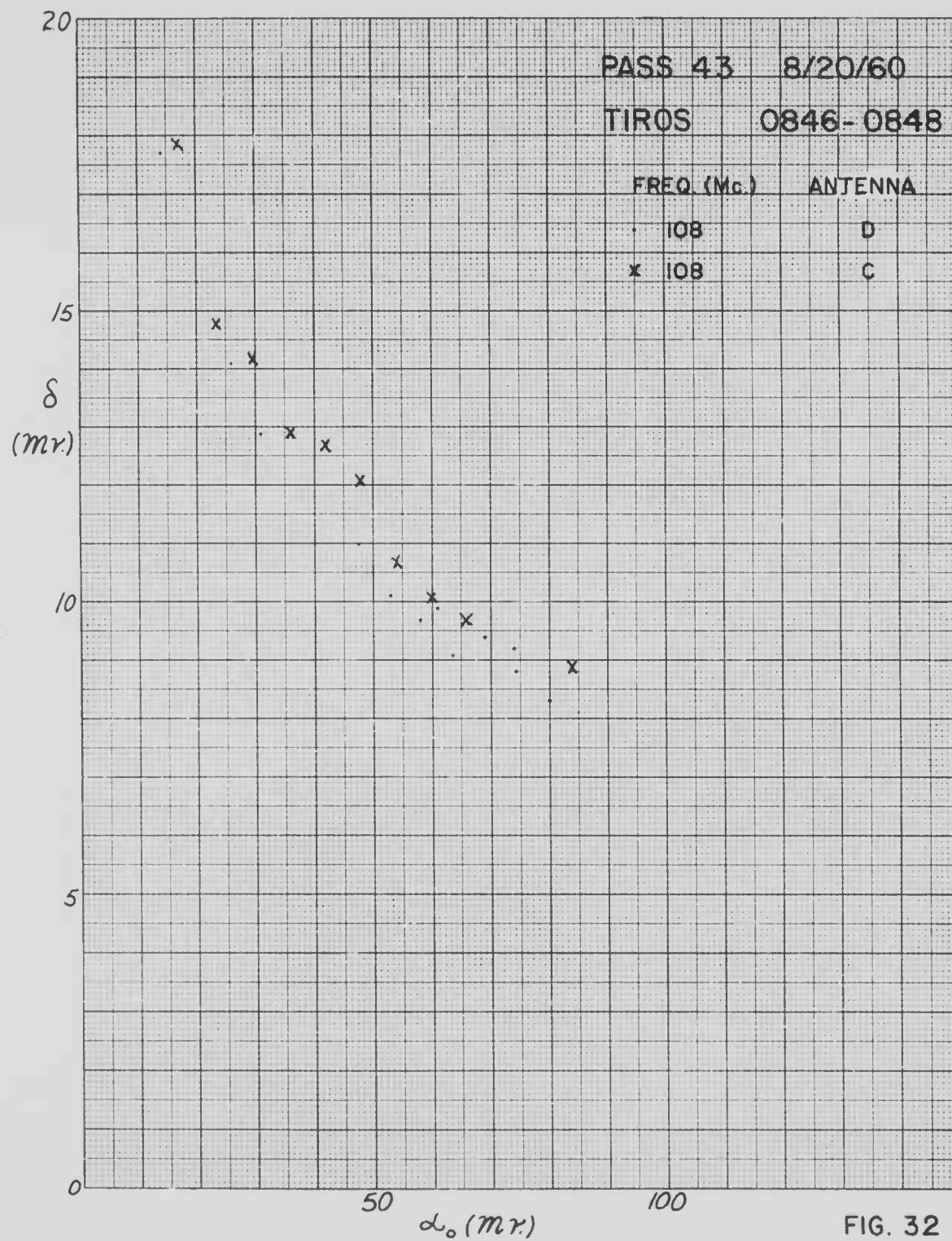


FIG. 32

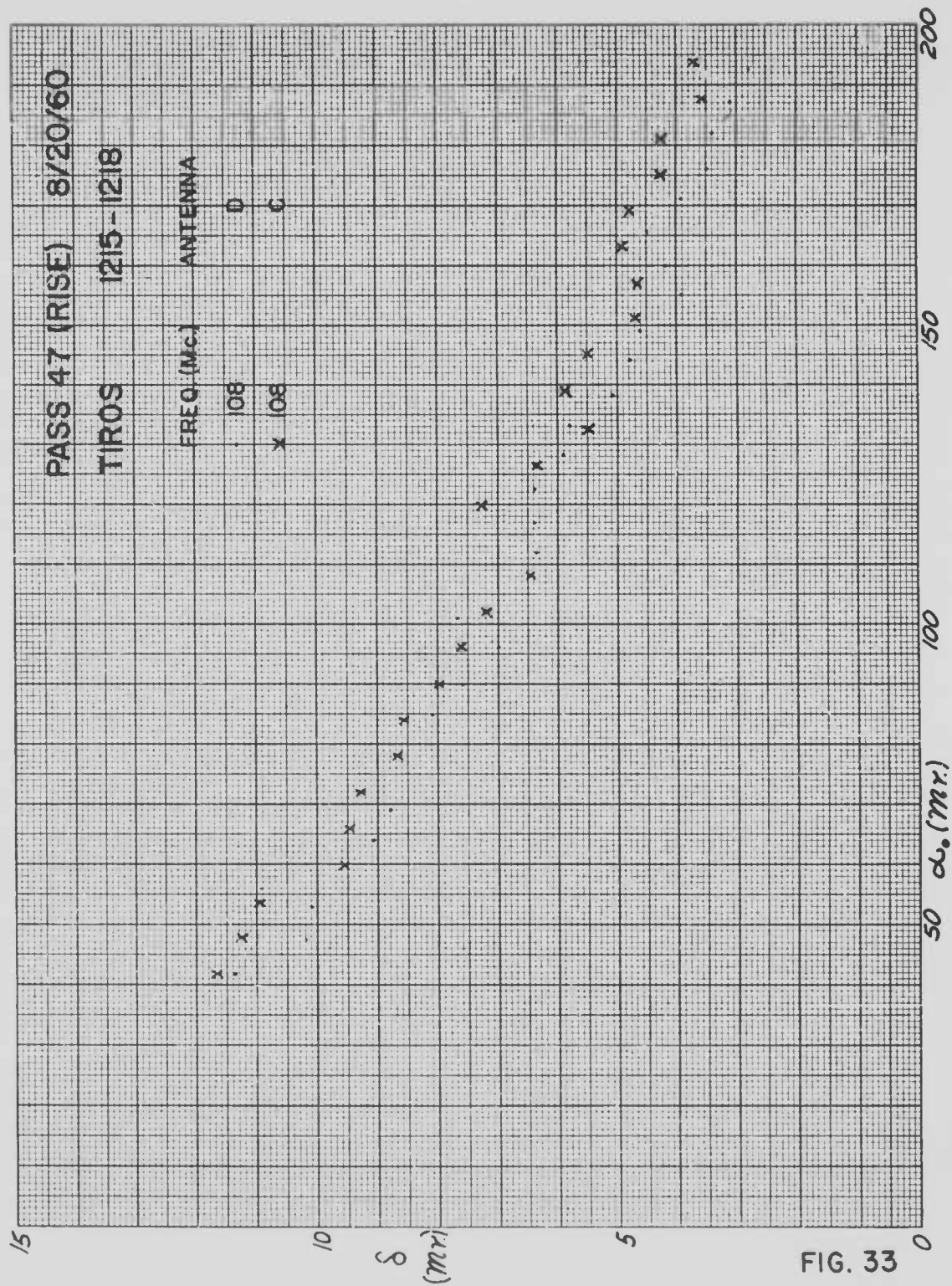


FIG. 33



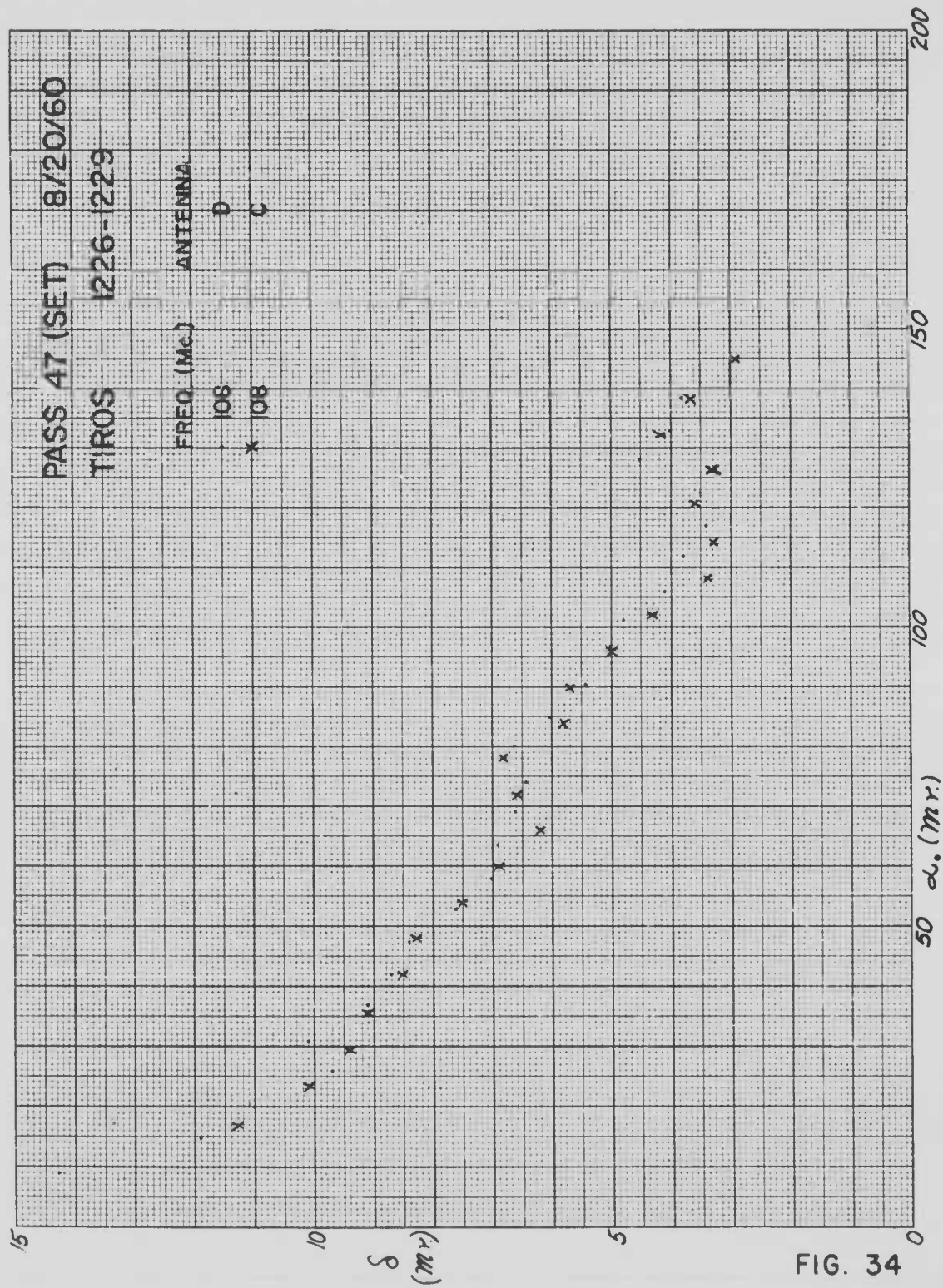


FIG. 34



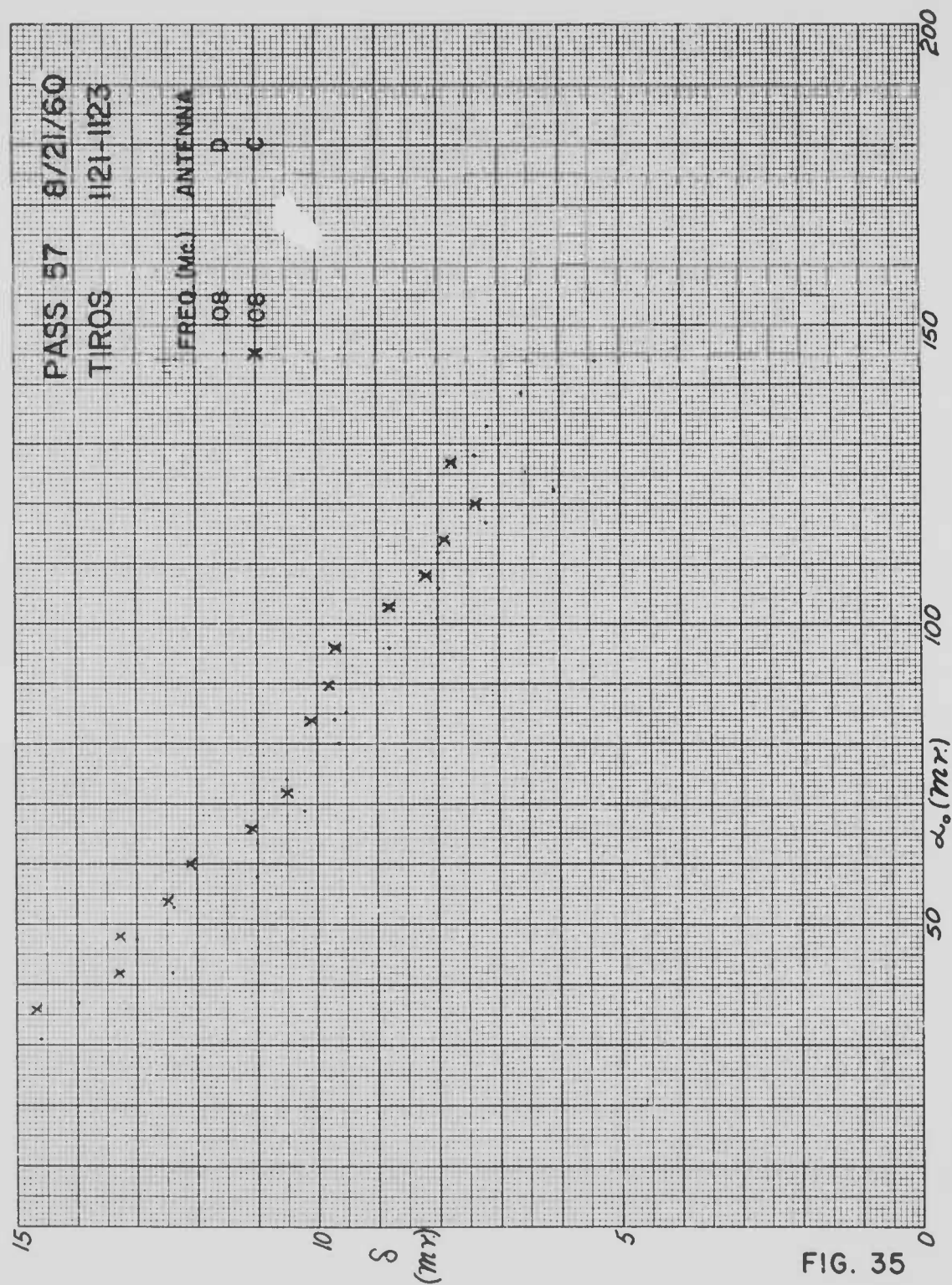
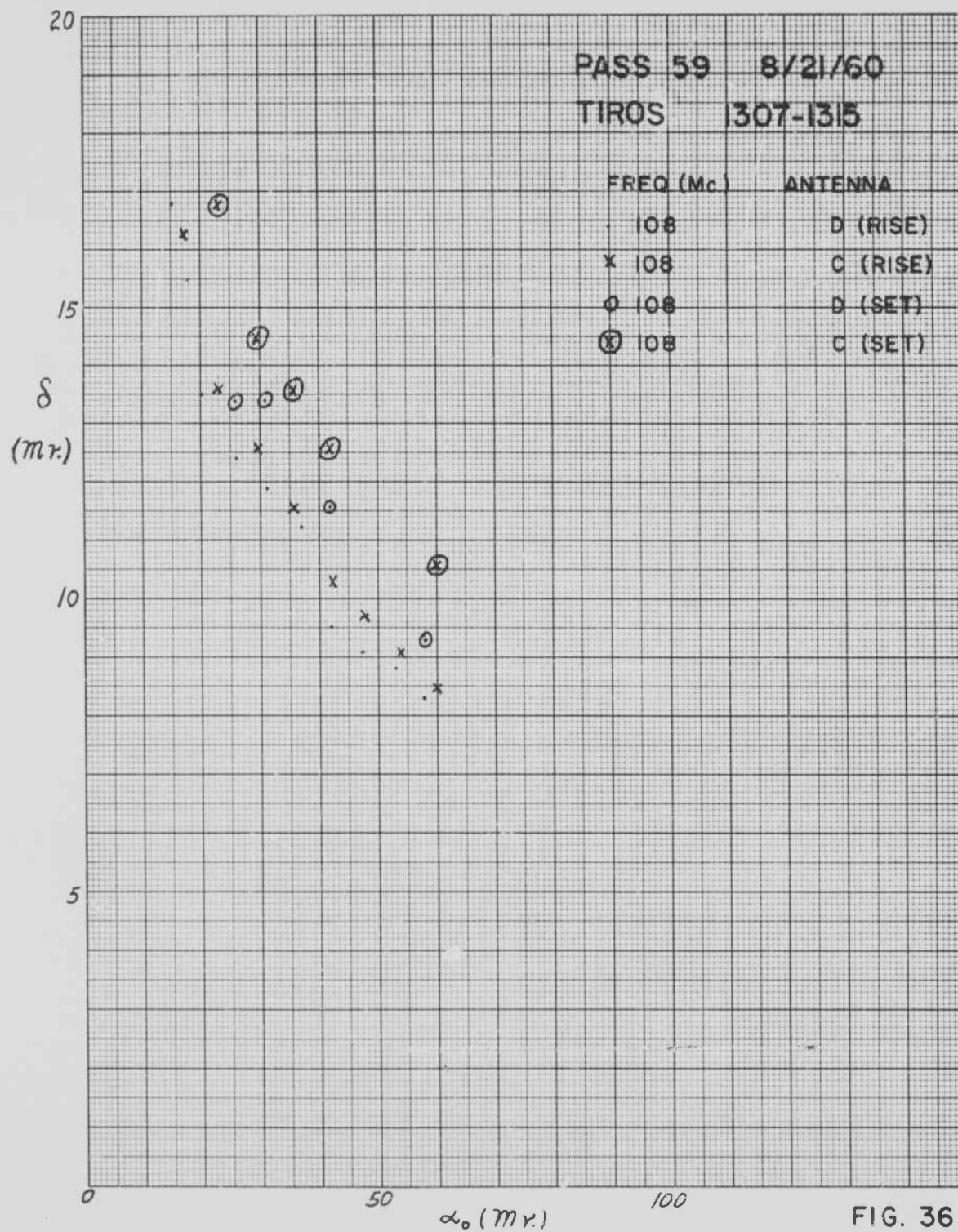


FIG. 35



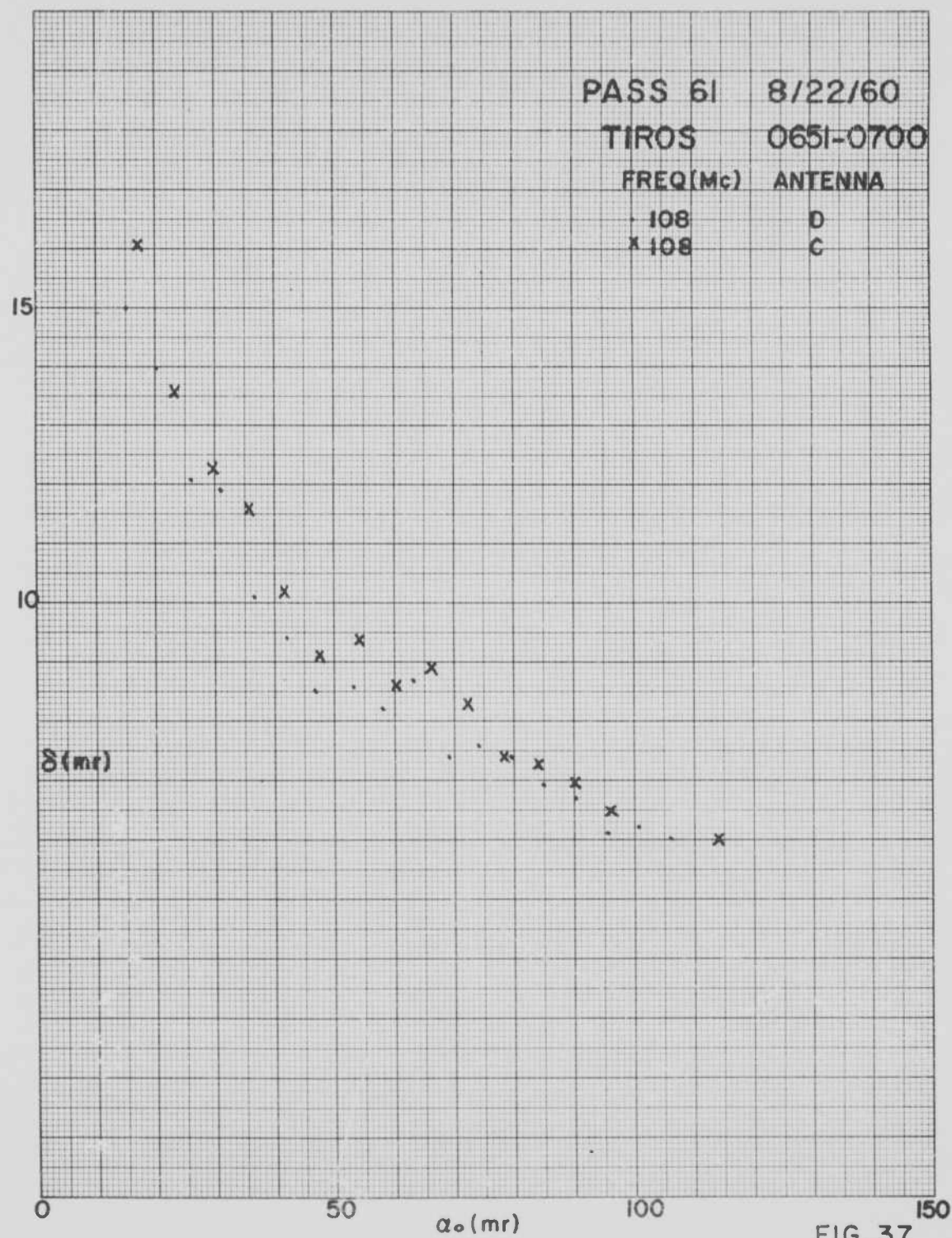


FIG. 37

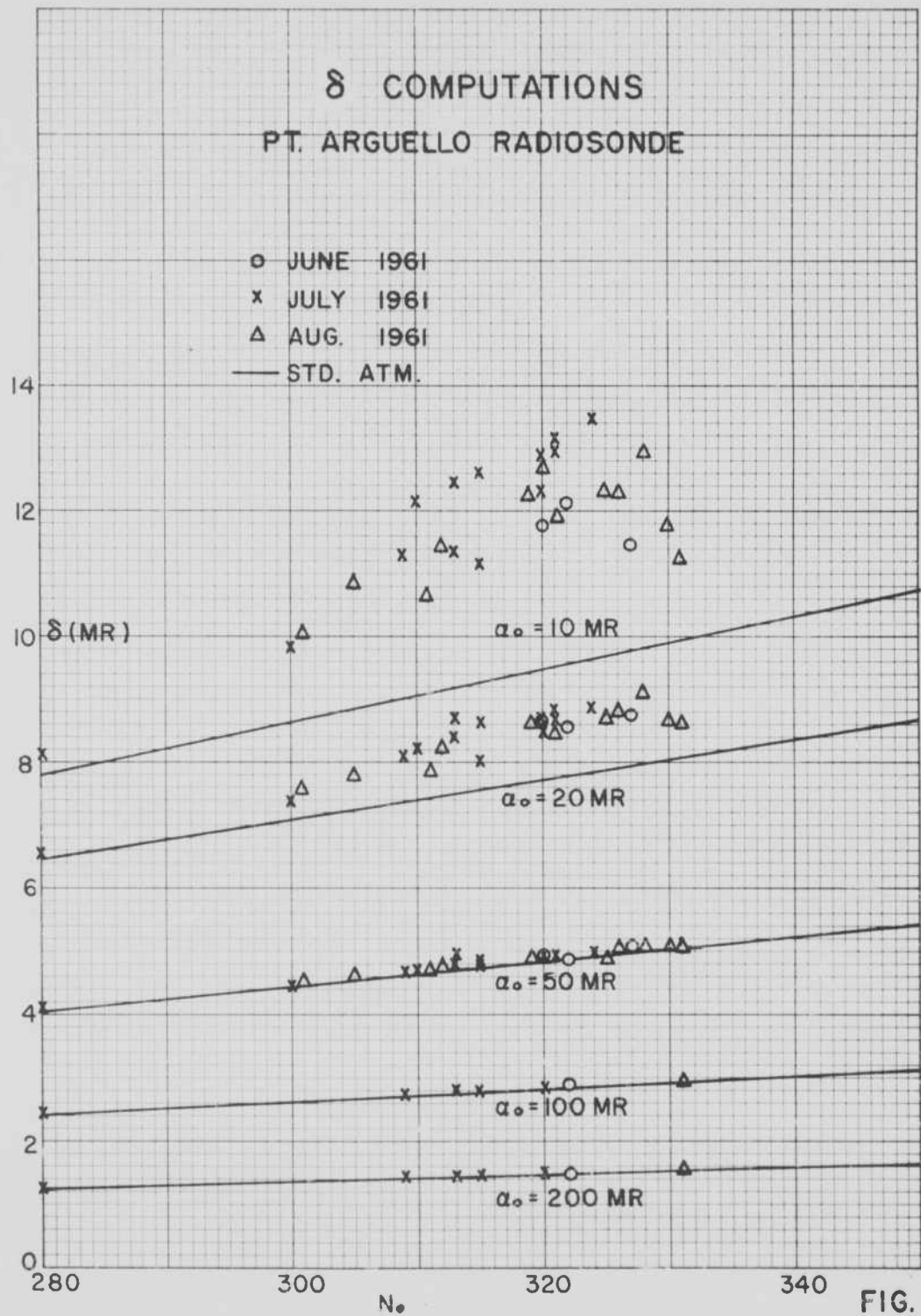
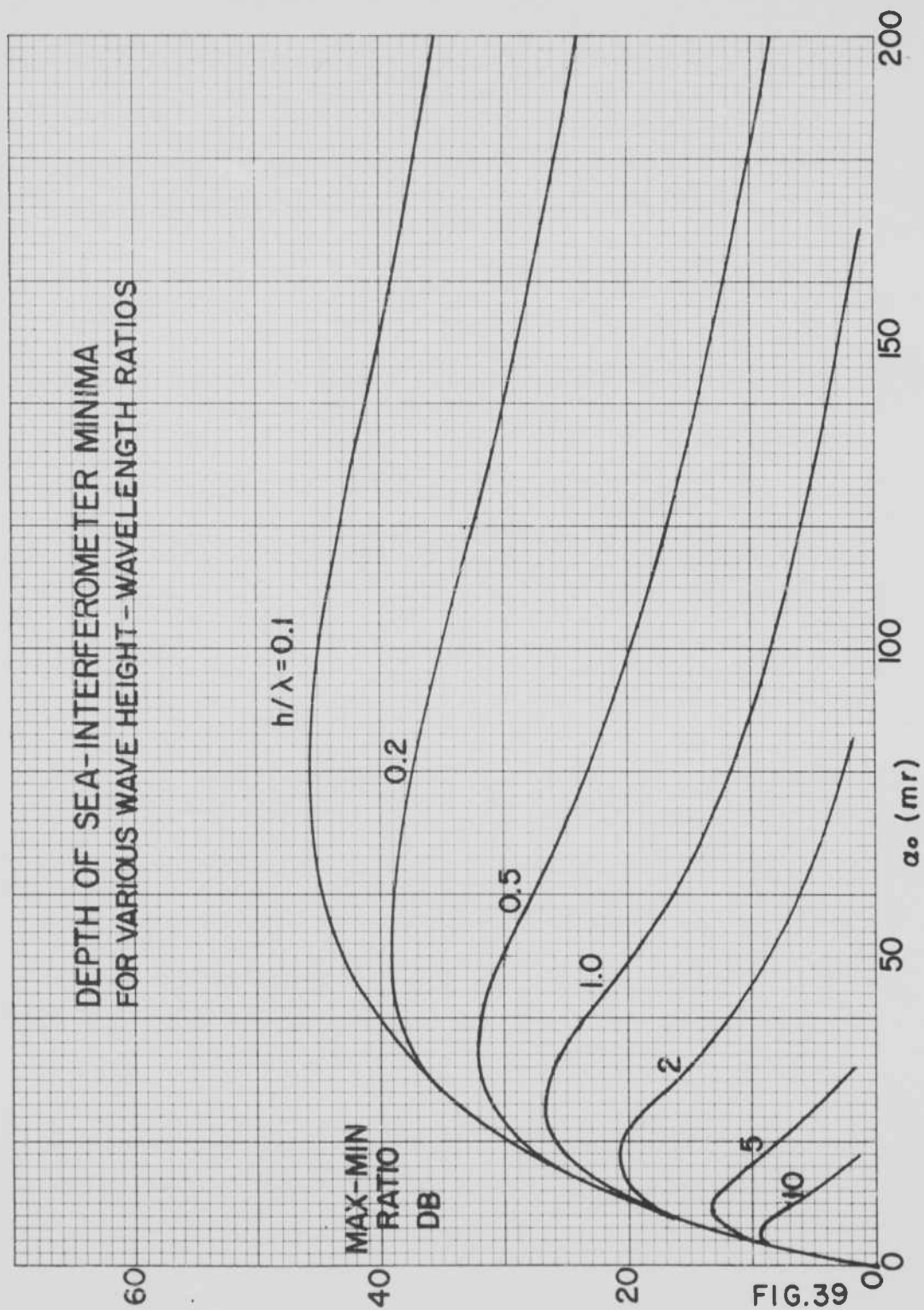
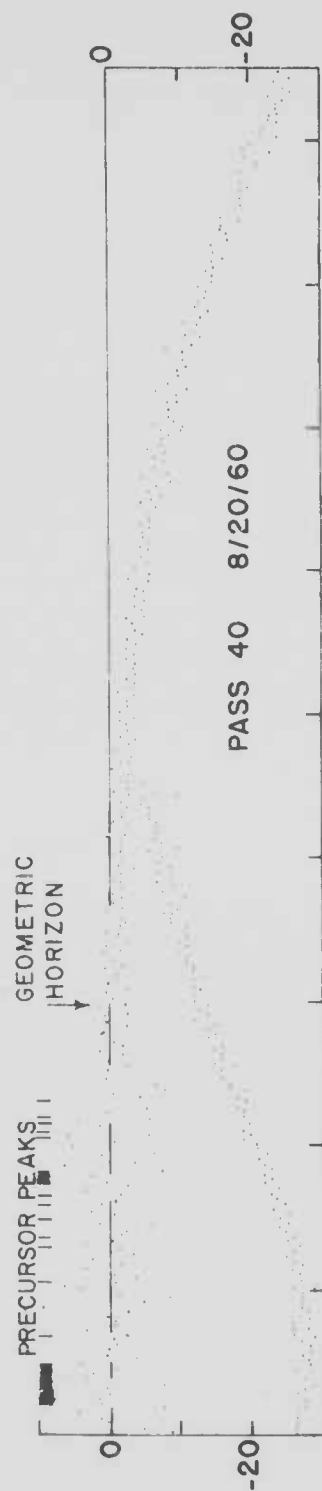


FIG. 38





# OBSERVED DOPPLER FIRST DIFFERENCES TIROS 108 Mc.



IST  
DIFF  
CPS/2 SEC  
INTERVAL

TIME INTERVALS — 1 MINUTE

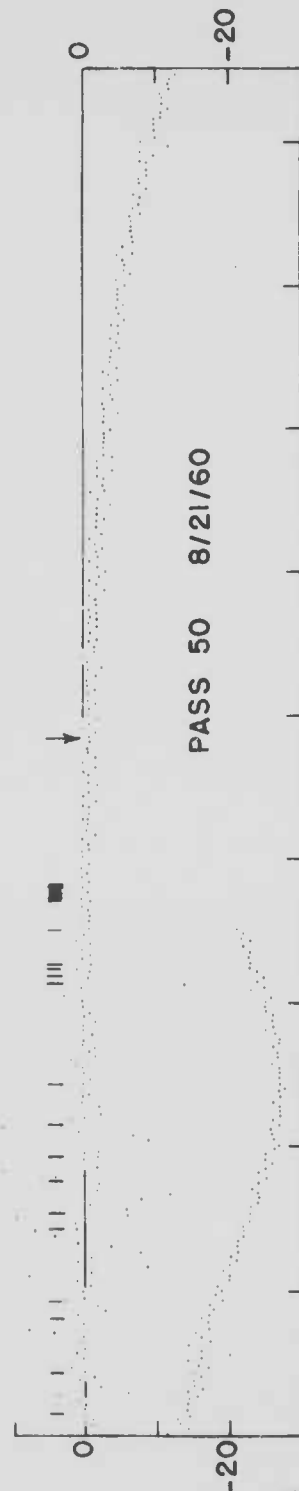


FIG. 40

# OBSERVED DOPPLER FIRST DIFFERENCES TRANSIT 2A 216 Mc.

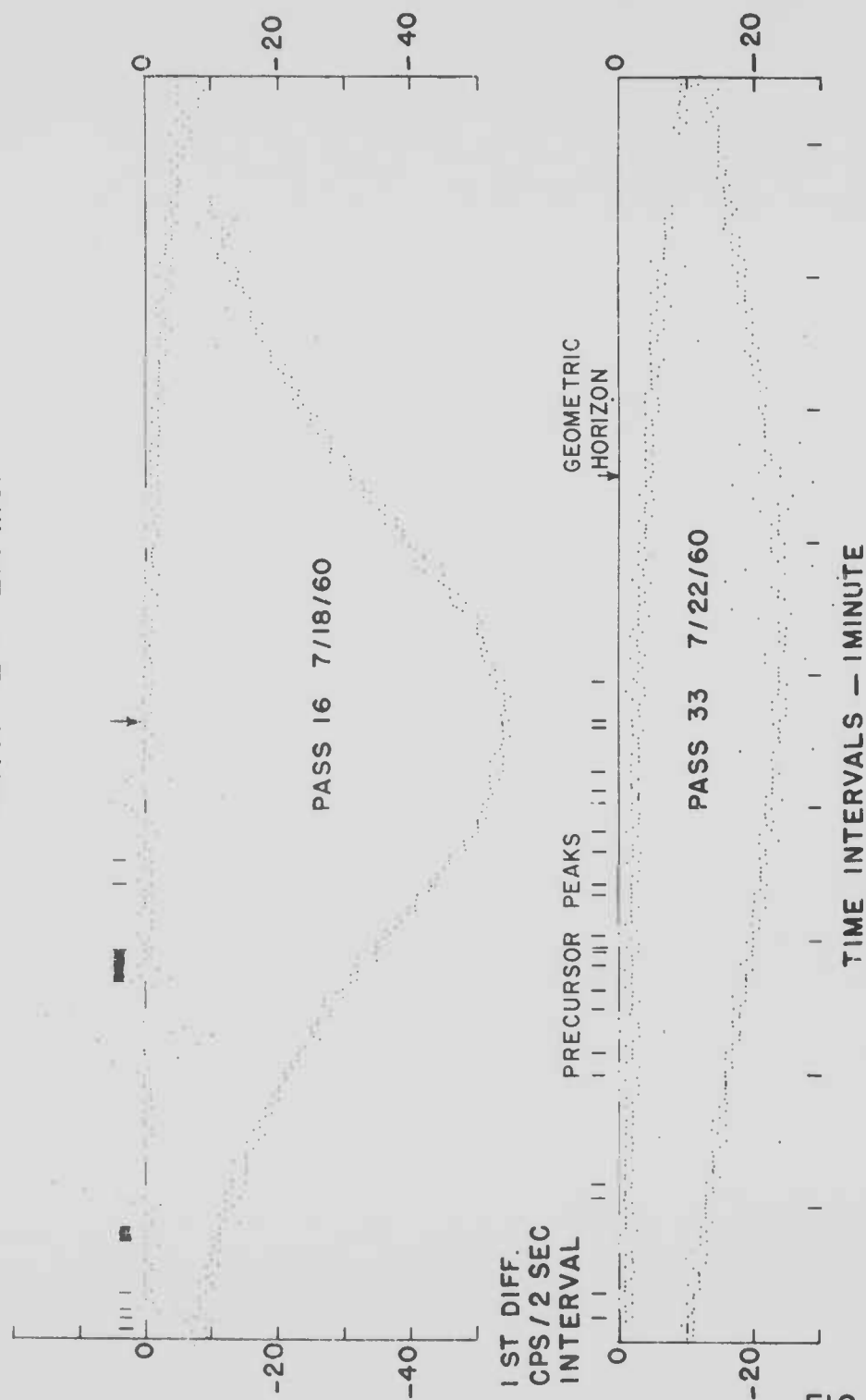


FIG. 41

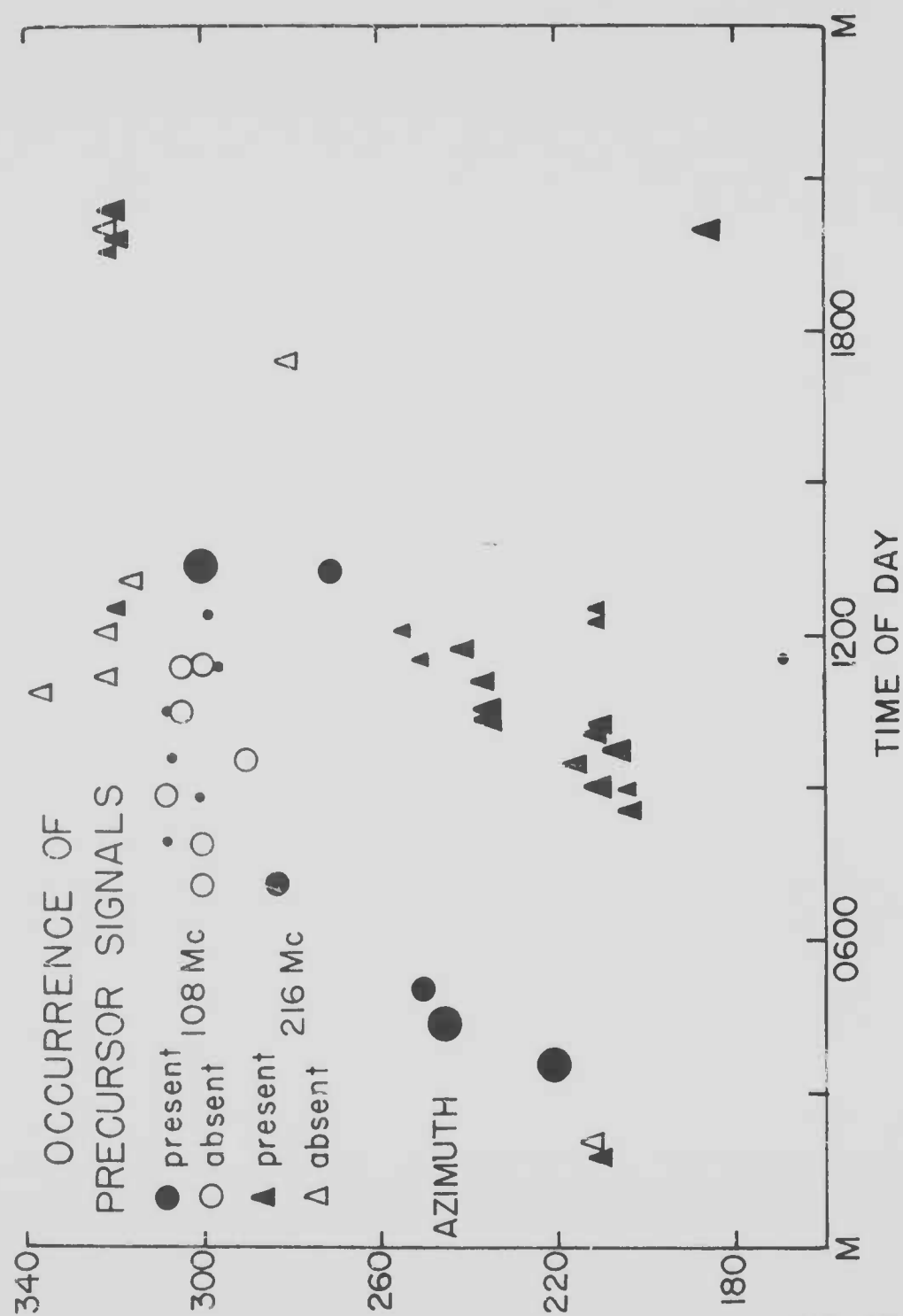


FIG. 42



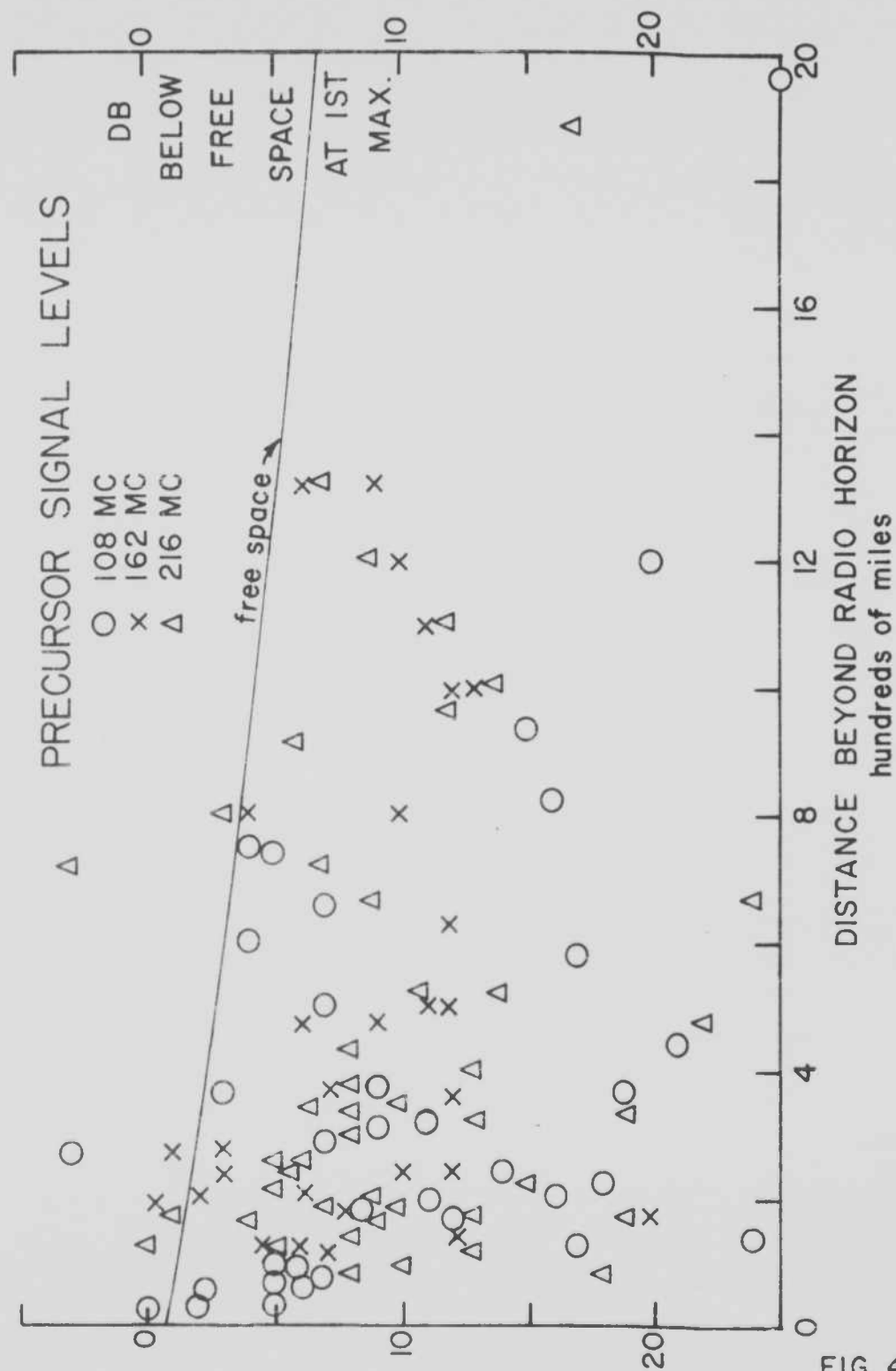


FIG. 43

UNCLASSIFIED

UNCLASSIFIED